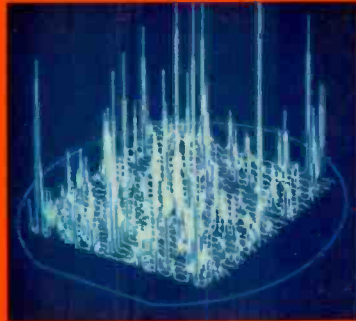# RCA
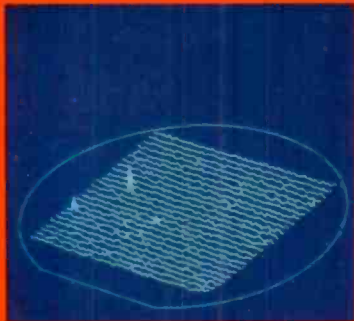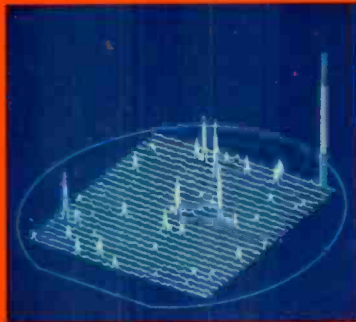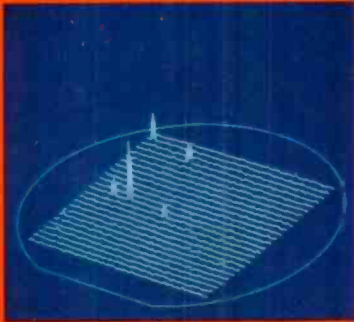# Review

Light Scattering Topography Plots of Si Wafers

March 1985 Volume 46 No. 1

Our cover shows three-dimensional light scattering topogrophy plots of Si wafers. Top and bottom sets are for wafers from two different manufacturers before (left) and after (right) denuding. Background "roughness" shows structural perfection; "spikes" are defects or, to a minor extent, dust. This figure is taken from the paper by Steigmeier and Auderset which discusses the use of elastic light scattering techniques to test nondestructively for dust, defects, and structural perfection in silicon wafers.

RCA Review

Contents

Elastic Light Scattering Techniques for Semiconductor Technology

E. F. Steigmeier and H. Auderset
Laboratories RCA Ltd., CH-8048 Zurich, Switzerland

Abstract—This paper provides an overview of elastic light scattering tech-
niques for use in semiconductor technology. The following
methods are described: (1) optical scanner used for dust and
defect detection, (2) optical scanner used for testing the struc-
tural perfection of films and wafers, (3) rapid testing for ac-
ceptability of polycrystalline silicon in terms of amorphous or
crystalline deposition, and (4) elastic light scattering topog-
raphy of starting wafers. The latter three methods are novel in
the field, and can contribute to a considerable device yield
improvement.

Introduction

In modern semiconductor technology, with its requirements for pro-
cessing perfection, it is necessary to test wafers and films nonde-
structively for dust, defects, and structural perfection. Only a very
few methods are suited for this purpose. The present paper presents
an overview on how this testing can be performed very effectively
by means of elastic light scattering techniques. The following topics
will be discussed:
(1) rapid testing for dust and local defects on wafers or films,
(2) rapid testing of wafers and films for extended structural perfec-
     tion,
(3) rapid testing of amorphous versus polycrystalline growth of
     polysilicon,
(4) light scattering topography of starting wafers in order to select
     the best material for top performance devices.

1. Testing for Dust and Defects with the Optical Scanner

In a previous paper, we have described an optical scanner system[1] which can show, in a matter of seconds, dust on a wafer or local defects in it. Fig. 1 shows the experimental arrangement chosen for optimum performance of the instrument. A laser beam is focused onto the wafer and the elastically scattered light is collected coax-
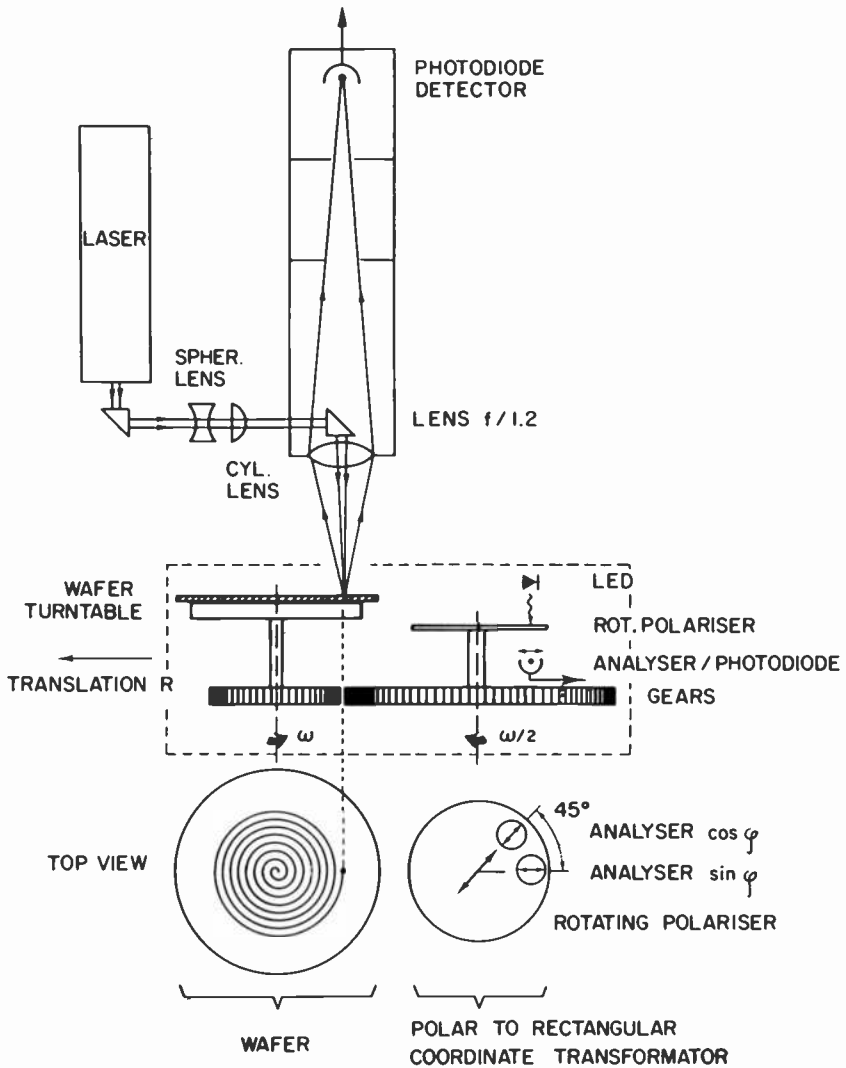
Fig. 1—Laser scanner measuring arrangement.

ially and detected by a photodiode. The electronic signal is processed and displayed as a wafer map (see Fig. 3, center). Since the wafer rotates and is translated at the same time, the laser spot describes a spiral path on the wafer. A microscope attachment permits inspection of a particular spot on the wafer chosen from the wafer map shown on the display. In addition, the number of events can be read from a digital display. For further details the reader is referred to the previous paper.[1]

Based on this work, a commercial system has been produced by Fluorocarbon[2] under license from RCA. This instrument is currently being used throughout the industry to monitor cleanliness in the processing of semiconductors. Hand-loading of the wafer onto the turntable is used in a model that provides flexibility for those applications where studies are made under varying conditions (e.g., testing cleaning equipment, furnaces, reactors, different processing steps, etc.) and where it is not desirable to test all the wafers of a process line. On the other hand, a pick-and-place cassette loading version of the optical scanner, as shown in Fig. 2, is offered for
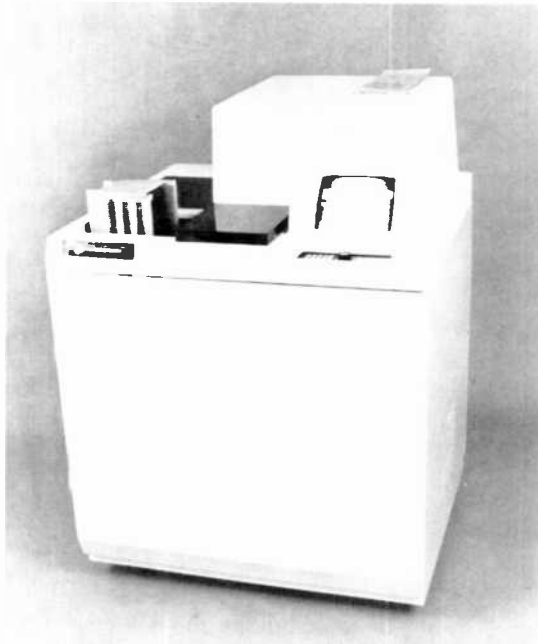
Fig. 2—Laser scanner DDS-3 cassette (pick-and-place) loading unit produced by Fluorocarbon PSD, Anaheim, CA.

applications where continuous in-line testing for dust and defects is needed. Rubber-belt transport is specifically avoided in favor of the pick-and-place feature, since, as Kleppinger has shown,[3] the belts of a competitor's model produce track marks on the wafer. This certainly would be a disadvantage in high-quality processing, even though the belt track deposits are on the backside of the wafer. It also was felt that air-cushion transport is inferior to pick-and-place in terms of chipping debris. The instrument is fully microprocessor controlled with a printer output and computer interface. Two versions are available, using either a red HeNe (632.8 nm) or a blue HeCd (441.6 nm) laser source. The penetration depths in crystalline silicon are 2.5 μm or 0.2 μm, respectively. The blue version is to be preferred where one does not want to probe too deeply into the material; in advanced technology, the active device is rather shallow (homoepi or SOS), and it may be misleading to test to depths that are not relevant.

Typical examples of scanner results are found in Fig. 3, which shows a scanner map and individual bumps and defects.[1] It can be seen from the SEM photomicrographs that these defects have indeed
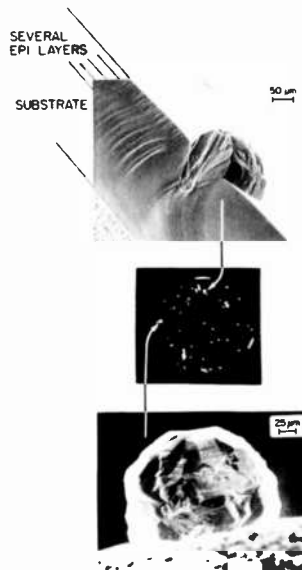
Fig. 3—Scanner map of individual bumps and defects on epitaxially grown films and SEM photomicrographs (top and bottom) of two of the larger defects as marked in center photo (courtesy of L. Krausbauer). It is seen that defects have nucleated at the surface of the original substrate.
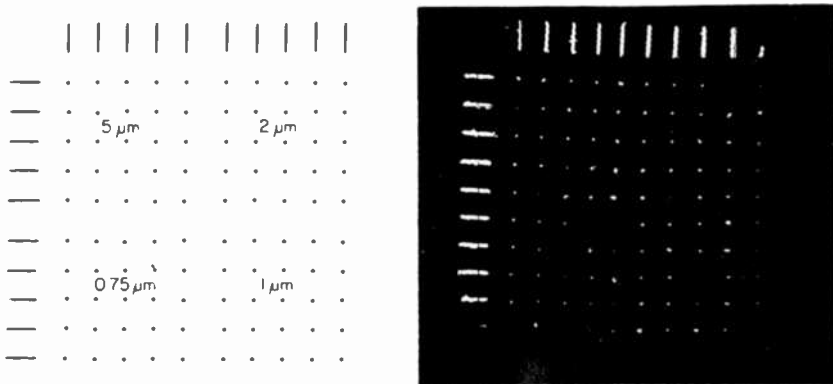
Fig. 4—Chrome mask pattern (left) for testing the dust and defect detectability limit. Dots represent regular arrays of holes of specified diameter etched into chrome films (courtesy of R. Geshner and J. Mitchell). Resulting scanner mapping (right) of these holes.

formed at the surface of the original substrate, most likely from nonremoved particulates which act as nucleation centers.

An important figure for the process engineer is the ultimate *detectability limit* of an instrument in terms of the size of particulates or defects. As we have stressed previously,[1] however, instrument calibration in terms of size only, as done by some models on the market, is grossly misleading to the user, since the scattering efficiency also depends on the refractive index change, shape, form, facetting, and surface quality (smooth or rough) of the particulate or defect. We have made an attempt to establish the detectability limit for our instrument, as shown in Fig. 4. A processed chrome mask with an array of holes of different diameters is scanned. It was found, as seen in the right hand part of the figure, that many 0.75-μm diameter holes are observable. (In reproducing the right hand part of Fig. 5 we have removed, for clarity, a considerable number of events from between the rows that were caused by residues of strongly scattering electron-beam resist.) Since particulates and defects scatter light considerably more effectively (maybe 10–100 times) than straight holes, we have concluded that the detectability limit of the instrument must be considerably below 0.75 μm. We estimate it to be about 0.4 μm (wavelength) or less.

2. Testing for Structural Perfection (Bulk Quality) with the Optical Scanner

In device technology, the bulk quality (structural perfection) of a semiconductor wafer or film is of prime importance, since this quan-
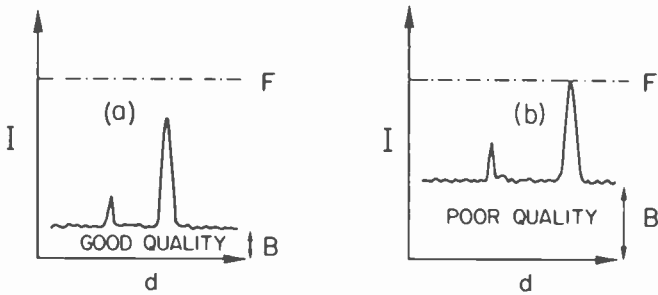
Fig. 5—Intensity signal *I* versus distance *d* along the spiral path of the wafer. The dash-dotted line represents the writing (full) threshold *F* of the storage scope. (a) shows results for a good quality wafer with small background level B and (b) for a poor quality wafer with large background level B. Individual defects or dust, which are not considered here, are indicated by the spikes.

tity in many cases determines the yield quite directly.[4] We have established[5] that the optical scanner can also be used to determine "bulk" structural perfection. Fig. 5 shows how this is done. The intensity signal of a particular wafer, in addition to showing individual peaks originating from individual defects, shows a background level that is not electronic noise but directly related to the background wafer quality. It is produced by light scattering due to variations in the refractive index in between some major events or defects. The dc voltage needed to shift this background level up to the writing threshold on the display can, therefore, be used as a direct measure of wafer or film quality. More details can be found in a previous work.[5]

Fig. 6 shows this effect on a wafer with an unusually strong variation in structural perfection along a vertical line. At the points
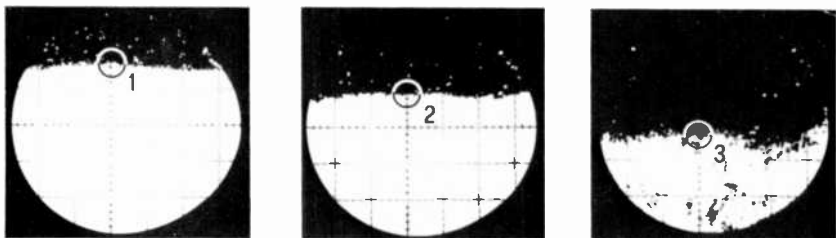
Fig. 6—Scanner mapping of a wafer showing dust and defects and the structural perfection variation along a vertical line: left photo is taken at a threshold setting of 750 units (best quality); center at 730 units; and right at 680 units (worst quality).

where the "writing" threshold is just reached, the threshold setting on the scanner unit can be used directly as a measure of structural perfection; high values mean good perfection (low scattering background) and vice versa.

The use of this technique to determine wafer quality is shown in Figs. 7 and 8 for two different cases. Fig. 7 presents a direct correlation[5] between the [221] twinning concentration in SOS wafers on the one hand (this has been shown to be one major yield-limiting factor in SOS devices[6]) and the optical scanner units on the other. While other methods are available[7] for determining the structural perfection of SOS layers, the optical scanner represents a very convenient means to rapidly determine and map the layer quality in a matter of seconds.

The use of the optical scanner is, however, not limited to crystalline silicon. It can be applied to any other material. Fig. 8 shows the structural perfection of amorphous low-pressure chemically-vapor-deposited (LPCVD) silicon as-deposited on top of a bulk oxide (region I) or on top of a previously phosphorus-doped polycrystalline silicon oxide (region II). We first observed the drastic difference in structural perfection between region I (perfect) and region II (very poor) on an optical scanner; it is caused by short-range order dif-
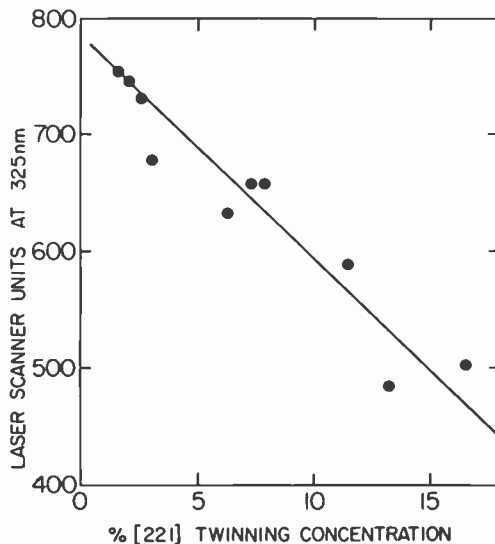
Fig. 7—Structural perfection (bulk quality) of SOS wafers. Shown is the correlation between laser scanner units and [221] twinning concentration in the top silicon layer.
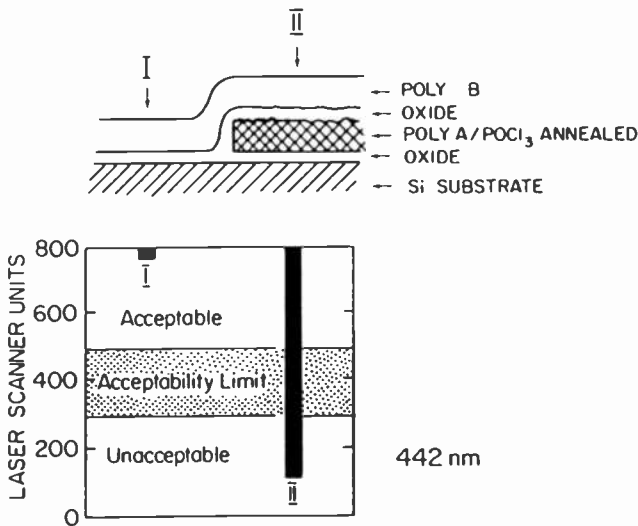
Fig. 8—Laser scanner testing of structural perfection of 6600 Å-thick amorphous silicon deposited by LPCVD on top of a bulk oxide (region I) and on top of a phosphorus-doped polycrystalline silicon oxide (region II). Light penetration is about 1200 Å in the amorphous silicon. Note the drastic difference in structural perfection.

ferences due to growth on a smooth or a rough substrate (oxide). For further details the reader is referred to Ref. 5.

3. Rapid Acceptability Testing of Amorphous LPCVD Polysilicon

Still another application of the optical scanner is in the field of phase transformations,[5] i.e., for testing whether a deposited material is amorphous or crystalline. Elastic light scattering is, in general, not the same for the different crystallographic phases of a material; this difference is in addition to the variation in light scattering with structural perfection within one phase discussed in Sec. 2. Raman scattering peak intensity is a convenient empirical indicator of whether a film is crystalline (large peak intensity), amorphous (small peak intensity), or mixed (intermediate). Raman scattering measurements are, however, quite involved in terms of equipment and not well suited for a manufacturing environment. On the other hand, as shown in Fig. 9, a correlation can be established between Raman peak intensity and optical-laser-scanner
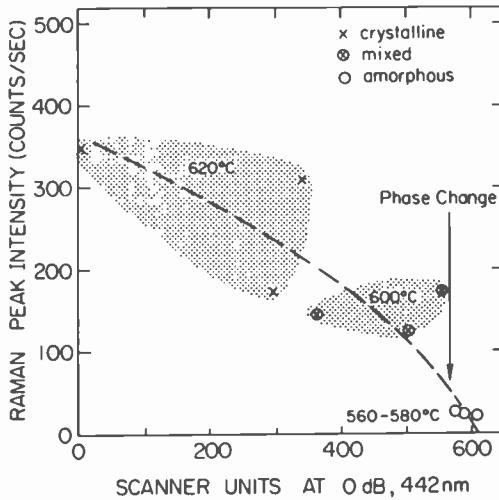
Fig. 9—Rapid acceptability testing of as-grown amorphous versus poly-crystalline LPCVD silicon by means of scanner unit readings. Shown is correlation between Raman peak intensity or crystal-lographic phase and laser scanner units for films deposited at different deposition temperatures; 560–580°C is desired for high-quality material.

readings in terms of elastic light scattering (scanner units). The laser scanner, therefore, can be used as a quick and convenient way to determine if an LPCVD process is producing the desired material, e.g., amorphous layers rather than polycrystalline silicon layers. This is of considerable importance, since it has been shown[8] that only material which is grown by LPCVD in the amorphous form and later recrystallized has the quality required for high-perfor-mance devices (strain-free, smooth, good lithographic properties, high breakdown fields across oxides, etc.).

4. Elastic Light Scattering Topography

Encouraged by the success in characterizing wafers in terms of ex-tended structural perfection by the optical scanner (Sec. 2), we de-cided to push the technique of elastic light scattering one step fur-ther.

For many devices (e.g., CCD imagers), the quality of the starting wafer is believed to be a major yield-limiting factor (in terms of cosmetic image quality). We have started a program to measure elastic light scattering topography in a manner somewhat similar

to that in which x-ray topography is used. With light, we can limit the probed region to the most relevant top surface sheet (e.g., 2500 Å for 5145 Å laser light) in terms of structural uniformity. Fig. 10 shows the experimental arrangement, which is similar to Fig. 1. The scanning is different (X-Y rather than spiral) but, more important, the mechanical design is much more sophisticated (i.e., made with a higher level of precision) and the filtering and detection sensitivity is much higher. On the 3-inch (or 4-inch) wafer (values in parentheses are for the 4-inch wafer), an inscribed square of 50 mm × 50 mm (66 mm × 66 mm) is scanned with a spot size of 2 mm × 40 μm, using 100-mW incident 5145-Å laser power, at 2500 (4356) points per wafer in 25 (33) tracks of 100 (132) points. Ten percent of the area is sampled within each track, but consecutive tracks are adjacent. An ITT FW 130 photomultiplier with a dark-count rate of about 0.5 photoelectrons per second is used as a detector. The equipment is computer controlled and the data are stored on disk, from which it can then be displayed in various forms.

We have measured three sets of (100)-oriented, CZ-grown oxygen-doped CCD starting wafers obtained from three different manufacturers. Each set was scanned as received and after an oxygen denuding cycle, performed according to the manufacturer's recommendation.

The results of light scattering topography are presented in Table 1 in terms of median values (3rd lowest in a data window of 6 values). For each wafer, the minimum and the maximum median
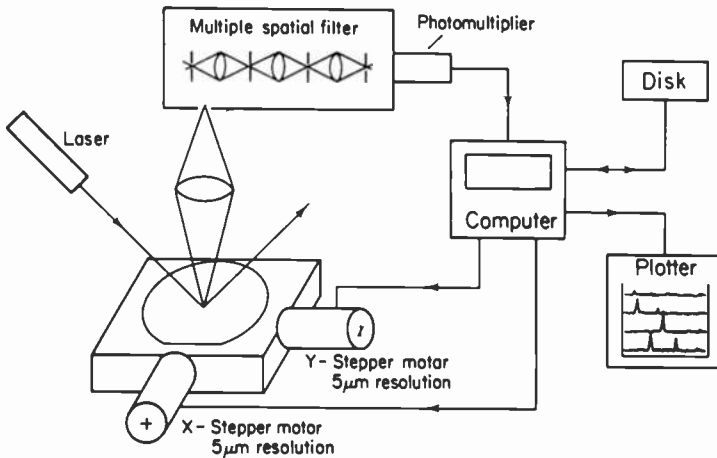
Fig. 10—Experimental arrangement for measuring light scattering topography.

Table 1—Median values obtained from light scattering topography measurements on wafers from three different manufacturers

Wafer	Vendor	Description	Median Values Before Denuding ($\times 10^3$ counts)		Median Values After Denuding ($\times 10^5$ counts)		Blue Scanner Counts (on 50 mm dia. area)	
			Minimum	Maximum	Minimum	Maximum	$\Delta = 10$	$\Delta = 50$**
QC 619-10	A	CZ 34/36	0.34	4.0	0.52	2.7		
-11*		ppm O_2	0.26	1.1	0.69	2.1	av = 115	av = 42
-12			0.35	1.2	0.51	(622.2)	std dev = 25	std dev = 17
-13			0.26	2.1	0.78	16.2		
-14			0.34	1.1	0.69	6.0		
-15			0.34	1.2	0.85	2.3		
QC 631-1*	B	CZ 26/32	1.3	4.8	2.7	16.7		
-2		ppm O_2	1.4	4.6	2.2	16.8	av = 200	av = 66
-3			1.3	3.6	2.0	22.4	std dev = 45	std dev = 21
-4			3.0	5.4	4.6	(86.4)		
-5			1.7	3.9	2.3	31.5		
-6			1.6	3.8	2.2	16.0		
QC 626-20	C	CZ 29/32	0.43	5.6	21.3	97.5		
-21		ppm O_2	1.2	10.6	—	—	av = 425	av = 139
-22			1.1	10.3	21.5	(327.6)	std dev = 395	std dev = 113
-23			1.75	23.1	13.3	56.5		
-24			0.69	6.6	—	—		
-25			0.95	8.7	—	—		

* Results for these wafers are plotted in Figs. 11, 12, and 13.
** Taken at 10 or 50 units below full (blossom) threshold.

values were determined over all 25 tracks of the wafer. These values give an indication of the *absolute level* of the elastic light scattering for each wafer and of the *relative fluctuations*. By taking the median value, it is possible to exclude individual defects. (All wafers are practically dust free, and the topography measurements are of course done in a dust-free environment, typically class 1.)

As can be seen from Table 1, the results before denuding (i.e., as received) are quite different for the different manufacturers; they are of different level but quite uniform within two of the sets (A and B), while the set from manufacturer C shows considerable scatter. After denuding, the results stay uniform within the sets from manufacturers A and B; the absolute level increases, however, more for manufacturer B than for A and even more for manufacturer C.
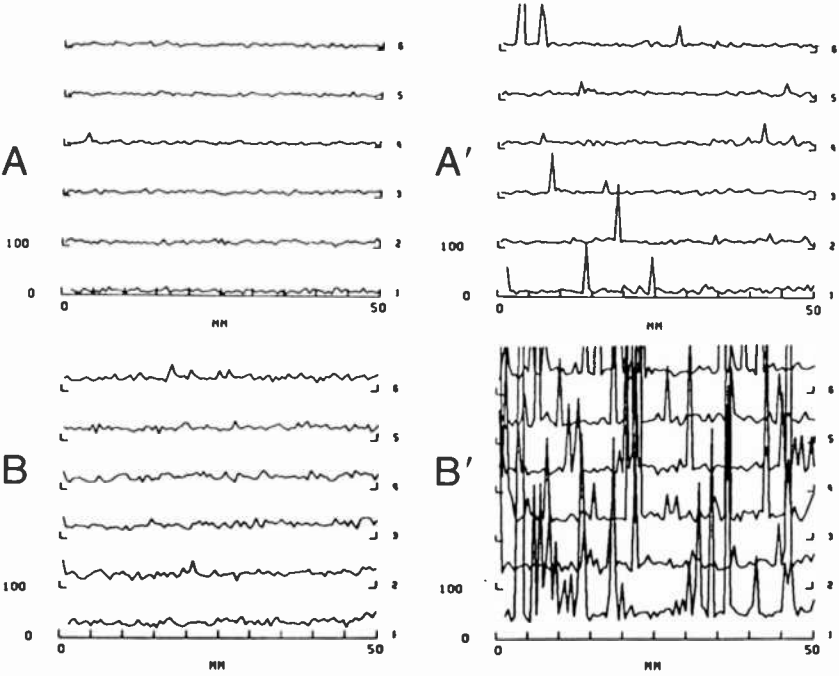
Fig. 11—Light scattering topography traces (extracts) from two different manufacturers (top and bottom) before and after denuding (left and right). Six adjacent traces of 2 mm width on each wafer are shown. Wafers are oxygen doped (≈25 to 35 ppm) CZ(100). The difference in bulk quality ("noise" or "roughness") for the two wafers before denuding can be seen in the left-hand traces. The two right-hand traces show the drastic difference in bulk structural quality and number of individual defects ("spikes") after denuding.

Fig. 11 shows the original data (*no* median values and tracks 1–6 only) for one typical wafer each from manufacturers A and B (denoted in Table 1 by an asterisk). Before denuding (left hand part of Fig. 11), one can clearly see the difference in absolute level and the difference in fluctuations (noise or roughness) of the traces.

Predenuded   Denuded

Low   High
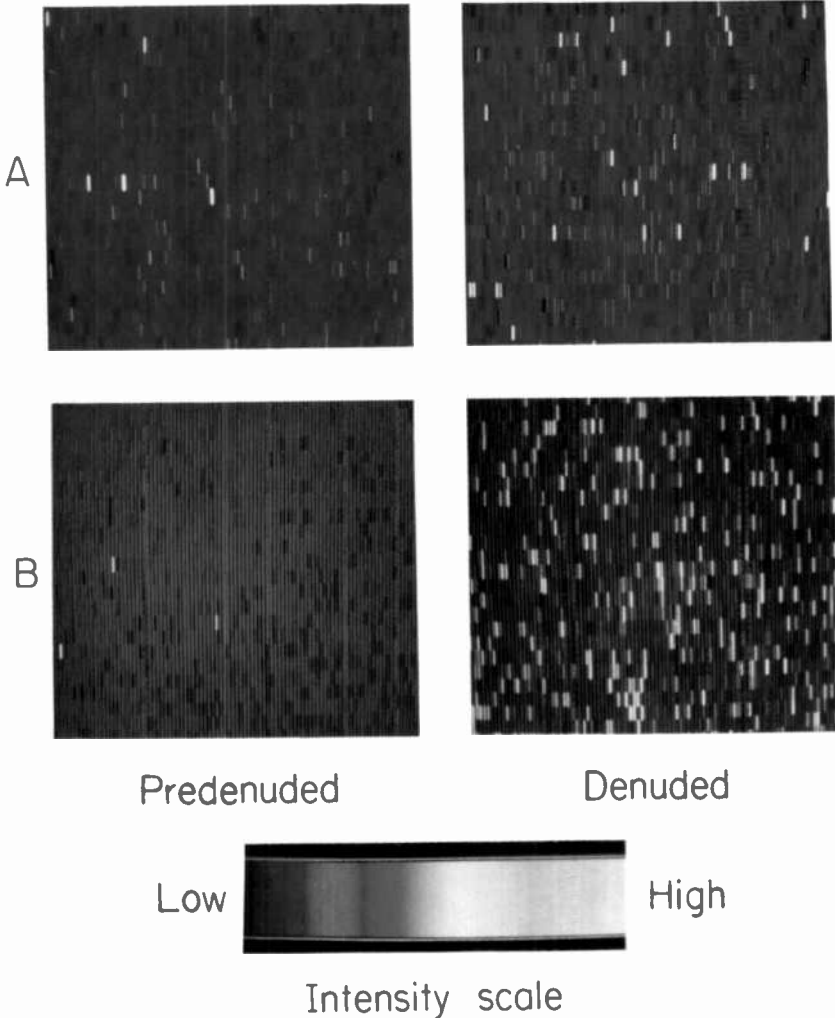
Intensity scale

Fig. 12—Light scattering topography plots in color; structural perfection and defect density are indicated by the color intensity as defined by the color scale shown below (courtesy of P. Seitz). As in Fig. 11, top and bottom are for two different manufacturers and right and left are before and after denuding.

After denuding (right hand part of Fig. 11), the increase in all the parameters mentioned above can be seen; one can also see an increase in the number of individual (local) defects, much more so for manufacturer B than for A. For comparison, Table 1 shows the defect readings taken on the wafers after denuding using the optical scanner (see Sec. 1). It should be emphasized that while the setup used to measure light scattering topography has been developed to a much higher level of sophistication than the optical scanner, the scanner results could be used to establish the rating of the groups A, B and C in terms of individual defects after denuding.

Fig. 12 shows color plots for the data of Fig. 11 (all 25 tracks); here, intensity is given by the "hot" color scale as shown at the

Predenuded   Denuded
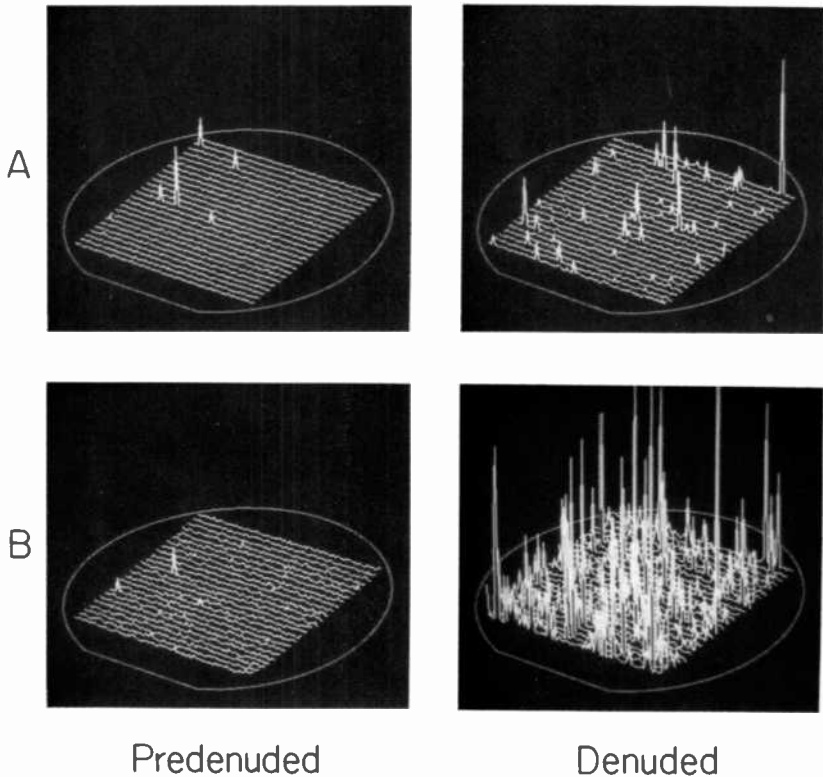
Fig. 13—Presentation of the data of Fig. 12 as a three-dimensional plot. Background "roughness" shows structural perfection; "spikes" are defects or, to a minor extent, dust (courtesy of P. Seitz).

bottom. The absolute level can now be read from the average color, the fluctuations in structural perfection from the color variations, and the individual defects from the "hot" spots.

In Fig. 13 the presentation is made in terms of a three-dimensional plot that shows the trace "roughness" (fluctuations in structural perfection) and the "spikes" (individual defects) very nicely.

As yet, we have not been able to establish the exact nature of the individual defects and of the increased background level (structural perfection) and its fluctuations, though we plan to do so by means of etching and TEM studies. It is also not clear as yet which level of structural perfection is required to yield the best devices. Since we find, however, that a low background level (highest structural perfection) correlates with a low number of individual defects, we tend to favor the wafers of best structural perfection. Further work is needed, quite obviously, to fully establish the details.

Conclusion

We have shown that elastic light scattering techniques can be used quite effectively in different applications of device technology. To our surprise, the semiconductor industry is making very little use of this rapid, nondestructive method, apart from testing for dust. In particular, testing for structural perfection by means of the optical scanner and by light scattering topography is only used, to our knowledge, within RCA. It is anticipated, however, that this novel technique will be applied increasingly in the near future as the dimensions of devices shrink and the need for device perfection increases.

Acknowledgment

References:

[1] E. F. Steigmeier and H. Auderset, "Optical Scanner for Dust and Defect Detection," *RCA Review,* **44,** p. 5 (1983); U.S. Patent 4,314,763 (1982).

[2] Fluorocarbon PSD, P.O. Box 3640, 1432 S. Allec Street, Anaheim, CA 92803.

[3] R. Kleppinger, "Laser-Based Defect Particle Counter Used in LSI Production," *RCA Engineer,* **29,** p. 53 (1984).

[4] M. T. Duffy, P. J. Zanzucchi, W. E. Ham, J. F. Corboy, G. W. Cullen, and R. T. Smith, "Optical Characterization of Silicon and Sapphire Surfaces as Related to SOS Discrete Device Performance," *J. Crystal Growth,* **58,** p. 19 (1982).

[5] E. F. Steigmeier and H. Auderset, "Structural Perfection Testing of Films and Wafers by Means of Optical Scanner," *J. Electrochem. Soc.,* **131,** p. 1693 (1984); U.S. Patent 4,391,524 (1983).

[6] G. W. Cullen, M. S. Abrahams, J. F. Corboy, M. T. Duffy, W. E. Ham, L. Jastrzebski, R. T. Smith, M. Blumenfeld, G. Harbeke, and J. Lagowski, "The Characterization of Heteroepitaxial Silicon," *J. Crystal Growth,* **56,** p. 281 (1982).

[7] For details, see further references given in Ref. [5].

[8] G. Harbeke, L. Krausbauer, E. F. Steigmeier, A. E. Widmer, H. F. Kappert, and G. Neugebauer, "High-Quality Polysilicon by Amorphous Low Pressure Chemical Vapor Deposition," *Appl. Phys. Letters,* **42,** p. 249 (1983); "LPCVD Polycrystalline Silicon; Growth and Physical Properties of In-Situ Phosphorus Doped and Undoped Films," *RCA Review,* **44,** p. 287 (1983); "Growth and Physical Properties of LPCVD Polycrystalline Silicon Films." *J. Electrochem. Soc.,* **131,** p. 287 (1984).

Characterization of Heteroepitaxial Silicon on Sapphire by UV Reflectometry

M. T. Duffy, G. W. Cullen, and R. A. Soltis
RCA Laboratories, Princeton, NJ 08540

G. Harbeke and J. R. Sandercock
Laboratories RCA Ltd., Zurich, Switzerland

Abstract—In previous work we described an optical reflectance technique used for quality control purposes in the qualification of silicon-on-sapphire (SOS) films. The procedure, applicable to film thicknesses in the 0.5–0.6 μm range, was based on specular reflectance measurements at two wavelengths, 280 nm and 400 nm. Because of recent interest in SOS films in the 0.2–0.3 μm thickness range, the measurement procedure has been modified to evaluate films in both thickness ranges using the same instrumentation as before. The modified procedure, based on measurements at one wavelength (280 nm), eliminates optical interference effects in the case of the thinner films and increases the sensitivity of the measurement technique.

Introduction

The quantitative characterization of silicon surfaces by specular reflectance measurements in the UV region, at a wavelength of about 280 nm (~4.4 eV), has been described previously.[1] It has been shown that lattice disorder influences the $X_4–X_1$ silicon transition at about 4.3 eV and modifies the optical constants of silicon.[2] Degraded crystallinity and surface topographical effects, which cause light scattering such as "haze" in the case of silicon on sapphire, result in diminished reflectance at photon energies in the vicinity of this transition. Thus, the reflectance of silicon in this spectral

region can, in principle, be used to determine silicon surface quality. The penetration depth of incident radiation at a photon energy of 4.3 eV is estimated to be less than 100 Å in silicon, a region of considerable interest in determining the electrical properties of silicon-on-sapphire (SOS) MOS devices.

In our initial work on the optical characterization of heteroepitaxial silicon films on sapphire,[3] we demonstrated that UV reflectance data could be correlated with (a) the volume concentration of {221} in the films (microtwin volume concentration) as determined by x-ray pole-figure analysis, (b) the concentration of deep electronic states within the bandgap as determined by surface photovoltage spectroscopy, and (c) SOS circuit yield and performance. Based on these observations, silicon films were divided into categories as described previously,[3] and a UV reflectometer suitable for quality control purposes was subsequently developed for determining these categories on the product line.[4] Several of these reflectometers are currently employed by people involved in heteroepitaxial silicon technology.

Until recently SOS circuits were fabricated in silicon films that ranged in thickness from 0.5 to 0.6 μm, and the procedures used for determining film quality based on reflectance were established for this thickness range. Several factors have changed since the measurement procedures were established. For example, silicon film quality from vendors has improved considerably because of the reflectance criteria, and there is a current need for a rapid nondestructive technique for qualifying heteroepitaxial silicon films in the 0.2 to 0.3 μm thickness range. Such films may be used in solid-phase epitaxy (SPE) to improve film properties for very high speed integrated circuit (VHSIC)-type SOS circuits.

In this paper we describe a modified procedure for optically characterizing improved quality heteroepitaxial silicon films over the thickness range of current interest. The procedure utilizes the reflectometer described in Ref. [4].

Experimental Background

In our early work,[3] reflectance measurements were made on SOS samples at two separate wavelengths: $\lambda \simeq 280$ nm (~4.4 eV) and $\lambda \simeq 400$ nm (~3.1 eV). The reflectance at 280 nm was used to determine film surface quality, while reflectance at 400 nm was used as a reference level with which to compare the reflectance of the same sample at 280 nm. The reason for choosing 400 nm as the reference wavelength arose from the observation that, at longer wavelengths,

optical interference effects resulted from reflections at the film and substrate surfaces for film thicknesses in the 500 to 600 nm range. It should be noted that the optical constants of silicon change rapidly with wavelength in this region.[2] Measurements were made on prototype equipment assembled in the laboratory, and the difference in reflectance at the two wavelengths, ΔR, was taken as a measure of film quality. This procedure helped to eliminate problems associated with making absolute reflectance measurements. For example, sample curvature, warpage, and taper caused variation in the position of the focused light spot falling on the detector (photomultiplier tube). Variation in detector response over the area of the sensing element caused considerable variation in output signal, even for the same sample when rotated about a given measurement position. Thus, the two-wavelength measurement helped in overcoming these problems, since the reflectance at both wavelengths was affected in a similar way.

Most of the problems associated with the prototype equipment measurements were eliminated in the subsequent development of our current UV reflectometer.[4] A description of the measurement procedure is repeated here for convenience. The optical layout is shown schematically in Fig. 1. The instrument uses a deuterium lamp, which provides a continuum light source. The filter holder has two compartments for interference filters and can be fixed in two positions for a choice of wavelengths. The transmitted light is reflected by the mirror and focused by lens I in a plane close to the chopper such that the light spot on the sample surface has a diameter of 4 to 5 mm. During about 45% of the chopper time cycle,
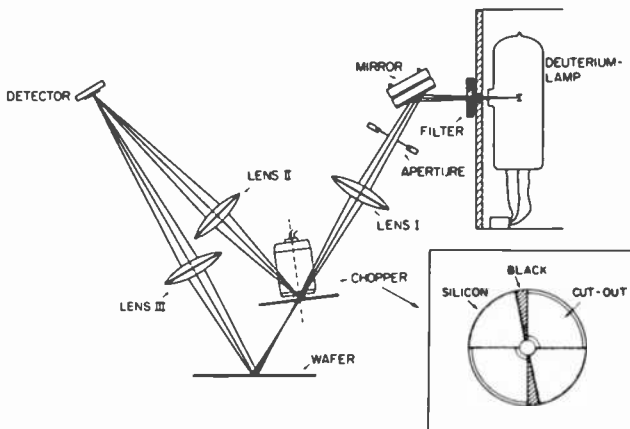
Fig. 1—Optical scheme of the UV reflectometer. After Harbeke et al.[4]

the light beam is reflected by the chopper blades in the direction of lens II and the detector. There is zero reflection during about 5% of the chopper time cycle, because the corresponding parts of the chopper blades are blackened. During the remaining 50% of the time cycle, the light is transmitted by openings in the chopper wheel and reflected by the sample in the direction of lens III and the detector. The reflecting chopper blades are made of well-polished single-crystal silicon so that the reflectance at any wavelength is close to the ideal reflectance value of silicon. Thus the chopper blades act as an internal standard.

The detector is a silicon photovoltaic device having an enhanced UV response. The electric signals from the detector (reference signal A and sample signal B) are used to form the difference signal $A-B$. The difference signal is normalized by dividing by the signal A in order to eliminate fluctuations and drift of the lamp intensity. With silicon chopper blades of the ideal reflectance values, the signal $(A-B)/A$ would be a direct measure of the deviation of the reflectance of the sample from the ideal value. Since the surface quality of the silicon blades may change with time, the signal $(A-B)/A$ after phase-sensitive detection and amplification is set electronically to zero for a reference wafer of high-quality single-crystal silicon. In a subsequent measurement of an SOS wafer, the signal $(A-B)/A$ is a direct measure of the difference in reflectance between the reference wafer and the SOS sample at the measuring wavelength. It is displayed on a digital voltmeter (DVM) display unit.

The ratio $(A-B)/A$ can be measured at $\lambda = 280$ nm and $\lambda = 400$ nm, giving values for ΔR_{280} and ΔR_{400}, respectively. Since the operation of this reflectometer is not subject to the problems encountered with our prototype unit, it is only necessary to make measurements at one wavelength, namely 280 nm, for the qualification of SOS wafers. However, because of the established categorization of SOS wafers based on measurements made on the prototype equipment, we used the difference term $\Delta R_{280} - \Delta R_{400} = \Delta$ as the quality factor for the newly developed reflectometer. The value of Δ correlated very well with our previous reflectance data used in the categorization scheme. The parameter Δ has been used to date for the qualification of SOS wafers ($t_{Si} = 0.5 - 0.6$ μm) by the various users of the UV reflectometer.

Recent interest in the evaluation of SOS films in the 0.2-0.3 μm thickness region requires a revision of the optical measurement procedure. The Δ parameter cannot be used since the term ΔR_{400} is modified by interference effects associated with reflections at the silicon and sapphire surfaces in the case of the thinner films. In-

stead, the term ΔR_{280} can be used for the qualification of all film thickness since the penetration depth at this wavelength is estimated to be only about 100 Å or less. There are also other reasons for choosing the term ΔR_{280} as the quality factor, as will become apparent in the next section.

Calibration Curve

The previous scheme[3] for the categorization of silicon films on sapphire is shown in Fig. 2 (curves 1, 2, and 3). Since microtwins represent a dominant crystallographic defect in the structure of SOS films,[5,6] the twinning concentration in these films[7] was used to represent film crystalline quality. The correlation of reflectance data with the twinning concentration in SOS films made it possible to
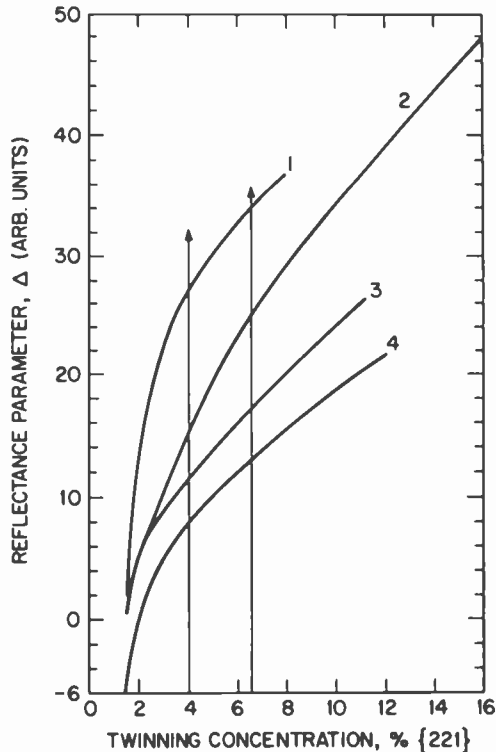
Fig. 2.—Plot of relative reflectance, Δ, versus twinning concentration, % {221}, in silicon films on sapphire from different vendors. The curves are approximate. Up to 4% {221} volume concentration is assigned category A; 4% to 6.5% {221} is assigned category B; and >6.5% {221} is assigned category C. After Duffy et al.[3]

establish a calibration curve representing silicon film quality for a given set of growth parameters in the case of each vendor. The quality of the silicon films subsequently prepared under the same conditions could then be assessed in each case by measuring sample reflectance and referring to the appropriate calibration curve. For quality control purposes, SOS wafers were separated into categories. Category A represents silicon films with a twinning concentration up to approximately 4% (volume concentration) for a film thickness of 6000 Å. Category B represents a twinning concentration between about 4% and 6.5%, and category C represents a twinning concentration greater than 6.5% (see Fig. 2). The corresponding range of values for the UV reflectance parameter for each vendor can be read from the graph in Fig. 2. This enables quality control personnel to determine quickly and nondestructively the crystalline quality of heteroepitaxial silicon films without the need for time-consuming analytical procedures. The curves in Fig. 2 were traced through the scattered data for a large number of samples. The data points are not shown.

It is evident from Fig. 2 (curves 1, 2, and 3) that there is not a unique relationship between reflectance data and the twinning concentration in SOS films. It is important therefore, that the type of reactor used and the film growth parameters be specified. An example of the influence of growth parameters in a barrel reactor on silicon-film reflectance characteristics is shown in Fig. 3. It can be seen that the growth temperature influences the slope of the curve. The higher growth temperatures give rise to a surface topography that causes light scattering and thus increases values of the reflectance parameter for a given twinning concentration. For this reason, light-scattering measurements alone cannot be used to assess film crystalline quality as defined by twinning concentration. The increase in the reflectance parameter with higher growth temperatures is attributed to increased light scattering at both wavelengths (for a given {221} concentration), with the reflected intensity at 280 nm being more strongly influenced than the reflected intensity at 400 nm because of the wavelength dependence of light-scattering effects. When the growth parameters are held constant, however, it is possible to obtain a calibration curve for a given vendor as shown in Fig. 2, which can be very useful in monitoring film quality and detecting changes due to the infusion of impurities into the deposition zone or other factors that degrade film crystallinity. The reflectance measurements are also very useful in studies relating to optimization of film growth parameters at a given temperature. An example of this is also shown in Fig. 3, which indicates
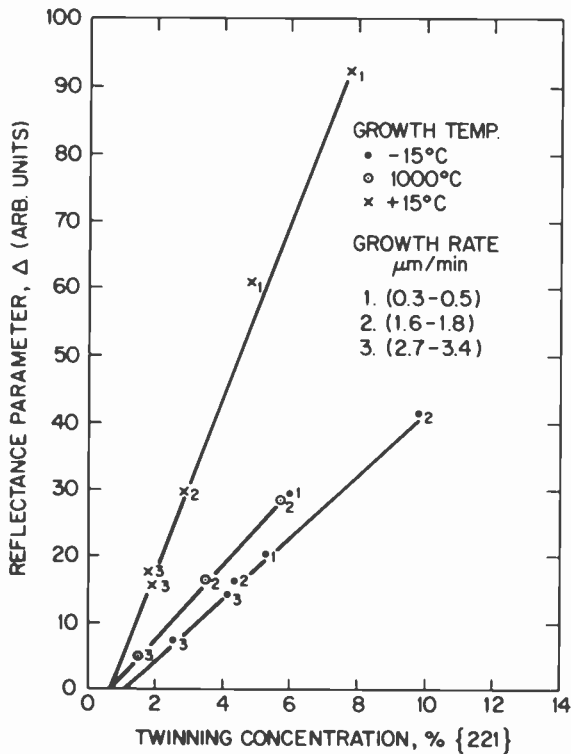
Fig. 3.—Plot of relative reflectance, Δ, versus twinning concentration in SOS films for different growth rates and growth temperatures. After Duffy et al.[3]

that faster growth rates favor better film quality at the three growth temperatures shown. The three upper curves shown in Fig. 2 were obtained on material from three vendors corresponding to three different types of reactors for silicon heteroepitaxy; Vendor 1 (curve 1) used a horizontal reactor, Vendor 2 (curve 2) a vertical reactor (or pancake reactor), and Vendor 3 (curve 3) a barrel reactor. Three separate curves arise because of different surface texture associated with heteroepitaxial silicon films prepared in the three different types of reactors, probably because different growth parameters were used.

It is apparent from Figs. 2 and 3 that low values of the reflectance parameter correspond to improved film crystallinity; subsequent work by the different vendors therefore focused on providing films characterized by low values of the reflectance parameter. This virtually eliminated separate calibration curves for the different vendors. A typical calibration curve for Vendors 1 and 2 is now repre-

sented by curve 4 in Fig. 2 rather than curves 1 and 2. Consequently, reflectance measurements can now be used with greater assurance in the qualification of SOS films. In addition, most currently available SOS films fall into category A. This means there is little difference in reflectance parameter values from one vendor to another, since the calibration curves converge near the origin in Fig. 2.

Correlation Between Reflectance Data and Twinning Concentration

One shortcoming of the previous procedure for the qualification of currently available films is that the reflectance parameter $\Delta = \Delta R_{280} - \Delta R_{400}$ is now smaller than before and becomes negative at low {221} concentrations, as shown in curve 4 of Fig. 2. It is desirable, therefore, to choose a reflectance parameter that is more sensitive than Δ to the defect structure in the films and that eliminates negative values. One procedure for doing this is described next.

An example of the correlation between reflectance data and twinning concentration (% {221} by volume) in a set of SOS samples is shown in Fig. 4. The upper two curves in the figure represent ΔR_{280} and ΔR_{400}. The relative reflectance scale is expressed in arbitrary units. One unit on this scale corresponds to a difference reflectance of about 0.05% at $\lambda = 280$ nm and about 0.035% at $\lambda = 400$ nm. This arises from the amplification used and the spectral dependence of the reflectivity of silicon. The bottom curve represents the reflectance parameter, Δ. The curve for Δ intersects the abscissa at a value of about 1.5% {221}. The twinning concentration in as-grown SOS films is rarely lower than this value.

All three curves in Fig. 4 show correlation of reflectance data with {221} content in the films, but it is clear that the ΔR_{280} data result in the steepest slope. Sufficient data have been collected to indicate that this term can be used for the qualification of SOS films. It is proposed, therefore, that the term ΔR_{280} be used instead of Δ as the quality control parameter for the assessment of SOS films. Not only is this term more sensitive to the defect structure of the films, but its usage effectively increases the signal-to-noise ratio of the measurement. For example, the noise level in measuring either ΔR_{280} or ΔR_{400} is about ± 1 unit. This can result in an uncertainty of ± 2 units in the term Δ, which can introduce a relatively large percentage error in Δ at low twinning concentrations. If the ΔR_{280} term is used instead of Δ, the noise level is still ± 1 unit but for a larger number, and the percentage error is relatively low.
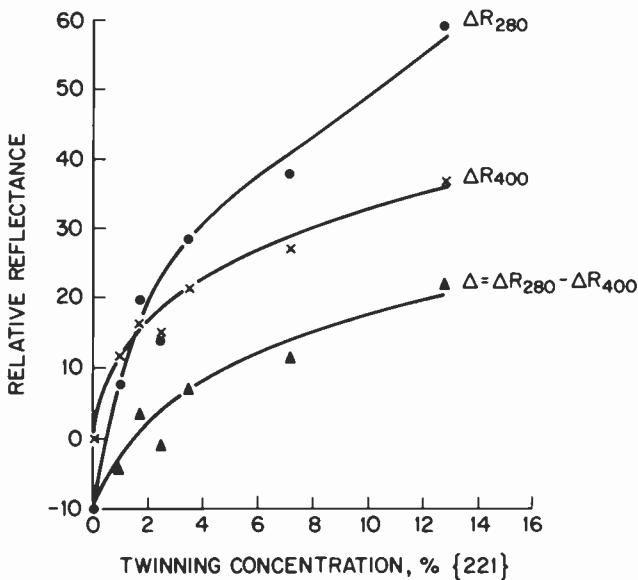
Fig. 4—Plot of relative reflectance versus twinning concentration for a set of SOS samples showing the dependence of ΔR_{280}, ΔR_{400}, and the difference term Δ, on the twin content of the films. The reflectance data at zero % {221} was obtained on a high-quality homoepitaxial silicon layer grown on a (100)-oriented silicon substrate. The reference reflector was a (100) silicon substrate.

Reference Wafers

It is important that the UV reflectometer be carefully calibrated and zeroed in measuring reflectance values. To measure ΔR_{280} the instrument is first calibrated by adjusting the gain to give a reading of 1400 units on the display when the black surface of the sample holder is placed in the optical path. This is a measure of the difference in reflectance between the silicon chopper blades and the nonreflecting surface of the sample holder (see Fig. 1). Thus, the ratio $(A-B)/A$ is set to 1400 units for calibration purposes. To zero the instrument, the ratio $(A-B)/A$ is electronically set to zero when a reference wafer of high-quality single-crystal silicon is placed in the sample holder.

The selection of this reference wafer is important, since all reflectance values subsequently measured relate to the reflectance of the reference wafer. The procedure we adopted in the past was to purchase high-quality (100)-oriented silicon substrates (5-10 Ω-cm) and compare the reflectance values for one lot of 25 wafers on the reflectometer using one of the wafers to zero the instrument. The

best silicon wafers giving the same value of ΔR_{280} were then set aside as reference wafers. One of these was then used for zeroing the instrument in subsequent measurements and was periodically checked against one of the unused companion wafers. If deterioration in reflectance was observed, a new reference wafer was used. It was found that attempts at cleaning or reconditioning the surface of the reference wafer was frequently unsuccessful. It should be noted that we are measuring small changes in reflectance, and small changes in the surface perfection of the reference wafer can introduce substantial error in the value of ΔR_{280} obtained on a given sample. For the same reasons SOS wafers should be evaluated prior to any processing or surface treatment. The elapsed time between film deposition and making reflectance measurements does not appear to be important provided the samples are kept clean.

An alternative to using as-received (100) silicon wafers as reference is to use homoepitaxial silicon films grown on (100) substrates. Good-quality homoepitaxial films have a higher reflectance than the substrates on which they are grown, possibly because of better surface crystalline perfection in the films than in the polished substrate surfaces. Choosing homoepitaxial silicon films as reference results in an increase of about 10 units in the value of ΔR_{280} for a given SOS sample. This corresponds to about 0.5% higher reflectance in the case of the homoepitaxial films than in the case of (100) substrates. The (100)-oriented reference films should be selected in the same manner as the (100)-oriented silicon substrates described above.

As indicated earlier, negative values of the reflectance parameter Δ are obtained for SOS films with low twin content. This is related to the surface perfection of the reference wafer used for zeroing the instrument. Use of a poor-quality reference surface will result in more negative values of Δ than use of a good-quality reference-wafer surface. The results presented in Fig. 4 were obtained after zeroing the reflectometer with a high-quality (100) silicon substrate. It can be seen that the curves for ΔR_{280} and ΔR_{400} cross over at a {221} concentration of about 1.5% (the crossover point can vary with film growth conditions). The value of Δ becomes zero, and negative for lower {221} concentrations. The data points shown when the {221} content is zero correspond to a high-quality homoepitaxial layer (6 μm, 5 Ω-cm) grown on a (100) silicon substrate. The value of ΔR_{280} is -10 units, the value of ΔR_{400} is zero, and the value of Δ is -10 units.

The fact that the ΔR_{280} curve drops off more rapidly than the ΔR_{400} curve at low {221} concentrations and becomes negative can

be attributed to the greater sensitivity of the ΔR_{280} term to crystallographic perfection of the films, both heteroepitaxial and homoepitaxial. If the homoepitaxial silicon layer had been used as reference for zeroing the reflectometer, the ΔR_{280} and Δ curves in Fig. 4 would be shifted upward by 10 units but the ΔR_{400} curve would remain unchanged. This happens because the instrument is nulled at both wavelengths. The net result is that negative values of Δ are eliminated by using a homoepitaxial layer as reference for zeroing the reflectometer. By adopting ΔR_{280} as the quality control parameter and a homoepitaxial layer as reference, the sensitivity of the measurement technique to SOS film quality can be increased substantially over the previous procedure. This can be seen by comparing the ΔR_{280} and Δ curves in Fig. 4. In addition, the ΔR_{280} measurement is applicable to all film thicknesses, unlike the Δ measurement.

Effect of Film Thickness

Plots of ΔR_{280} versus volume concentration of {221} are given in Fig. 5 for different film thicknesses [(100) homoepitaxial silicon reference]. A separate curve is obtained for each thickness because of the manner in which the volume concentration of {221} is expressed.[7] The density of microtwins in the films is highest in the vicinity of the sapphire substrate and usually falls off quickly with distance from the interface. In determining volume concentration, it is assumed for convenience that the microtwin density is uniformly distributed throughout the film thickness. Thus, if two films of different thicknesses have the same microtwin content, the thicker film will have an apparently lower volume concentration of {221}. If the categorization scheme shown in Fig. 2 is applied here and if we are primarily interested in category A material, then category A would correspond to about 0-4, 0-5, 0-6, 0-8, and 0-12% {221} volume concentrations in the case of film thicknesses 0.6, 0.5, 0.4, 0.3, and 0.2 μm, respectively. These percentages represent similar total {221} content in the films, and, for convenience, the assumption is made that this content is principally contained in the first 2000 Å of film thickness. The other categories can be assigned on a similar basis. The curves in Fig. 5 were obtained from scatter plots that are almost linear over the interval shown.

An estimate of the distribution of microtwins within the SOS films can be obtained from the data in Fig. 6. The volume concentration of {221} was determined for a set of samples with a film thickness of about 0.55 μm. The films were then thinned by plasma
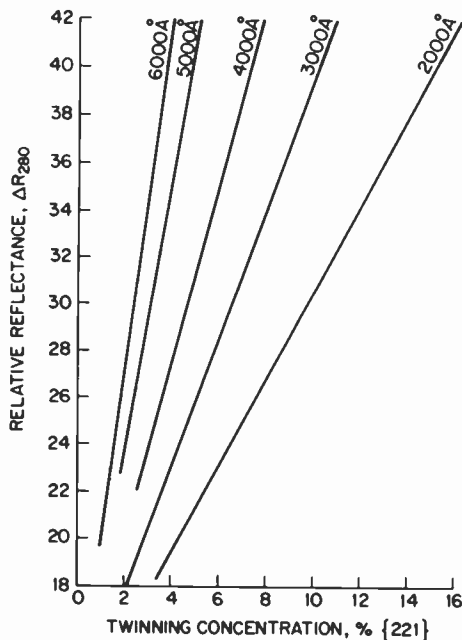
Fig. 5—Plots of ΔR_{280} versus {221} volume concentration for different film thicknesses. The reference reflector was a (100) homoepitaxial silicon film.

etching to a final thickness of about 0.25 μm and the twin content in each film again determined. The {221} concentration in each thinned film was then scaled, according to the original film thickness, to give the concentration that would be obtained if the twin content in the thinned film was distributed through its original thickness. The scaled {221} concentration values are plotted on the ordinate in Fig. 6 and the corresponding initial values on the abscissa. The dashed line, drawn with a slope of one, represents the relationship between initial and final concentrations in the films that would be obtained if there was no microtwin content in the 0.3 μm of film thickness removed by etching. The discrepancy between the two lines in Fig. 6 represents the twin content in the 0.3 μm removed by etching. It can be seen that about 20% of the {221} content of the films was contained in the upper 0.3 μm of film thickness. Strictly, this should be taken into account in determining the upper limit to category A in the categorization scheme described above for the different film thickness. Doing so would further complicate the evaluation procedure, however, and is not considered necessary.
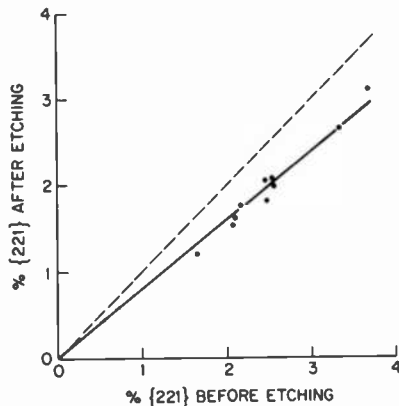
Fig. 6—Graph showing relationship between the volume concentration of {221} in a set of SOS films both before and after etching about 0.3 μm of film thickness. Initial film thickness was about 0.55 μm. The volume concentrations in the etched and unetched film were normalized to a film thickness of 0.55 μm. The divergence of the two curves is a measure of the twin content in the upper 0.3 μm of film thickness.

The results in Fig. 5 can be used to gain information on the relative influence of film thickness and defect content on the reflectance term ΔR_{280}. As indicated previously, both surface roughness and {221} content in the films can contribute to the value of ΔR_{280}. It may be expected that as the film thickness increases surface roughness also increases, leading to increased light scattering and increased values of the reflectance parameter. It is also conceivable that there is a relationship between the defect content in the films and surface topography. The relative contributions of these effects are not known.

The data in Fig. 5 can be rearranged in terms of total microtwin content in the silicon films rather than volume concentration of {221}. For example, film thicknesses of 0.6, 0.5, 0.4, 0.3, and 0.2 μm have the same total {221} content if their volume concentrations of {221} are 2.0, 2.4, 3.0, 4.0, and 6.0%, respectively. The values of ΔR_{280} (from Fig. 5) corresponding to those volume concentrations are plotted versus film thickness as curve 1 in Fig. 7. Curve 2 represents 1.5 times this content and curve 3 twice this content. The three curves cover the range assigned to category-A films described previously. It is interesting to note that doubling the twin content in the films, i.e., going from curve 1 to curve 3, causes an increase of 48% in ΔR_{280} for a film thickness of 2000 Å and an increase of 53% for a film thickness of 6000 Å. The increase in ΔR_{280} due to a
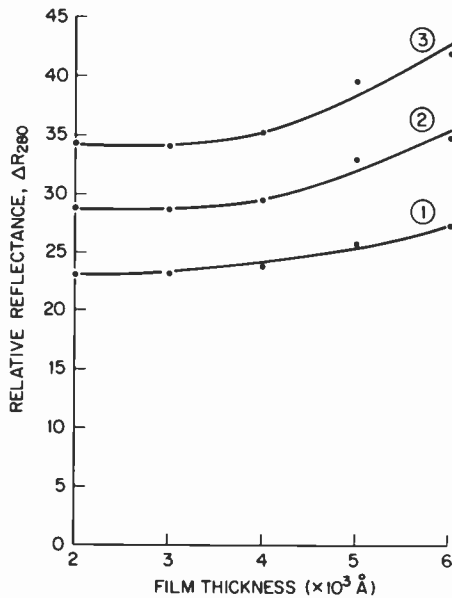
Fig. 7—Plots of ΔR_{280} versus silicon film thickness. Each curve represents a given total {221} content value irrespective of film thickness (see text for explanation).

three-fold increase in film thickness from 2000 Å to 6000 Å for curve 1 is about 19% and about 23% for curve 3. The empirical results in Fig. 7 support the following conclusions in relation to category-A films: (1) the major contribution to ΔR_{280} is caused by the defect content in the films and (2) increasing film thickness and associated surface roughness contribute to the value of ΔR_{280} to a much lesser extent than the defect content. The strong correlation between ΔR_{280} and defect content of the films provides the basis for using this term as reflectance parameter for quality control purposes.

If the above categorization scheme is employed, the corresponding values of the reflectance parameter ΔR_{280} can be determined from Fig. 5 for each film thickness. As already indicated, the values of ΔR_{280} in Fig. 5 are based on measurements made relative to a (100) homoepitaxial silicon film reference. If measurements are made relative to a (100) silicon substrate reference, the plots in Fig. 5 will be shifted downward about 10 units, and negative values of ΔR_{280} may be obtained for the best-quality SOS films. Either reference is acceptable, provided the reference used is indicated when values of ΔR_{280} are recorded. It is suggested that if a (100) silicon substrate reference is used, 10 units should be added to the measured value of ΔR_{280}. The plots in Fig. 5 can then be used directly for quality control purposes. It should be noted that negative values of ΔR_{280},

obtained when using a (100) silicon substrate reference, are a consequence of the reference used and not some idiosyncrasy of the instrumentation. A negative value of ΔR_{280} simply means that the reflectance of the sample is higher than the reflectance of the reference wafer used. The procedure outlined above should help both vendor and user in maintaining SOS film quality irrespective of film thickness.

Conclusions

A modified procedure for the optical characterization of silicon films on sapphire for quality control purposes has been developed. Specular reflectance measurements are made at a wavelength of 280 nm for assessing the quality of SOS films in the thickness range 0.2-0.6 μm. A (100)-oriented high-quality silicon homoepitaxial layer is used as reference for zeroing the UV reflectometer. A high-quality (100) silicon substrate can also be used as reference if 10 units are added to the measured values of ΔR_{280}. No change has been made in the reflectometer itself. The modified procedure increases the sensitivity of the reflectance technique for determining SOS film quality relative to the prior procedure.

Acknowledgments

References:

[1] P. J. Zanzucchi and M. T. Duffy, "Surface Damage and the Optical Reflectance of Single-Crystal Silicon," *Appl. Opt.*, **17**, p. 3477 (1978).
[2] Ch. Kuhl, H. Schlotterer, and F. Schwidefsky, "Optical Investigation of Different Silicon Films," *J. Electrochem. Soc.*, **121**, p. 1496 (1974).
[3] M. T. Duffy, J. F. Corboy, G. W. Cullen, R. T. Smith, R. A. Soltis, G. Harbeke, J. R. Sandercock, and M. Blumenfeld, "Measurement of the Near-Surface Crystallinity of Silicon on Sapphire by UV Reflectance," *J. Crystal Growth*, **58**, p. 10 (1983).
[4] G. Harbeke, E. Meier, J. R. Sandercock, M. Tgetgel, M. T. Duffy, and R. A. Soltis, "Rapid Characterization of Polysilicon Films by Means of a UV Reflectometer," *RCA Review*, **44**, 19 (1983).
[5] M. S. Abrahams and C. J. Buiocchi, "Cross-Sectional Electron Microscopy of Silicon on Sapphire," *Appl. Phys. Lett.*, **27**, p. 325 (1975).
[6] M. S. Abrahams, C. J. Buiocchi, R. T. Smith, J. F. Corboy, J. Blanc, and G. W. Cullen, "Early Growth of Silicon on Sapphire, I. Transmission Electron Microscopy," *J. Appl. Phys.*, **47**, p. 5139 (1976).
[7] R. T. Smith and C. E. Weitzel, "Influence of Sapphire Substrate Orientation of SOS Crystalline Quality and SOS/MOS Transistor Mobility," *J. Crystal Growth*, **58**, p. 61 (1982).

Optical Profilometer for Measuring Surface Contours of 1 to 150 Microns Depth

H. P. Kleinknecht and H. Meier
Laboratories RCA, Ltd., Zurich, Switzerland

Abstract—An optical profilometer is described for the touchless mea-
surement of surface contours of up to 150 μm in profile depth,
for which the usual interference techniques cannot be used.
The profilometer was originally designed for the measurement
of silicon power-device wafers, where 40–100 μm deep
grooves are used for electrically separating the individual de-
vices and for applying the passivating glass and oxide layers.
These grooves are produced by etching, which can give rough
surfaces, and must be monitored to ±2%. This optical profi-
lometer consists essentially of a high-power microscope
equipped with a laser attachment that automatically steers and
holds the microscope focused to the sample surface. The au-
tomatic focusing uses the beam of a He-Ne laser that is cou-
pled into the microscope by beam splitters and goes through
the objective lens to form a fine spot (0.5 μm) on the sample
surface. From there it is reflected back through the objective
and projected into a focus outside the microscope. The posi-
tion of this focus is a function of the sample surface height,
and it is sensed by an arrangement of apertures and photo-
diodes that drive a feedback servo-motor for microscope fo-
cusing. An electronic depth gauge (LVDT) resting on the
shoulder of the microscope measures the vertical excursions
of the microscope, which follow the sample contour.

1. Introduction

There are numerous cases in research, development, and manufac-
turing where one has to measure and monitor the surface contours
of polished, etched, or machined parts. Correspondingly, the number

of testing methods that have been developed for doing this is very large, and the choice of the proper method is dictated by the particular conditions and requirements. A very comprehensive literature list has been given by J. M. Bennett.[1] Of all the techniques used, the instruments using a mechanical stylus are the most direct.[2] In many instances, however, the possibility of damage to the sample by the stylus, the time requirement for such measurements, and/or the lateral resolution limit given by the stylus radius cannot be tolerated. In these cases, a touchless optical profilometer is required.

The original objective of the work reported here was the development of an optical profilometer to measure silicon wafers in power-device manufacturing. In particular, the essential dimensions of the surface contour of Si mesa transistor wafers and thyristors (Fig. 1) had to be monitored and controlled in the mesa-etch operation. This control is critical, because the depth of the moat surrounding the mesas affects the surface shape along the line, where the high-field region of the collector junction meets the surface. Therefore, this is the location where the passivating glass-SIPOS-oxide combination has to be effective for obtaining high-voltage capability of the device. (SIPOS is an acronym for semi-insulating polycrystalline oxygen-doped silicon.)

As indicated in Fig. 1, the moat depths range from 40 to 100 μm and have to be measured to ± 1 μm; the bottoms of the moats are rough, covered with etch pits, and are not planar at all. Hence,
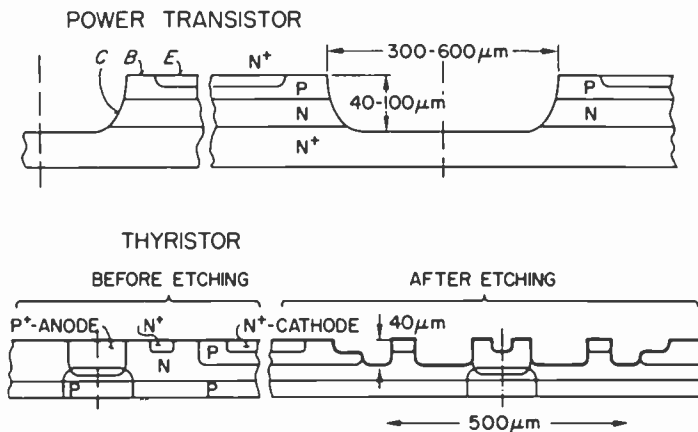
Fig. 1—Cross-sections of silicon power device wafers.

optical interference techniques[1,3] are not applicable. On the other hand, interference accuracies are not required.

Up to now the measurement of the moat depth was done in the factory with a light-section microscope[4] in which a sheet of light is obliquely (45°) projected on the sample and its trace on the sample surface is observed at right angle to the light sheet. The light trace following the surface contour can be measured with an ocular micrometer, but this is slow, subjective, and not very accurate.

In Sections 2 and 3, the principle of our optical profilometer is explained. Section 4 deals in a quantitative way with the optical design and Section 5 describes the complete system including the electronics. Test results and an assessment of the accuracy of the instrument are given in Section 6, where we also will point out a number of other applications besides Si power devices.

2. Approach

Our approach to the design of an optical profilometer for the above application essentially follows the schemes discussed in References [5] to [8]. It is outlined in Fig. 2. The beam of a He-Ne laser (λ = 0.6328 μm) is brought to a focus at "1" in Fig. 2, is coupled into a high-power optical microscope by means of a beam splitter cube, and is projected onto the sample surface at "2" by the objective lens L_1. The reflected laser light goes back through L_1 and, via a second beam splitter, to a focus at "3". The position of focus "3" along the beam is strongly dependent on the surface height of the sample, i.e.,
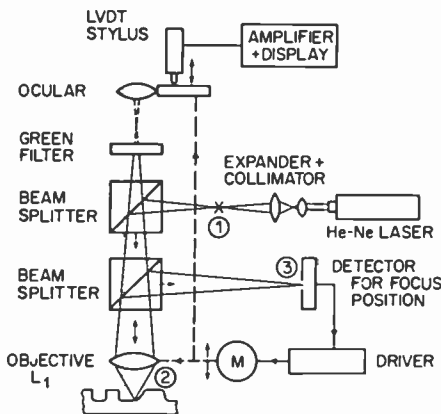
Fig. 2—Principle of the optical profilometer.

on the distance between the sample surface and the objective lens. For small changes in sample height, z, and for an objective magnification, M, one gets a change of the position of focus "3":

$$z_3 = M^2 2z. \qquad [1]$$

We use objectives with magnification between $M = 64$ and $M = 25.6$, which for a sample height change of $z = 1$ μm give focus changes, z_3, of 8 mm and 1.3 mm, respectively. The box in Fig. 2 called "Detector for Focus Position", which is an important part of our design, will be described in detail in the next section. It gives a dc signal, roughly proportional to z_3, which in a feed-back loop using a dc motor corrects the vertical microscope position such that the focus "2" is always kept at the sample surface. As the microscope follows the sample surface contour, its vertical movement is picked up by the stylus of an electronic depth gauge, a linearly variable differential transducer (LVDT) resting on the shoulder of the microscope.

Using this approach, the sample is kept stationary in space (except for the lateral scanning), as well as the laser, the beam splitters, and the focus detector. Only the microscope is moved up and down.[5] This arrangement enables us to make the sample stage, which sits on the base plate of the instrument, large and stable. However, this is in contrast to the "correct" way, which is to move the sample up and down to keep the surface in focus.[7,8] An elementary calculation shows that the microscope excursions in our case are equal to $z/(1 - M^{-2})$ instead of being equal to the sample height, z. However, the error is small, e.g., it is below 0.16% for $M = 25.6$, which is the lowest magnification used for a measurement.

The use of a complete microscope enables the operator looking through the eyepiece to select the desired measurement position on the wafer and to observe the laser spot on the sample during the test. For this purpose we use regular bright-field illumination with white light (not shown in Fig. 2) and observe through a green-filter (Fig. 2), which allows most of the white light to pass while most of the red laser light is blocked, such that the laser spot on the sample is visible but far too weak to do eye damage. Our choice of a Kodak Gelatin Filter No. 61 gives enough brightness for comfortable observation and keeps the laser radiation a factor of 10^3 below the limit allowed by the U.S. Center for Devices and Radiological Health. The distance of the focus "1" from the objective is designed to be equal to the tubus length of the microscope (256 mm). Therefore, with proper adjustment of the eye-piece, the sample appears sharp when the laser beam is focused on the sample surface.

3. Detection of Focus Position

There are basically two techniques for the detection of the longitudinal position of a focus such as the focus "3" in Fig. 2. The first one uses a small pin hole in front of a photosensor at the focus location. If the pin hole aperture is oscillated in the direction of the beam, the measured signal will sweep through a maximum.

Alternatively, one can oscillate the sample[7] or the lens.[5] By processing this signal with peak detection[5,7] or phase-sensitive detection,[10] one can get a dc signal proportional to the longitudinal focus position.

After some experimentation, we chose the second technique. We use two apertures and two sensors, one some distance in front of and one behind the focus to be measured.[6,8] This is shown in Fig. 3. One aperture uses a third beam splitter that deflects half of the intensity towards the closer sensor 1, while the other half goes straight towards the more distant sensor 2. The apertures covering the sensors are symmetrically located in a longitudinal position around the zero position of the focus.

The unfolded beam and the two apertures, S_1 and S_2, are sketched in Fig. 4a. In zero position, both sensors receive the same fraction of the laser intensity and the difference amplifier will give a zero signal. A forward deviation of the focus to "3" (z_3 in Fig. 4a) will favour the light falling on sensor 2, giving a positive signal, $P_2 - P_1$; a backward deviation will give a negative signal for $P_2 - P_1$. This difference can be used to drive the microscope up or down to bring the focus back to zero. The complete set-up including electronics, is shown schematically in Fig. 12 and will be elaborated in more detail in Section 5.

In principle this focus-position detector works with circular pin-hole apertures, S_1 and S_2.[6,9] However, as indicated in Fig. 5a, a problem is encountered when the sample surface is tilted. Under
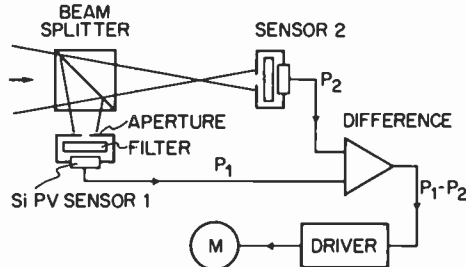
Fig. 3—Detector for focus position.
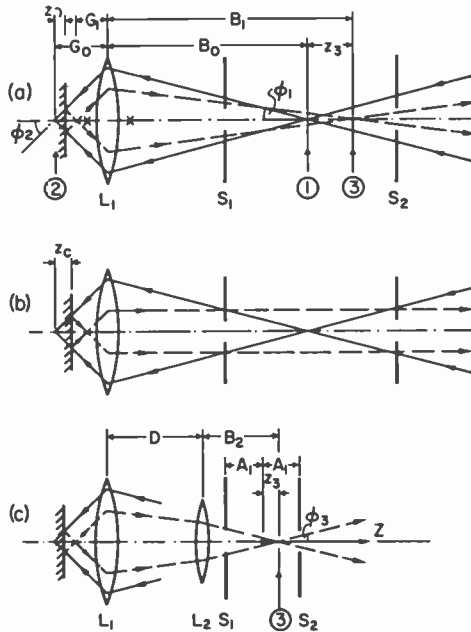
Fig. 4—Unfolded beams of the profilometer.

these circumstances, the reflected beam may partly or totally miss the aperture, giving a signal that is too low for measurement; as will be shown in the next section, this can also cause erroneous readings. Fortunately, the Si power-device wafers considered as measurement objects in our case have a surface tilt that is predom-
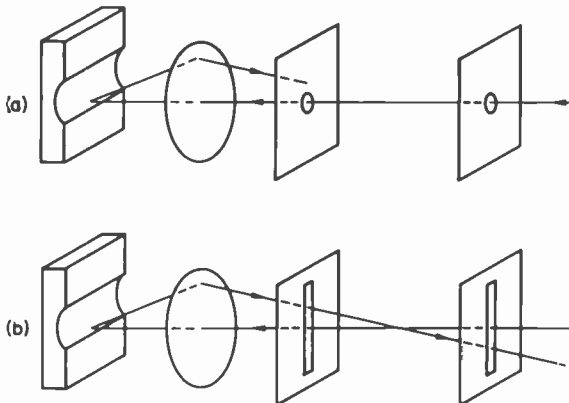
Fig. 5—The tilt problem: (a) pinhole aperture and (b) slit aperture.

inantly oriented in a plane perpendicular to the primary direction of the moat or the mesa edge. This is shown in Fig. 5b, where the moat runs horizontally and tilt is in the vertical plane. This kind of tilt can be accommodated to a large degree by using vertical slit apertures instead of pin holes. In practice it is always possible to rotate the wafer under test such that the moat to be measured lines up as in Fig. 5b.

4. Design Analysis and Optimization of the Optical System

In this section we describe in quantitative terms some of the problems and optical design details that had to be analyzed in order to optimize the parameters of the system.

In addition to what was said above, the acceptable tilt is limited by the numerical aperture of the objective, as indicated in Fig. 6. One can read from this figure that the maximal tilt is about as large or slightly larger than $\alpha/2$, where the numerical aperture is $NA = \sin \alpha$. Table 1 lists the various objectives used and their NA and α. The magnification, M, is the product of the $\times$-factor of the objective and the $1.6 \times$ tube factor due to the optical system in the tube of the particular microscope used. We also list the laser spot diameters, D_L, on the sample for best focus (i.e., the neck diameter at "2") with each objective, as estimated by observation through a calibrated eyepiece. This can be related to the convergence angle, ϕ_2, of the laser beam at focus "2" (see Fig. 4a). One has for a Gaussian beam[11]

$$D_L = \frac{2 \lambda}{\pi \phi_2} .$$ [2]

The angles ϕ_2 calculated from Eq. [2] are also listed in Table 1. They are seen to be close to α, which indicates that the laser-collimation combination has been set-up close to optimum for filling the whole lens aperture and getting the finest possible laser spot on the sample. The convergence angle ϕ_1 at focus "1" is equal to ϕ_2/M. The average of this value from all four rows of Table 1 gives $\phi_1 = 0.75°$ = 0.013 radians, which number will be used for the calculations
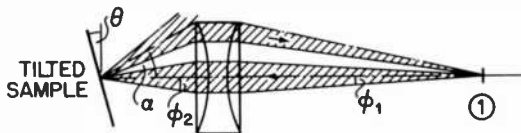
Fig. 6—Tilt and numerical aperture.

Table 1—Optical Parameters for Various Objectives

Objective	NA	α	M	D_L	ϕ_2	θ
$6.3\times$	0.12	$6.9°$	10.08	$3.0~\mu m$	$7.5°$	$4.7°$
$16.0\times$	0.35	$20.5°$	25.6	$1.3~\mu m$	$19.1°$	$11.6°$
$25.0\times$	0.40	$23.6°$	40.0	$0.8~\mu m$	$29.8°$	$15.1°$
$40.0\times$	0.85	$58.2°$	64.0	$0.45~\mu m$	$47.7°$	

below. The last column of Table 1 lists maximum tilt angles θ estimated as described in Section 6. θ is slightly larger than $\alpha/2$, as expected.

The next problem is the range of the sample surface height, z, within which the system can respond properly. In particular, if z is above a certain limit, z_c, the signal P_2-P_1 will reverse in sign, and the servo-system will run away. This can be explained from Fig. 4a and b which also defines some of the variables used here. In Fig. 4a one has $G_1 > F_1$ (the focal length of L_1), and $P_2-P_1 > 0$ for $z > 0$. However, as soon as the situation of Fig. 4b is reached, where $G_1 = F_1$, the focus "3" goes to infinity, and beyond that the beam becomes divergent leading to $P_2-P_1 < 0$ (for $z > 0$) causing runaway. Using the elementary relations

$$G_o = B_o/M \qquad [3]$$

$$F_1 = B_o/(M + 1) \qquad [4]$$

and reading from Fig. 4a the relation

$$G_1 = G_o - 2\,z, \qquad [5]$$

one obtains for $G_1 = F_1$ the critical z-value:

$$z_c = \frac{B_o}{2M(M + 1)}. \qquad [6]$$

For $B_o = 256$ mm (our microscope tubus length) and $M = 64$, one gets $z_c = 31~\mu m$, which is not satisfactory for our application. As a remedy for this we have added a weak additional convex lens, L_2, with focal length $F_2 = 150$ mm, in front of the third beam splitter a distance $D = 135$ mm from L_1 (see Fig. 4c).

Now by simple analysis one gets a critical sample height

$$z_c = \frac{B_o}{2\,M}\,\frac{B_o + F_2 - D}{B_o + (F_2 - D)\,(M + 1)}, \qquad [7]$$

which with the above numbers gives $z_c = 440~\mu m$. This is more than enough for our application.

With the insertion of the extra lens L_2 one also has to change Eq. [1], giving the position of focus "3", z_3, as a function of z for small z. Using the above analysis, one finds

$$z_3 = M^2\, 2\, z \left(\frac{F_2}{B_o + F_2 - D} \right)^2. \qquad [8]$$

This expression, with the above numbers, differs from Eq. [1] by a factor of 0.3 which means only a small sacrifice in sensitivity.

For larger excursions of z, the relation corresponding to Eq. [8] is no longer linear but still trivial to calculate. To compute (and optimize) the difference signal P_2-P_1 as a function of z, we had to calculate the fraction of the laser beam going through the two slit apertures. A Gaussian distribution was assumed for the laser beam and the intensity was taken to be diffraction limited.[11]

All of this was put on a PET computer, and the function P_2-P_1 = $f(z)$ was plotted for various parameters, such as M (magnification), F_2 (focal length of L_2), D (distance between L_1 and L_2), A_1 (distance of apertures from zero position of focus "3"), A (half of the slit width), and ϕ_1 (convergence at "1"). The optimization of these plots together with some experiments has resulted in the choice of parameters listed in Table 2. Fig. 7 gives the plots of P_2-P_1 versus z, as calculated for the parameters given in Table 2.

This function is the response of the focus detector. It is always positive for negative excursions z and negative for positive z, as required for feed-back control. Near $z = 0$ the curves are very steep, more so for higher magnifications than for lower ones. For very large z of either polarity, the signal becomes low, which limits the range particularly for high magnification. However, there is no runaway.

Fig. 8 gives experimental plots (solid lines) corresponding to the theoretical ones of Fig. 7. They were obtained by connecting the analog output of the LVDT to the x input of a recorder and connecting the output of the difference amplifier to the y input. The servo-loop was interrupted and the fine z motion of the microscope

Table 2—Choice of System Parameters Based on Optimization Calculations

Optical Tubus Length	B_0	256.0 mm
Magnification (Objective & Tube)	M	25.6–64
Focal Length of L_2	F_2	150.0 mm
Distance L_2 to L_1	D	135.0 mm
Distance S_1 to "3" = "3" to S_2	A_1	39.0 mm
Halfwidth of slits	A	0.25 mm
Convergence of input beam at "1"	ϕ_1	0.013 rad
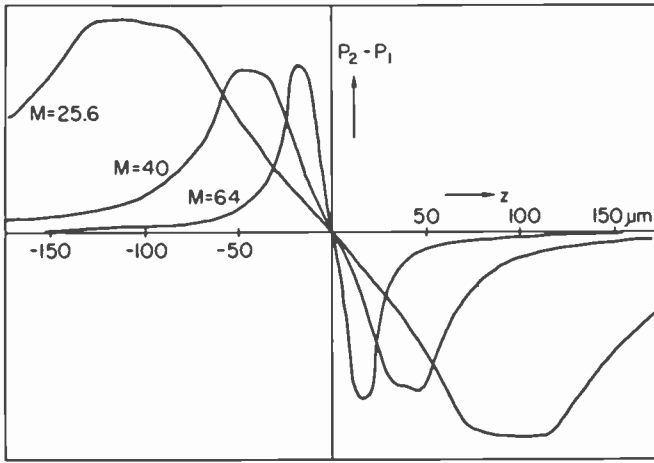
Fig. 7—Response function of the focus detector (theoretical curves).

was operated by hand. The theoretical curves from Fig. 7 (dotted lines in Fig. 8) were fitted to the experimental ones by choosing suitable amplitude factors. We have also inserted a factor (of 1.23) in the z axis (the same for all three magnifications) to obtain a good fit. With this correction, the agreement in curve shape and in the behaviour of the three objectives is seen to be good.

The above described PET computer program has been refined to include sample tilt in the plane perpendicular to the slit (perpen-
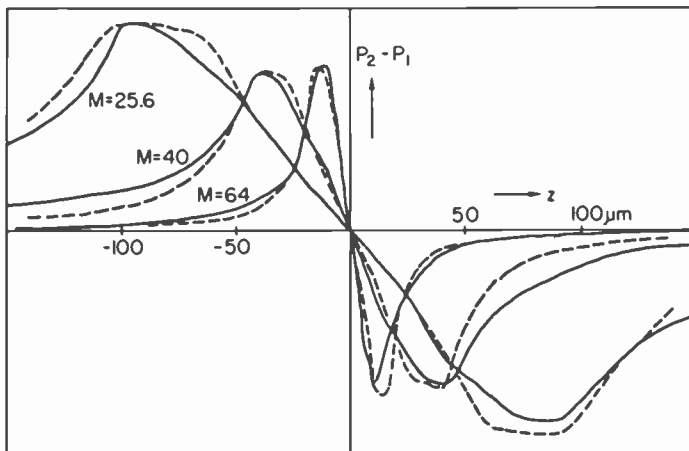
Fig. 8—Response function of the focus detector: experiment (solid lines) and theory (dotted lines).
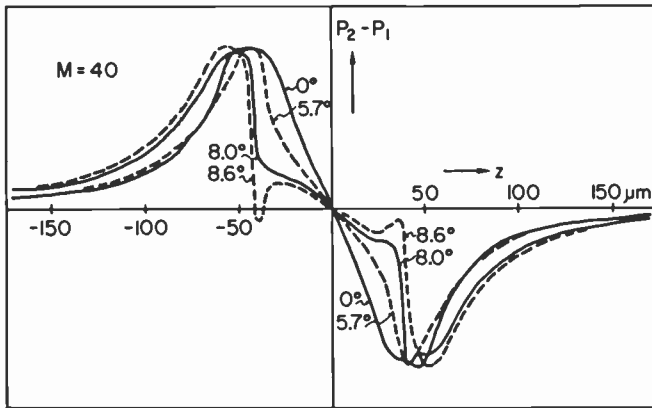
Fig. 9—Response function for tilted samples for $M = 40$.

dicular to the tilt direction, as indicated in Fig. 5). Fig. 9 is a plot
with different amounts of tilt for $M = 40$, indicating that for a tilt
above 8° the system can hook onto an erroneous value. Fig. 10 is
the same plot for $M = 64$, which shows that a much larger tilt can
now be tolerated, namely about 15°. Thus high magnification should
be used whenever coarse and tilted surfaces are to be measured.

So far the profilometer response has been treated for a perfectly
smooth sample surface. In other words, as drawn in Fig. 4a, the
beam was assumed to be specularly reflected and, for $z > 0$, to come
to a focus above the original focal point "2" as indicated by Eq. [5].

The other extreme would be a randomly scattering surface. This
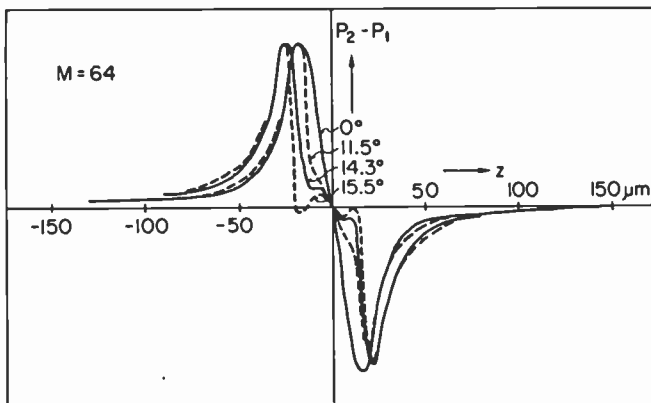
Fig. 10—Response function for tilted sample for $M = 64$.
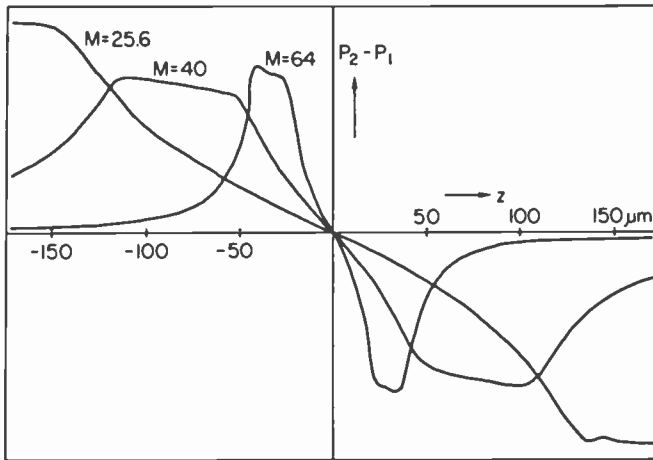
Fig. 11—Response function for a randomly scattering sample.

is equivalent to a small-area light source at the location of the sample, which means that Eq. [5] has to be replaced by

$$G_1 = G_0 - z. \qquad [9]$$

We have also assumed that the distribution of the back-scattered light is Lambertian and that the return beam is limited by the numerical aperture of the objective lens L_1. The result of this kind of calculation is plotted in Fig. 11. The comparison with Fig. 7 shows that, except for the slope at zero which is halved, there is no catastrophic difference.

5. The Complete System

Fig. 12 is a block diagram of the whole instrument. A 2-mW He-Ne laser ($\lambda = 0.6328$ μm) is used. We employ a Zeiss Epi microscope with a dc motor, M, attached to the fine focus control via a friction clutch. The lens L_1 consists of a $1.6 \times$ system built into the microscope tube and the objectives which can be exchanged with a revolver. The three beam splitters, the lens L_2, and the sensors 1 and 2 are mounted on a plate that is fixed in space and does not follow the z-motion of the microscope, as discussed in Section 2. Severe difficulties were encountered due to reflection of the laser beam from the glass-air surfaces of the beam splitters and the top of the $1.6 \times$ system. This problem was eliminated by tilting the beam splitter assembly by 4° (within the plane of Fig. 12) and also tilting

LVDT
STYLUS

MICROSCOPE
GREEN FILTER

COLLIMATOR

① LASER

M   L2   ③

SENSOR 1   SENSOR 2

L1

②   SAMPLE

XY STAGE

SUM   Σ   Δ   DIFFERENCE

COMPARATOR

FOCUS   LOW Σ

ZERO

DRIVER   FILTER

123.0   MEASURE
SIGNAL TOO LOW
OVER RANGE
UNDER RANGE

SYLVAC
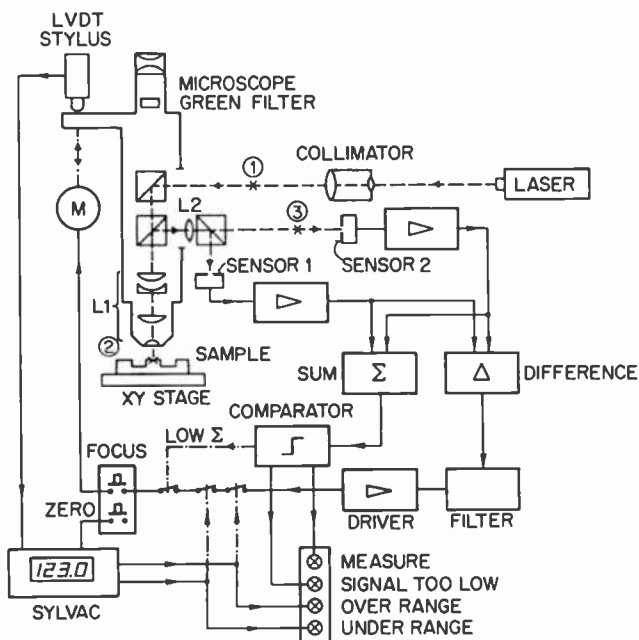
Fig. 12—Block diagrams of the complete system

the lenses of the $1.6 \times$ system by $2°$. This causes the surface reflexes to fall outside the slit apertures (the slits were oriented perpendicular to the plane of Fig. 12). The $2°$ tilt of the $1.6 \times$ system does not degrade the image quality noticeably.

Sensors 1 and 2 are enclosed in light-tight boxes with slit apertures, and line bandpass filters (Melles Griot 03 FIL 037) are inserted between slit and sensor. Thus no white light from the microscope illumination or room light can reach the sensors, while 75% of the laser light gets through. The sensor assemblies are mounted on little stages that can be adjusted in longitudinal direction and laterally perpendicular to the slit direction. All the light paths from the laser to the microscope and back to the sensors are enclosed in a light-tight compartment in order to fulfill laser safety requirements.

The sample stage has a fine x and y motion, operated from the side, and a flat unstructured table top on which large substrate plates of suitable thickness supporting the wafers under test can be moved and oriented by hand. The fast insertion and removal of the samples is facilitated by a large lever arm with which the microscope can be lifted in one step by about 10 mm. After insertion of

the wafer, the lever can be lowered to the z range, from which the automatic focussing can take over. Also, the lifting motion via a lever-operated shutter temporarily blocks the laser beam from getting out of the light-tight compartment and into the microscope and prevents laser radiation from escaping between objective and sample.

The light sensors are photovoltaic Si cells of 5-mm diameter. Their signals feed into dc amplifiers with the possibility for gain adjustment in order to adjust the zero-difference signal. The difference signal is further amplified by a driver stage that operates the servo-motor, M. It was found necessary to insert into the control loop an active "PID"-type filter in order to reduce the possibility of control oscillations. We have also provided for adjusting the loop gain for the same purpose.

The servo-loop is normally open, and it is closed only when the operator pushes the "Focus" button. This prevents time consuming run-away. Run-away is further avoided by a circuit that interrupts the loop for low signal. This can happen on a steep mesa slope or if the sample surface is too far away. For this purpose, the sum of the two sensor signals goes to a comparator that operates a relay switch to interrupt the feed-back loop for low signal. The comparator also controls suitable indicator lamps.

The vertical excursions, z, of the microscope are measured with a commercial LVDT Model SYLVAC D25, consisting of a stylus resting on the shoulder of the microscope and a digital LED display reading to tenths of microns. This display can be set to zero by operating the "Zero" push-button; from then on the LVDT reads the difference with respect to that z-value. The Sylvac digital unit also gives special signals when the reading is above a preset upper limit or below a preset lower limit. These signals are again used to interrupt the servo-loop in order to prevent the microscope excursions from going beyond safe limits and also to trigger indicator lights.

Fig. 13 is a photograph of the complete test set.

6. Quantitative Tests

Fig. 14 shows a recorder trace of a scan across a sample consisting of three steel gauge blocks (100, 75, and 50 μm thick) glued with nail polish to a flat Si wafer. The vertical coordinate of the trace comes from the analog output of the LVDT, and the horizontal is over time as the sample stage is driven with a synchronous motor. As can be seen by comparison with the vertical scale taken directly from the LVDT display, the traces check very well with the nominal
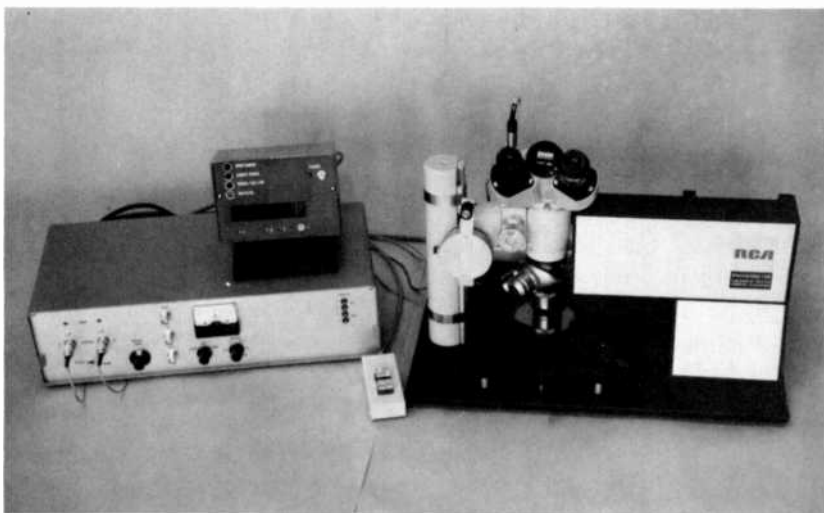
Fig. 13—The optical profilometer.

values of the gauge blocks if we subtract about 1 μm for the thickness of the glue. The circular points are transferred from a Dektak* trace taken of the same sample.

Fig. 15 is a trace taken in the same way across the surface of a cylindrical lens that had been sputter coated with aluminum. The trace is an ellipse, not a circle, because the x and y scales of our plot differ. The points on the ellipse are calculated assuming a perfectly circular cylinder with a radius (obtained by fitting) of 22.04 mm. The trace was done with a 25× objective and repeated with 16× and 6.3× giving small differences. The dashed horizontal lines indicate the points where the comparator gave "signal too low" and discontinued the measurement. This indicates, somewhat arbitrarily, the sample tilt at which the particular objective can no longer collect the reflected laser beam. These critical tilt angles (θ = arctan $[dy/dx]$ from Fig. 15) are the values listed in Table 1.

Other traces of the same kind for three objectives and a Dektak trace are given in Fig. 16 and 17. The curves are vertically displaced from one another for clarity. Fig. 16 is a trace of a Si wafer into which several steps have been cut by multiple passes with a diamond saw followed by heavy etching. The surfaces are still rather rough. As a consequence we see a lot of noise in the low-magnifi-

---

* Sloan Tech. Corp., 535 E. Montecito St., Santa Barbara, CA 93103.
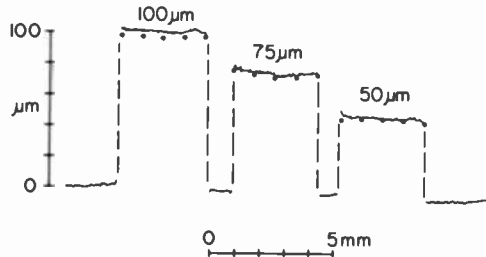
Fig. 14—Scan across three gauge blocks.

cation traces due to the local tilt as it was calculated in connection with Fig. 9, Section 4. The $40 \times$ curve is smooth and compares well with the Dektak trace. The oscillations in the deepest step are real, coming from the saw marks. Fig. 17 is a set of scans across a moat on a Si wafer of the type shown in Fig. 1.

When measuring power-device wafers (Fig. 1) in manufacturing, it is important to be able to measure through photoresist layers, because when the moat depth is tested, the mesa tops are still covered with photoresist so that the wafers can be re-etched if necessary. Fortunately, the laser beam is only weakly reflected from the air-photoresist interface (3%), while the reflectivity at the photoresist-Si interface is 20%. Hence, it is expected that the laser profilometer will look at the Si surface and not "see" the photoresist. This has been confirmed by demonstrating that visual observation through the ocular at high magnification using automatic focussing works on a photoresist covered wafer.

Tables 3 and 4 list a number of measurements made on two different kinds of single-moat wafers, one of them with photoresist
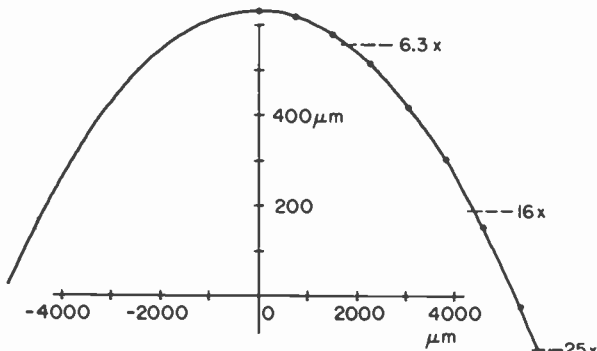
Fig. 15—Scan across a cylindrical lens.
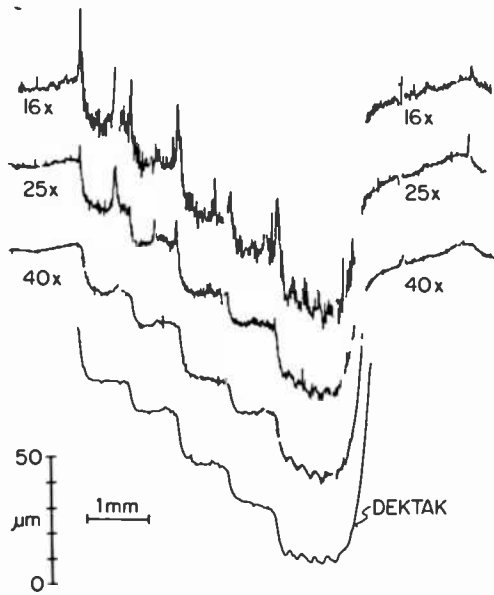
Fig. 16—Scan across steps on a Si sample.

covered mesa tops. Also shown are schematic sketches of the geometry indicating with arrows the points along the moat structure where the measurements were taken. These sets of measurements were repeated five times at locations near the periphery and in the
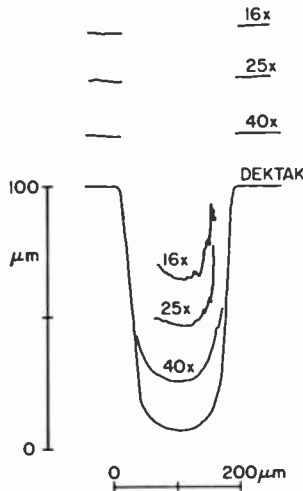
Fig. 17—Scan across a moat on a Si power wafer.

Table 3—Measurements at Various Locations on Wafer Type 9128 (No Photoresist, 16×). Depths in Columns from Top to Bottom Correspond to Positions Indicated by Arrows in Sketch.

Location on Wafer	Top	Right	Bottom	Left	Center
Depth	0	0	0	0	0
in μm	− 78	− 83			
	− 73	− 85	− 89	− 94	− 89
	− 83				
	+ 1	0	0	− 1	0
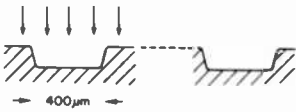
center of each wafer. The measurements of Table 4 were repeated using the 40× objective instead of the 16×. At each location on the wafer, the first measurement was done on the mesa top on one side, zeroing the display. Then one, two, or three measurements were done at the bottom of the moat, followed by a measurement at the mesa top on the other side. This last measurement should come back to zero if the wafer is smooth and the stage is leveled. The data show that it does so to a precision of ±1 μm. The values taken at the moat bottoms vary from one location on the wafer to another, because the moat depths do actually vary by a few μm. In Table 4

Table 4—Measurements at Various Locations on Wafer Type 6678 With Photoresist on Mesas. Depths in Columns for Each Objective Correspond to Positions Indicated by Arrows in Sketch.

Location on Wafer	Top	Right	Bottom	Left	Center
Depth in	0	0	0	0	0
μm; 16×	− 89	− 92	− 82	− 90	− 88
Objective	− 85	− 79	− 68	− 84	− 84
	− 93	− 95	− 87	− 93	− 90
	0	0	0	+ 1	0
Depth in	0	0	0	0	0
μm; 40×	− 89	− 92	− 82	− 88	− 87
Objective	− 89	− 82	− 65	− 84	− 85
	− 91	− 94	− 86	− 92	− 89
	0	0	+ 1	0	+ 1
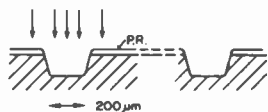
the repetition after switching from $16\times$ to $40\times$ was done as closely as possible at the same location, and the agreement of the two blocks of data, including the moat bottoms, is on the average also close to ± 1 μm. This indicates that our profilometer has a precision of ± 1 μm.

Tables 5 and 6 show similar data taken on multi-moat wafers with rough and pitted surfaces. The mesa tops in Table 6 were covered with photoresist. Again, the mesa-top values in Table 5 deviate on average by less than ± 1 μm. The corresponding values of Table 6 shows deviations of ± 2 μm. The differences between the $16\times$ and $40\times$ measurements are also somewhat larger in Table 6, namely ± 2 μm in the average. These larger deviations are due to the much larger nonuniformity of the sample of Table 6.

The precision of ± 1 μm derived from the above tests includes errors due to the nonuniformity of the surface and the limited precision of the sample stage. A direct test of the precision and accuracy inherent in the profilometer itself was made by mounting a planar mirror on a long lever arm whose height was controlled by a piezo-element (Fig. 18). The actual height change of the lever arm was measured with a second LVDT, which in a separate experiment had been found to agree within better than ± 0.1 μm. In this way, the mirror could be elevated in a controlled manner between 0 and 6 μm.

Fig. 18 gives the readings of the profilometer as a function of the "true" surface height of the mirror, as measured by the second

Table 5—Measurements at Various Locations on Wafer Type UT640 (No Photoresist, $16\times$). Depths in Columns from Top to Bottom Correspond to Positions Indicated by Arrows in Sketch.

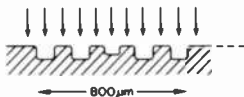| Location on Wafer	Top	Right	Bottom	Left	Center	T = Mesa Top, M = Moat
Depth	0	0	0	0	0	T
in μm	-32	-34	-36	-34	-36	M
	-1	-3	0	0	-1	T
	-29	-32	-33	-31	-34	M
	-2	-2	0	0	-2	T
	-18	-17	-14	-14	-20	M
	0	-1	0	0	0	T
	-30	-28	-33	-34	-34	M
	0	-1	0	-1	-2	T
	-34	-28	-31	-33	-35	M
	-1	-2	0	-1	-2	T

↓↓↓↓↓↓↓↓↓↓↓

←——— 800µm ———→

Table 6—Measurements at Various Locations on Wafer Type DUS370 with Photoresist on Mesas. Depths in Columns from Top to Bottom Correspond to Positions Indicated by Arrows in Sketch.

Location on Wafer	Top		Right	Bottom	Left	Center		Mesa
Objective	16×	40×	16×	16×	16×	16×	40×	Tops = T
Depth	0	0	0	0	0	0	0	T
in μm	−35	−36	−37	−35	−37	−34	−37	
	−46	−46	−44	−43	−46	−44	−45	
	−2	−3	−4	−1	−3	+3	−3	T
	−46	−48	−46	−40	−41	−42	−44	
	−32	−38	−35	−36	−34	−33	−37	
	0	−1	−1	0	0	−2	−1	T
	−18	−16	−15	−14	−17	−16	−16	
	−1	−2	0	−1	−2	−3	−1	T
	−38	−38	−37	−34	−38	−40	−39	
	−42	−44	−43	−35	−39	−42	−41	
	0	−4	+3	0	+3	−2	−3	T
	−53	−56	−52	−44	−53	−41	−52	
	−39	−41	−40	−35	−40	−39	−39	
	−2	−4	−2	+1	−3	+2	−2	T
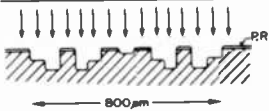
LVDT. The points are mostly averages of six measurements, three times going up and three times down. The deviations of these averages are less than ±0.1 μm for most points. The standard deviation of the six points from their mean is also about ±0.1 μm. This test was done with the 40× objective. A repeat measurement with 16× gave very similar results. From these tests, we conclude that the accuracy of the profilometer inherent in the optics and in the feedback loop (without sample movement) is better than ±0.2 μm.

As a follow-up on the calculations in Section 4 about surfaces with local tilt and extreme roughness, we have done a few tests with non-mirror, non-Si samples. For instance, we could measure the thickness of paper labels. Another non-Si sample was the measurement of Riston dry-film resist on a printed-circuit board (about 12 μm). This could be measured easily at steps of this resist on the copper plated front face as well as on the bare rear face of the board. Also, the thickness of metal layers on printed circuit boards could be measured.

More recently, we have built a high precision flexing stage for the profilometer and have measured the groove profiles in GaAs wafers to be used as substrates for constricted-double-heterojunc-
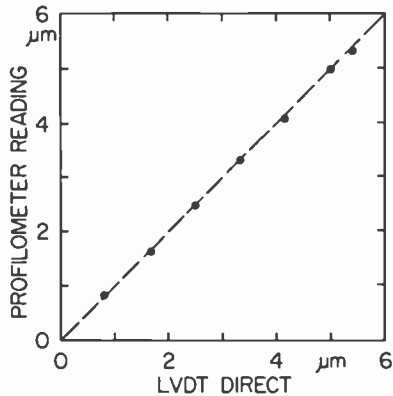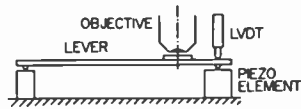
Fig. 18—Accuracy test of the profilometer.

tion AlGaAs lasers.[12,13] The groove depth of 3.5 μm could be traced with a precision of ± 0.2 μm. In another experiment, the profiles of refractive lenticular arrays etched into Si wafers to be used with infrared CCD focal plane arrays[14] were measured with the same precision.

7. Conclusions

We have developed a laser profilometer for optically reflecting or scattering surface contours in the range of 1 to 150 μm with an accuracy and a precision of about ± 1 μm. Accuracy is limited mostly by the surface quality of the samples and by the precision of the sample stage. The accuracy and the precision inherent in the optics and in the feedback was found to be five times better. The sampling area can be as small as 0.5 μm. Measurements can be made on surfaces with tilt angles with respect to the optic axis of up to 30° in one preferred direction and of up to 15° in any other direction. The larger tolerance against tilt in one preferred direction is the result of the use of slit apertures in the focus detector.

The instrument described above has been specifically designed for testing and monitoring the depths of the moats surrounding the mesas of Si power transistor and thyristor wafers in the manufacturing process. However, the same instrument, or the same prin-

ciple, can be applied to the measurement of surface profiles of other kinds of samples that are too deep and too rough to be handled by interference techniques.

Acknowledgment

References:

[1] J. M. Bennett, "Measurement of the RMS Roughness, Autocovariance Function and Other Statistical Properties of Optical Surfaces Using a FECO Scanning Interferometer," *Appl. Opt.*, **15**, p. 2705 (1976), and references therein.

[2] J. M. Bennett and J. H. Dancy, "Stylus Profiling Instrument for Measuring Statistical Properties of Smooth Optical Surfaces," *Appl. Opt.*, **20**, p. 1785 (1981), and references therein.

[3] G. E. Sommargren, "Optical Heterodyne Profilometry," *Appl. Opt.*, **20**, p. 610 (1981).

[4] H. E. Keller, "Quantitative Determination of Surface Topography by Light Microscopy," *Microscope*, **21**, p. 59 (1973).

[5] F. T. Arecchi, D. Bertani, and S. Ciliberto, "A Fast Versatile Optical Profilometer," *Optics Comm.*, **31**, p. 263 (1979).

[6] D. P. Bortfeld, I. Gorog, P. D. Southgate and J. P. Beltz, *RCA Engineer*, **26**, p. 75 (1980).

[7] D. K. Hamilton and T. Wilson, "Surface Profile Measurement Using the Confocal Microscope," *J. Appl. Phys.*, **53**, p. 5320 (1982).

[8] Y. Fainman, E. Lenz, and J. Shamir, "Optical Profilometer: A New Method for High Sensitivity and Wide Dynamic Range," *Appl. Opt.*, **21**, p. 3200 (1982).

[9] H. Hook and J. Bleacher, private communication.

[10] J. R. Sandercock, private communication.

[11] D. Marcuse, *Light Transmission Optics*, p. 232, Von Nostrand Reinhold Co., New York (1972).

[12] D. Botez, "CW High-Power Single-Mode Operation of Constricted Double-Heterojunction AlGaAs Lasers with a Large Optical Cavity," Appl. Phys. Lett., **36**, p. 190 (1980).

[13] Samples were provided by D. B. Carlin.

[14] H. G. Erhardt, J. Kane and L. S. O'Hara, *SPIE Proceedings*, p. 501 (San Diego, Oct. 22, 1984).

Rapid Evaluation of Submicron Laser Spots

M. T. Gale and H. Meier
Laboratories RCA Ltd., Zurich, Switzerland

Abstract—An instrument has been developed for the fast and accurate determination of the position and profile of a submicron focused laser spot, as required in optical disc recording systems and in the evaluation of diode lasers and associated optics. The measurement is based upon a scanning knife-edge technique using a novel crossed-grating chrome mask to enable both x and y spot profiles to be analyzed in a single scan. The mask pattern is also self-calibrating, enabling a very compact measurement head to be realized. A single scan and evaluation of the spot x,y widths and position is performed in less than 0.5 seconds, with an accuracy of about 0.03 microns and 0.5 microns respectively.

1. Introduction

A fast and accurate determination of the dimensions of a focused, submicron laser spot is becoming increasingly important in a number of rapidly developing optical technologies. One major area of application is in the development of injection laser systems to determine individual laser performance and to simplify the alignment of the collimation and symmetrizing optics. The requirement here is for a fast and accurate measurement of the spot diameter along the two major axes and the ability to perform this measurement at different positions along the optical axis in order to evaluate aberrations such as astigmatism. Another area of application is in optical-disc recording systems, where the size and quality of the focused spot critically affects the system performance and reliability. Optimum adjustment of the beam forming and focusing optics ideally requires almost instantaneous feedback of the resulting changes in the spot. In addition, the spot evaluation is preferably

performed in the actual machine (rather than on a removed optical sub-system), which imposes a further requirement of a compact measurement head that can be inserted to perform the measurement at the actual recording plane.

Commercially available instruments for measuring spot profiles and diameters do not satisfy all of these requirements. Instruments that sample the spot intensity using a scanning pinhole or wire[1] do not have the resolution required to evaluate submicron spots. More powerful instruments for lens testing and image evaluation[2] use a knife-edge scanning technique, but have measurement heads that are physically too large for this application and are too slow. We have therefore developed an instrument for the above applications that is accurate, compact, and relatively low-cost.

A number of different techniques have been investigated for measuring micron and submicron sized focused laser beams.[3,4] Knife-edge scanning techniques have the advantage of being simple and direct and are especially suited to the measurement of submicron beams. References in the literature describe various different forms of implementation of the basic technique.[5-8] A particular problem is the calibration of the exact knife-edge position, which is essential to an accurate measurement.

The instrument described in this paper uses a scanning transmission knife-edge technique in which the position information is determined using a novel grating-mask pattern to obtain a simultanous and calibrated measurement of a spot along 2 axes. A single scan and evaluation requires about 0.5 seconds and determines the spot widths and position to an accuracy of better than 0.03 and 0.5 microns, respectively. The measurement head is relatively compact and can be translated along the optical axis to obtain a complete analysis of the spot intensity pattern in the neighborhood of the best focus.

2. The Scanning Knife-Edge Technique

The essential features of the scanning knife-edge measurement are summarized here to provide a basis for the description of the instrument; further details can be found in References [5]–[8].

Fig. 1 illustrates the basic technique in one dimension. The focused light spot being measured is scanned by a knife-edge and the total transmitted power is monitored by a photocell during the scan. At any point during the scan, the transmitted power is given by

$$P(x) = \int_x^x I(x') \, dx',$$
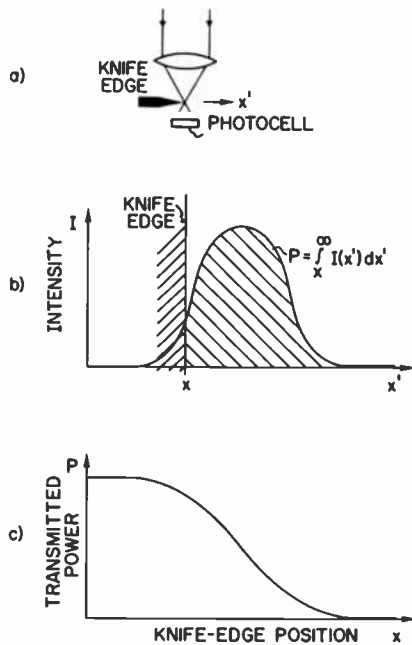
Fig. 1—Basic knife-edge measurement technique. A photocell monitors the total transmitted light power as the knife edge scans the laser spot (a). The spot intensity profile (b) is obtained by differentiating the measured photocell signal (c).

where $I(x)$ is the intensity distribution of the light spot and x is the position of the knife-edge.

Conversely, the spot intensity profile $I(x)$ can be obtained by differentiating the measured photocell signal:

$$I(x) = \left| \frac{dP(x)}{dx} \right|.$$

For two-dimensional spots, the same result holds provided (1) the spot has orthogonal symmetry, i.e., the intensity profile can be represented as

$$I(x,y) = I_1(x) \cdot I_2(y),$$

and (2) the axes of an elliptical beam are parallel to the instrument measurement axes.

The technique is thus ideally suited to the measurement of the circular, focused Gaussian beams of gas lasers, the intensity distribution of which can be written as

$$I(x,y) = \frac{2P_o}{\pi w^2} \exp\left(-\frac{2x^2 + 2y^2}{w^2}\right)$$

where P_o is the total laser power and w is the beam radius at $1/e^2$ intensity point.

For the elliptical beams of semiconductor lasers, care must be taken to orient the measurement (x,y) axes parallel to the ellipse axes; this generally does not present a problem since the major ellipse axis is perpendicular to the diode junction, which is well defined (usually parallel) with respect to the mounting surface. (This restriction could be overcome by making at least 3 knife-edge scans at different angles, from which the ellipse orientation and profile can be computed.)

The above analysis assumes that the total transmitted power is accurately measured by the photocell. The actual intensity distribution behind the knife-edge is an edge diffraction pattern and cannot be completely captured by a photocell of finite size. Firester et al have shown that for a 1% spot-width measurement accuracy, the acceptance numerical aperture (N.A.) of the photocell must be greater than about 0.85 of the N.A. of the spot-forming optics.[7] For example, measurement of an N.A. = 0.9 focused spot requires a photocell acceptance N.A. > 0.77, corresponding to an acceptance angle greater than $\pm 50°$. In practice this can be readily achieved by careful design of an integral knife-edge/photocell element.

A further consideration for measurement accuracy is the calibration of the knife-edge position or velocity. Calibration can be achieved using an interferometer to monitor the knife-edge displacement,[7] but this considerably increases the bulk and complexity of the measurement head. This problem has been solved by developing a novel knife-edge mask that produces a photocell signal with inherent calibration information during every scan.

3. Description of the Instrument

A diagram of the basic instrument is shown in Fig. 2. The heart of the instrument is a novel knife-edge mask glued directly onto a photocell, the combination being mounted on an oscillating arm. It, together with the galvanometer movement, the signal preamplifier, and the z-translation stage, constitutes the measurement head. A controller provides the drive signals and interfaces the photocell signal, via a fast A/D converter and RAM temporary storage, to a small computer that controls the measurement and analyzes the signal to obtain the x,y spot profiles and positions.
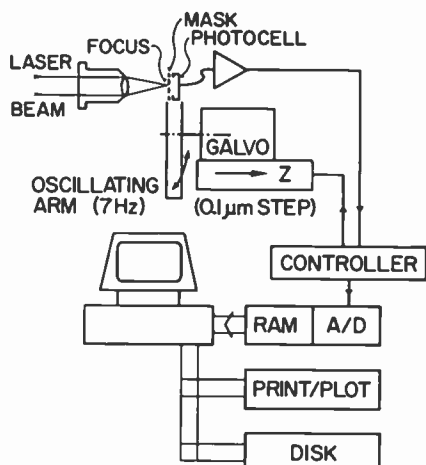
Fig. 2—Schematic of the basic spot-measurement instrument. The knife-edge mask is glued directly onto a photocell mounted on an oscillating arm.

3.1 Knife-Edge Mask

An important requirement in the evaluation of submicron focused beams is the essentially simultaneous measurement of the spot profile along the two orthogonal axes (x,y) perpendicular to the beam propogation direction (z). If the measurement head has to be physically rotated between x and y scans, the problem of maintaining the z positional information becomes acute; also the total measurement time is drastically increased. The basic knife-edge scan can be extended to two dimensions by scanning diagonally across two orthogonal edges. As shown in Fig. 3, the resulting photocell signal exhibits two corresponding slopes which, after differentiation, give the x and y spot profiles.

This concept has been extended to the knife-edge mask pattern shown in Fig. 4, which then can provide automatic velocity calibration of the knife-edge movement as well as distinguishing between the x and y information. The basic mask is fabricated in chrome on glass and is a relatively coarse crossed-grating pattern of 1-mm period in both directions. The figure shows only a small portion of the total mask, which is typically about 10 mm × 10 mm in size. The transparent lines are 20–30 microns in width (i.e., large compared to the spot size) and must have an extremely high edge definition—much better than one micron for the measurement of submicron focused spots.
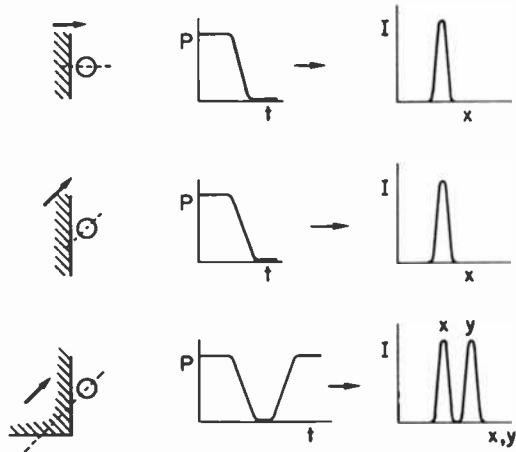
Fig. 3—One- and two-dimensional scanning modes. Horizontal or diagonal scans of a single knife-edge yield the one-dimensional profile $I(x)$. Diagonal scanning of two orthogonal knife-edges yields the complete profile $I(x)$ and $I(y)$.

As described in more detail in the next section, the mask is oscillated such that the laser spot periodically traverses, with constant velocity, a line scan similar to that shown in Fig. 4. The photocell signal during a single line scan, shown as a function of time
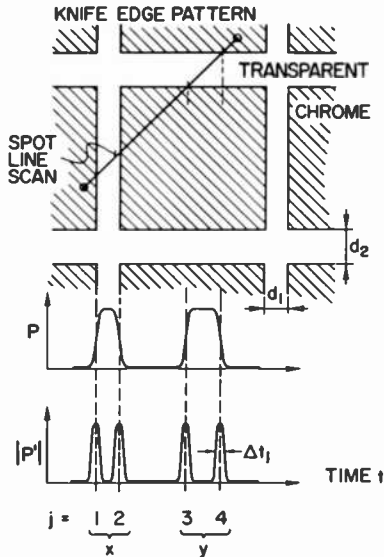
Fig. 4—Novel knife-edge mask pattern. The derivative of the photocell signal (P') yields calibration, position, and width information for both x and y dimensions in a single scan.

referenced to a start pulse from the scan drive electronics, consists of two broad peaks that contain the x and y information, respectively. Differentiation of this signal yields the x and y spot profiles (twice each) and the relative position of the spot with respect to the measurement head. Further, since the widths of the transparent grating lines d_1 and d_2 are accurately known, the separation of the differentiated x and y peaks furnishes a calibration of the (linear) mask velocity. The following information can thus be derived from the photocell signal during each scan:

• Knife-edge velocity calibration

$$v_x = d_1/(t_2 - t_1); v_y = d_2/(t_4 - t_3)$$

• Relative spot position:

$$x = v_x (t_1 + t_2)/2; y = v_y (t_3 + t_4)/2$$

• Spot profile and widths:

$$w_x = v_x \Delta t_1; w_y = v_y \Delta t_3$$
$$\quad = v_x \Delta t_2; \quad = v_y \Delta t_4$$

A consequence of using a periodic grating mask is that the required scan position over a horizontal and a vertical grating line is also repeated periodically over the mask, considerably facilitating the initial adjustment of the measurement head. Since the x and y scan information may be reversed if the scan line is at a different position on the mask, linewidths d_1 and d_2 are different (typically $d_1 = 20$ μm and $d_2 = 30$ μm), enabling identification of the x and y information by the photocell signal peak widths.

3.2 Measurement Head

The knife-edge mask and photocell detector are mounted on an arm (Fig. 5) that is oscillated at a frequency of about 7 Hz by a commercial galvanometer unit (General Scanning, Model G-300 PD) with integral position transducer. A triangular-wave drive signal is applied to the galvanometer, resulting in an oscillation of the arm with constant angular velocity. The measurement is performed at the center portion of the scan, well away from the area of velocity fluctuations due to the direction reversal at the ends of the scan. The arm radius (30 mm) is chosen such that the mask movement ($\sim$100 μm) can be considered to be a linear motion.

The knife-edge mask-grating pattern is fabricated by photolithography on a resist-coated chrome-on-glass blank using a high precision laser-writing exposure unit.[9] After etching and cutting to
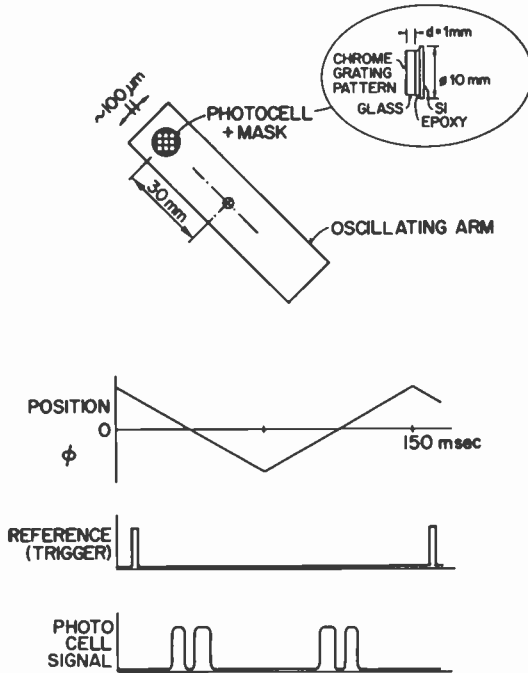
Fig. 5—Oscillating scanner arm and knife-edge mask/photocell combi-
nation. The curves show the angular arm position, the reference
signal for the x,y position, and the photocell signal as a function
of time.

size, the mask is glued directly to the surface of a 10-mm-diameter
silicon photocell (RCA type C30809). The effective mask-to-photo-
cell optical separation is then g/n, where g is the glass thickness
and n the glass index of refraction. With $g = 1$ mm and $n = 1.5$,
an optical separation of 0.6 mm is achieved, which easily satisfies
the numerical aperture requirement outlined above.

The photocell is connected by two flexible wires to a preamplifier
mounted behind the oscillating arm and above the galvanometer,
which in turn is mounted on a translation stage capable of about
0.1 μm positional accuracy. This enables the oscillating measure-
ment arm to be translated in the z (optical axis) direction and to
perform a measurement of the spot size at different z positions in
the neighborhood of the focus. Figs. 6 and 7 show photographs of
the measurement arm and complete head for the present instru-
ment. A further reduction in size could readily be achieved by rede-
signing the galvanometer and translation-stage components in the
head.
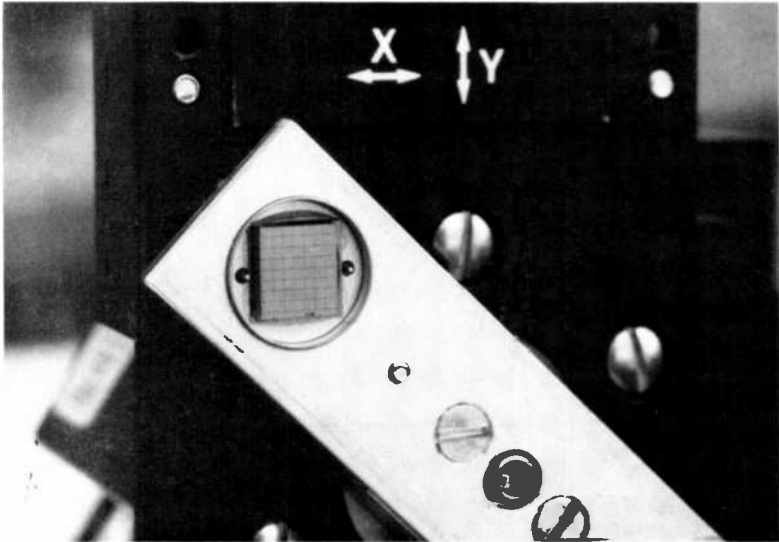
Fig. 6—Measurement arm showing grating knife-edge mask mounted on photocell. The mask is about 7 mm × 7 mm in size and oscillates with an amplitude of about 1 mm during the measurement.

3.3 Data Evaluation

The measurement head is connected by a flexible cable to the controller (Fig. 2) which houses a stable triangular-wave oscillator and driver for the galvanometer, a driver card and logic for the translation stage, and an amplifier for the photocell signal. This signal is then digitized (12 bits, 125 kHz) and stored in a RAM which can be addressed directly by the computer. The storage is initiated by a delayed reference pulse from the galvanometer drive oscillator circuit (Fig. 5), and 2000 samples in the region of interest are stored for any given scan. The sampling interval of 8 μsec corresponds to about 0.07 μm displacement of the knife-edge mask. The computer (currently a Commodore 8032 PC) initiates the data sampling of a scan and evaluates the digitized signal to determine the exact spot profile, widths, and position. A single scan and evaluation requires about 0.5 seconds; the x,y spot widths are determined to an accuracy of about ± 0.03 μm and the x,y spot position (relative to an arbitrary reference position) to an accuracy of about ± 0.5 μm. Higher accuracy can be obtained by averaging multiple scans.

Software routines also enable a number of other useful and time-saving features to be implemented. An automatic scan of the spot
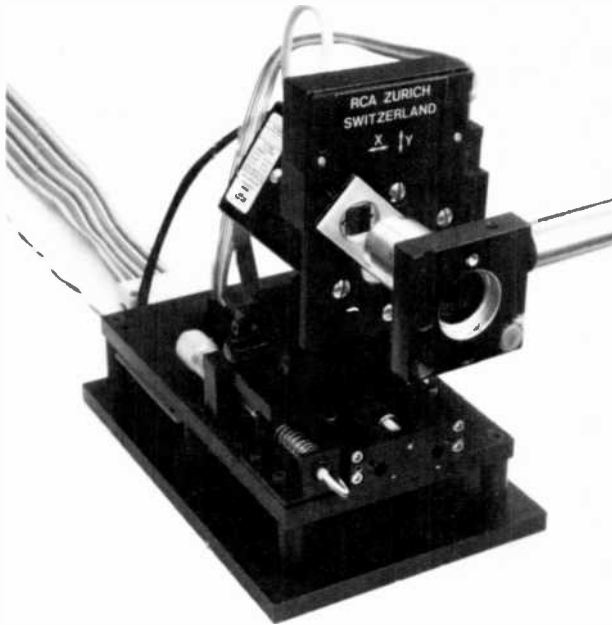
Fig. 7—Present measurement head showing oscillating arm, galvanom-
eter drive and z translation stage. In the foreground is an objective
forming the focused laser spot under evaluation.

parameters along the z axis enables the best focus to be rapidly
determined. Corresponding plots of the beam widths as a function
of the z-axis position allow rapid detection and evaluation of beam
ellipticity and astigmatism (Fig. 8), which is particularly useful for
diode laser systems. Table 1 summarizes the instrument perfor-
mance.

4. Results and Discussion

A prototype spot-measurement instrument has been in use within
RCA for more than one year, and has been found to be particularly

Table 1—Instrument Performance

Spot parameters:	
Single scan and evaluation time:	0.5 seconds
Spot widths W_x, W_y—accuracy:	0.03 μm
Spot position x,y,z—accuracy:	0.5 μm
Best focus:	
10 scans through region of focus in 1 minute	
Best focus (z) position accuracy:	0.1 μm
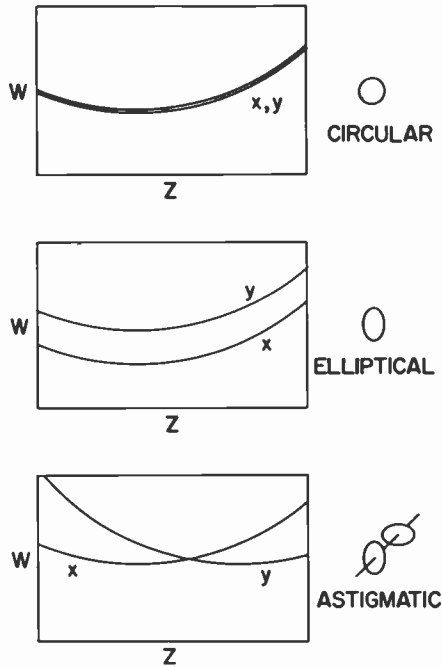
Fig. 8—A scan through the focus and display of the x,y spot widths as a function of the z position enables beam ellipticity and astigmatism to be rapidly assessed.

useful in the area of diode-laser systems and the alignment and testing of the associated collimation and focusing optics. Fig. 9 shows a typical measurement of the focused beam from a CDH-LOC laser[10] after collimation, symmetrizing, and focusing with an objective of N.A. = 0.65. The x and y spot widths are $w_x = 0.69$ μm and $w_y = 0.72$ μm (with an estimated accuracy of ±0.03 μm), showing an excellent symmetrizing of the elliptical diode-laser output beam. This information, together with the position of the spot with respect to an arbitrary reference position, is obtained in 0.5 seconds once the measurement head has been positioned. The effect of adjustments to the optics, or variations in the diode-laser output pattern due to changes in temperature or drive current, are detected and displayed within the same short time, considerably facilitating the investigation of these parameters.

Fig. 10 shows the measured x and y spot widths for the same laser as a function of the position along the optical axis (z), obtained in about 1 minute. The curves show the lack of astigmatism in the focused beam and confirm the circular nature of the spot; they also
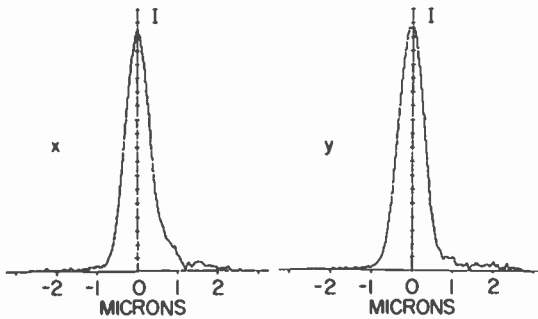
Fig. 9—Measured x,y intensity profiles for the focused spot (objective N.A. = 0.65) from a diode laser. The spot widths (full width at the 50% intensity points) are w_x = 0.69 μm and w_y = 0.72 μm.

enable the position of best focus to be determined to an accuracy approaching 0.1 μm.

The intensity distribution of a beam in the neighborhood of the focus can be studied in detail. Fig. 11 shows the measurement for a truncated HeNe laser beam focused by a N.A. = 0.9 objective. The spot profile at the focus (a) shows the appearance of the Airy disc around the central spot due to the beam truncation, and a complete scan through the focus (b) shows the z variation of the diffraction pattern and best focus position.

The experience to date with this spot-measurement instrument shows that it is relatively easy to align, sufficiently compact to be used in most practical situations, and has enabled the time required to evaluate the important characteristics of a focused laser spot to
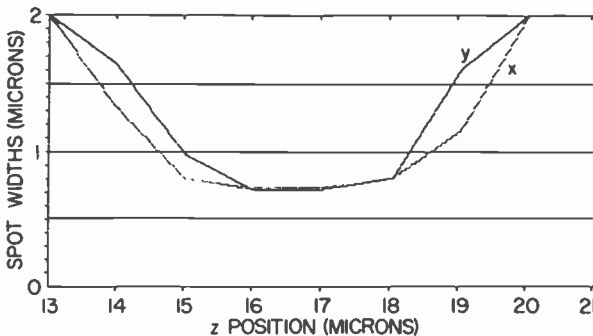
Fig. 10—X and Y spot widths for the laser of Fig. 9 as a function of the z position in the neighborhood of the focus. Note the circular spot with virtually no astigmatism.
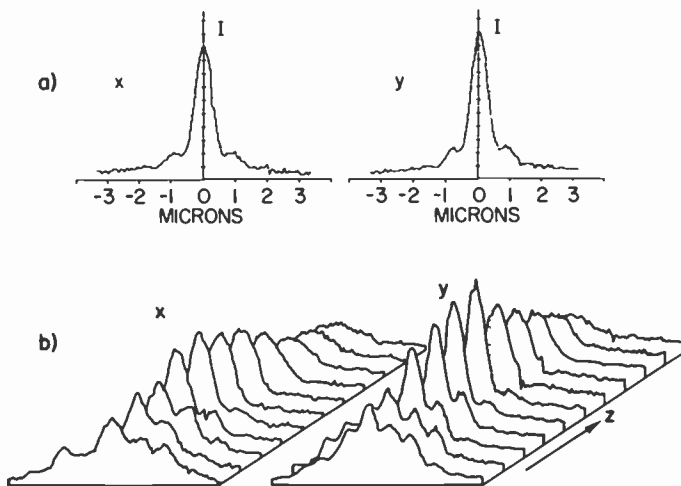
Fig. 11—Measured *x,y* intensity profiles (a) for the focused spot (objective
N.A. = 0.9) from a truncated HeNe laser beam. A scan through
the focus (b) shows the local variation in spot profile.

be drastically reduced. The ability to observe the effect of adjust-
ments to collimation, symmetrizing, and focusing optics in essen-
tially real time has also proved a very valuable feature and has
important applications in the development and construction of op-
tical-recording and diode-laser systems.

Acknowledgments

References:

[1] *Laser Beam Analyser*, ALL Applikationslabor fuer Lasertechnik, Munich, Ger-
many.
[2] *2000 Mark II OTF Analysis System*, Tropel, Fairport, NY.
[3] M. B. Schneider and W. W. Webb, "Measurement of Submicron Laser Beam
Radii," *Appl. Opt.*, **3**, p. 1382 (1981).
[4] D. K. Cohen, B. Little, and F. S. Luecke, "Techniques for Measuring 1-micron
Diameter Gaussian Beams," *Appl. Opt.*, **23**, p. 637 (1984).
[5] J. A. Arnaud et al, "Technique for Fast Measurement of Gaussian Laser Beam
Parameters," *Appl. Opt.*, **12**, p. 2775 (1971).
[6] Y. Suzaki and A. Tachibana, "Measurement of the Micron Sized Radius of Gaus-
sian Laser Beam Using the Scanning Knife-Edge," *Appl. Opt.*, **14**, p. 2809 (1975).

[7] A. H. Firester, M. E. Heller, and P. Sheng, "Knife-Edge Scanning Measurements of Subwavelength Focused Light Beams," *Appl. Opt.*, **16,** p. 1971 (1977).

[8] J. M. Khosrofian and B. A. Garetz, "Measurement of a Gaussian Laser Beam Diameter Through the Direct Inversion of Knife-Edge Data," *Appl. Opt.*, **22,** p. 3406 (1983).

[9] M. T. Gale and K. Knop, "The Fabrication of Fine Lens Arrays by Laser Beam Writing," *SPIE*, **398,** p. 347 (1983).

[10] D. Botez, "CW High-Power Single-Mode Operation of Constricted Double-Heterojunction AlGaAs Lasers with a Large Optical Cavity," *Appl. Phys. Lett.*, **36,** p. 190 (1980).

A Dynamic Antivibration Support

J. R. Sandercock, M. Tgetgel, and E. Meier
Laboratories RCA Ltd., Zurich, Switzerland

Abstract—In many sensitive instruments and production machines, the achievable resolution is limited by the ever-present building vibrations. A new dynamic isolation system is described that effectively removes these vibrations and has clear advantages over the traditional soft passive isolation system.

Introduction

Certain delicate machines and instruments can be rather sensitive to external vibrations. Generally there are two distinct effects—high-frequency vibrations, which may excite a mechanical resonance in some part of the machine or its supports, and low-frequency vibrations, which tend to produce a nonresonant distortion of the basic structure. The first effect occurs typically at frequencies in the range of 100–1000 Hz and can often be effectively eliminated by the simple expedient of mounting the system on thin rubber. Low-frequency vibrations, which typically are driven by building vibrations and are in the range of 2–25 Hz, are much harder to eliminate and some sophisticated passive antivibration mounts have been developed for this purpose.* It is these low-frequency vibrations that will be addressed in this paper. A new dynamic isolation system is described in detail and compared with the commercially available passive systems.

Passive Isolation

The simplest method of vibration isolation consists of mounting the device to be isolated on a resilient support. Consider such a mount

---

* See, for example, the catalog of the Newport Corporation, Los Angeles, CA, for a good description of a passive air suspension with the isolation properties of a compound spring.
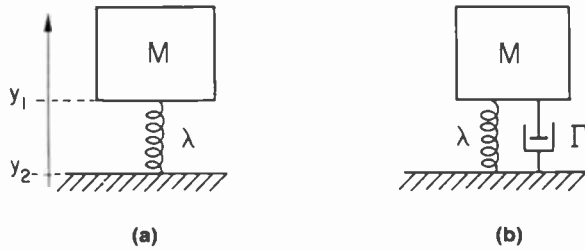
Fig. 1—(a) Simple passive isolation and (b) passive isolation with damping.

consisting of a mass M supported on a spring of force constant λ as illustrated in Fig. 1(a). Of interest is the vertical movement y_1 of the mass M in response to a movement y_2 of the supporting surface. If y_2 is a harmonic displacement with angular frequency ω and amplitude a_2, then the response y_1 is also harmonic with amplitude a_1:

$$y_1 = a_1 e^{i\omega t},$$

where it is straightforward to show that

$$\frac{a_1}{a_2} = \frac{1}{1 - \dfrac{M\omega^2}{\lambda}}. \qquad [1]$$

At high frequencies, the second term in the denominator is large and a_1 therefore is small, i.e., high-frequency isolation is good. However, at a frequency ω_o given by $M\omega_o^2/\lambda = 1$, the amplitude a_1 becomes infinite, and some damping must clearly be introduced in a practical device.

In the damped system of Fig. 1(b) there is a viscous force F acting with amplitude

$$F = \Gamma\lambda \frac{d}{dt}(y_1 - y_2),$$

and the response of the damped system is

$$\frac{a_1}{a_2} = \frac{1 + i\Gamma\omega}{\left(1 - \dfrac{\omega^2}{\omega_o^2}\right) + i\Gamma\omega}. \qquad [2]$$

The amplitude a_1 is now complex (phase shifted), but the amplitude at resonance is reduced to

$$\left|\frac{a_1}{a_2}\right|_{\omega = \omega_0} = \left(1 + \frac{1}{\Gamma^2\omega_o^2}\right)^{1/2}. \qquad [3]$$

In practice the choice of damping Γ is a compromise between low resonant amplitude (Eq. [3]) and sufficient high-frequency isolation. Eq. [2] shows that for the high values of Γ needed for low resonant amplitude, the amplitude a_1/a_2 tends to unity, i.e., there is no attenuation of the vibration amplitude. A practical compromise is obtained with $\Gamma \simeq 1/(3\omega_o)$.

While more complex spring systems can offer better high-frequency isolation, the problem of the buildup of amplitude at resonance remains.

Dynamic Isolation

The dynamic antivibration system to be described here comprises units consisting of the combination of an accelerometer with an electromechanical transducer. Such a unit is illustrated in Fig. 2. The accelerometer consists of a mass m resting on a piezoelectric disc P, the whole being supported by a bracket B on the device of mass M to be isolated. The electromechanical transducer LS (e.g., a modified loudspeaker) allows a variable force to be applied to the underside of the bracket. The force and the measured component of acceleration are collinear. In parallel with the electromechanical transducer is a spring of force constant λ which supports the weight of the body to be isolated.

Since the mass m is supported only by the piezoelectric disc P, the voltage V developed across P is proportional to the absolute acceleration (d^2y_1/dt^2) of the mass m. This voltage is integrated to produce a current $I \sim \int V dt$, which produces a force $k_2 I$ in the electromechanical transducer, where k_2 is a constant. The equation describing the motion of the unit is therefore (assuming $M \gg m$):
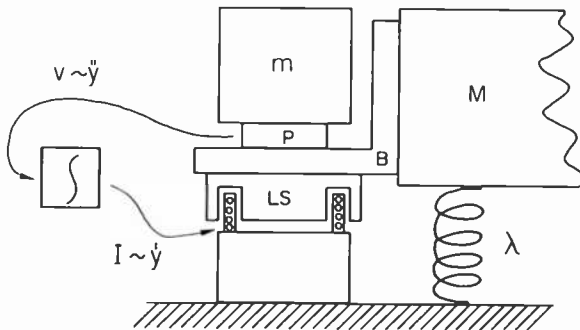
Fig. 2—The principle of dynamic vibration isolation.

$$M \frac{d^2y_1}{dt^2} = -\lambda(y_1 - y_2) + k_2 I,$$

where

$$I \propto \int V dt \propto m \int \frac{d^2y_1}{dt^2} dt \propto m \frac{dy_1}{dt}$$

or

$$k_2 I = -k_1 m \frac{dy_1}{dt},$$

where k_1 is a constant determined by the gain of the integrator. Therefore

$$M \frac{d^2y_1}{dt^2} = -\lambda(y_1 - y_2) - k_1 m \frac{dy_1}{dt},$$

from which it is straightforward to show that the amplitude a_1 of the response to a driving amplitude $y_2 = a_2 e^{i\omega t}$ is

$$\frac{a_1}{a_2} = \frac{\lambda}{(\lambda - M\omega^2) + ik_1 m\omega}. \quad [4]$$

The amplitude a_1 therefore decreases with increasing values of k_1 (gain).

Comparison of Dynamic and Passive Isolation

There are two very important and fundamental differences between dynamic and passive isolation systems.

[1] It is seen from Eq. [2] (as discussed above) that for the passive system Γ may not be too large if isolation is to be effective. On the other hand, Eq. [4] shows that for the dynamic system the damping term may be arbitrarily large (large k_1) with the isolation improving with increased damping. This distinction arises because for the passive case damping is proportional to the *relative* velocity between mass and floor, while for the dynamic case the damping is proportional to the *absolute* velocity. An absolute velocity may be thought of as a velocity relative to a virtual inertial plane. Thus, as illustrated in Fig. 3, high damping in the dynamic system is equivalent to strong coupling to an inertial reference frame and, therefore, the stronger the coupling the better the isolation.

[2] We consider the effect of a force $F = F_o e^{i\omega t}$ applied directly to
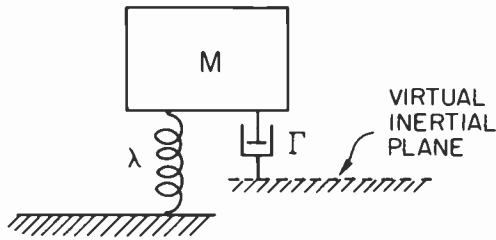
Fig. 3—Illustration of damping with respect to a virtual inertial plane.

the supported mass M. It is easy to show that for the passive case, a displacement a_1 is produced where

$$a_1 = \frac{F_o}{M[\omega^2 - \omega_o^2 + i\omega_o^2\omega\Gamma]};$$ [5]

for the dynamic case, the corresponding expression is

$$a_1 = \frac{F}{M\left[\omega^2 - \omega_o^2 + i\omega\dfrac{k_1 m}{M}\right]}.$$ [6]

If we set $\Gamma = 1/(3\omega_o)$ in Eq. [5] (for the passive case), it is apparent that at frequencies $\omega \gtrsim 3\omega_o$ the amplitude does not differ appreciably from the value $F/M\omega^2$ appropriate to an unconstrained mass M. In other words a passively supported mass is effectively *unconstrained, or floating*. On the other hand, due to the large value of k_1 in Eq. [6], at all frequencies except the highest the amplitude a_1 is very much less than $F/M\omega^2$, so that in the dynamic case the mass is held essentially rigid.

In designing a practical device based on the above principle three points must be borne in mind. First, the device discussed above isolates in one direction (and at one location) only. A minimum of six such devices must be attached to the body to be isolated since the body has six degrees of freedom (3 translational, 3 rotational).

Second, the gain of the feedback loop cannot, in practice, be increased indefinitely. At some point the gain at high frequencies, where mechanical resonances cause phase shifts, will be high enough to cause oscillation. Rigid construction is required to place these mechanical resonances at sufficiently high frequencies. Note that this only applies to the unit comprising the accelerometer and electromechanical transducer; resonances in the supported body will not cause oscillations.

Third, the ideal integrator assumed in the feedback loop would have infinite gain at $\omega = 0$ and thereby cause severe noise problems at ultralow frequencies. In a practical device, the feedback loop should have zero gain at $\omega = 0$.

Detailed Construction

In principle the dynamic isolation elements can be attached to any rigidly constructed and resiliently mounted body. The design below applies to a general purpose table that, in its prototype form is capable of supporting loads up to about 300 kg, but it can be straightforwardly scaled to one that will support larger loads.

Referring to Fig. 4, the table top is supported near its corners on four supports, each consisting of a resilient rubber block R and a base S. The thickness and area of the rubber blocks are chosen so that the vertical resonant frequency of the table top plus supported mass lies in the range 10–30 Hz.

Antivibration elements are attached at various points to the table top as indicated by the arrows. A minimum of six are required but more may be used, for example, to increase the correction forces available. A convenient arrangement involving eight elements is illustrated.

The design of each element is illustrated in Fig. 5. A bracket B attached to the table top supports an electromechanical transducer LS on its lower surface and an accelerometer A on its upper surface. The transducer LS supplies a force proportional to the applied current. For this purpose a loudspeaker is used with a block C glued to the center of the cone in intimate contact with the voice coil. The force provided by the transducer and the component of acceleration measured by A both lie along the common axis of A and LS. Since the force must act between the floor and the bracket B, the end of the transducer remote from the bracket B must be coupled to the
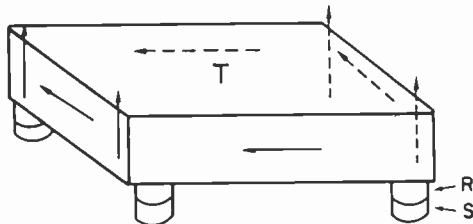
Fig. 4—Resiliently mounted table top with eight antivibration elements indicated by the arrows.
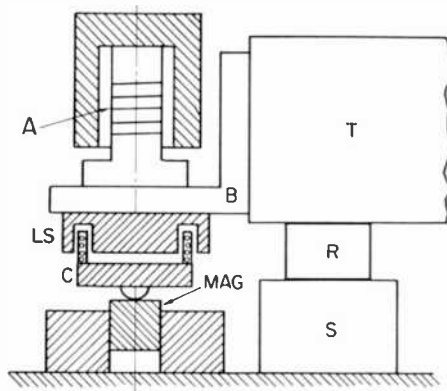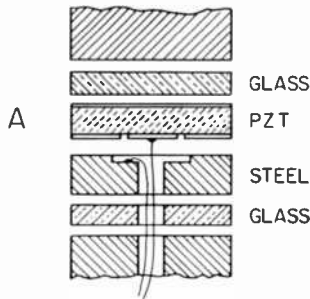
Fig. 5—(a) Detailed construction of antivibration element and (b) exploded view of thermally compensated accelerometer.

floor in such a manner that the coupling is rigid in the direction of the common axis of A and LS and compliant perpendicular to this direction. The transverse compliance is simply achieved by attaching to the block C a steel ball, which rests on and is firmly held by the magnet (MAG). During a transverse displacement, the block C plus ball rocks on the magnet, causing a rotation of the loudspeaker voice coil. During an excessive transverse displacement, the ball may slide on the magnet, thus preventing damage to the loudspeaker.

The magnet itself is held in a friction coupling which allows it to slide along the common axis of A and LS whenever a certain force is exceeded. Clearly this frictional force must be less than the magnetic coupling force between ball and magnet, but must be greater than the maximum force generated by the transducer LS. The above combination of ball, magnet and friction coupling forms a completely self-aligning coupling between the floor and the transducer LS.

The vibration element depicted in Fig. 5 acts in the vertical direction. For the horizontally acting elements of Fig. 4, the bracket B supporting the element is rotated through 90° and the friction coupling holding the magnet is appropriately altered.

The accelerometer A of Fig. 5(a) is shown in greater detail in Fig. 5(b). The following qualities are required of the accelerometer:

(a) The lowest mechanical resonance must exceed 10 kHz so that adequate gain may be applied in the feedback loop. To achieve this, the PZT must be used in the compressional mode; bending modes (bimorph devices) are too soft.

(b) The PZT element is a pure capacitance C and requires a resistance R in parallel to define the dc conditions. The lowest frequency, $1/RC$, to which the element will respond must be chosen lower than the lowest frequency component of the vibrations to be compensated. The resistance R causes a mean square noise voltage

$$\overline{\Delta V^2} = 4\ kTr\Delta f, \text{ where } \Delta f \propto 1/RC, \text{ so that } \overline{\Delta V^2} \propto \frac{4kT}{C}.$$

For typical values of $C \sim 1$ nF, the noise voltages are on the order of about 4 μV. The mass m must be chosen large enough so that the smallest accelerations to be measured will give signals larger than this limiting noise value.

(c) PZT material is also pyroelectric, typically producing signals of 10 V per degree of temperature change. A change of 1 μK would produce a signal larger than the thermal noise voltage discussed above; it is therefore necessary to thermally isolate the PZT and to use some thermal compensation.

The detailed accelerometer construction is shown in Fig 5(b). The silver-coated PZT disc is axially polarized and attached on one surface to a glass disc which supports a boss for attaching the mass m. The other surface of the PZT has an annulus of the silver coating removed. A steel thrust piece is attached to the outer ring of the PZT. Electrical contacts are made to the thrust piece and the center of the PZT. The whole construction sits on another glass disc (for thermal isolation), which in turn sits on the accelerometer base.

Notice that a temperature change will produce equal and opposite charges on the two faces of the PZT disc but will produce *no* voltage difference between the outer ring and center of the lower surface of the PZT. On the other hand, an acceleration will cause a change of force across the outer ring of the PZT only and will, therefore, produce a voltage difference.
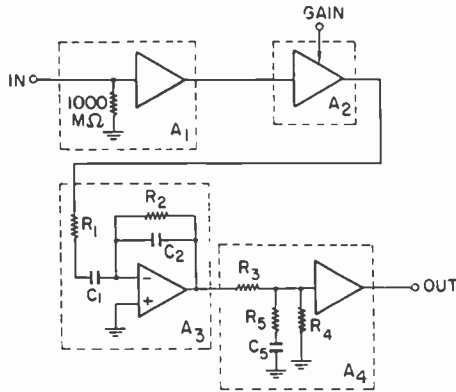
Fig. 6—Block diagram of electronic circuits for dynamic vibration isolation.

The accelerometer signal is processed by the circuit shown in Fig. 6 before being fed back to the electromechanical transducer LS as the correction signal. The basic processing consists of integration, with some low- and high-frequency attenuation. A preamplifier A_1 with 1000 MΩ input impedance is followed by a variable gain stage A_2 employing a transconductance operational amplifier. The signal is then fed to the integrator A_3. DC blocking by the capacitor C_1 passes only signals with frequency higher than a predetermined low-frequency limit (typically 1 Hz) and thus, together with resistor R_2, maintains dc stability. The time constant $C_2 R_2$ should be roughly unity or greater. The output of the integrator is finally amplified by the power stage A_4 before passing to the transducer. The divider chain comprising R_3, R_4, C_5, R_5 gives high-frequency attenuation above a frequency of around 200 Hz and allows higher gain to be used in the feedback loop before the onset of high-frequency oscillation.

The power stage A_4, illustrated in greater detail in Fig. 7, is a class D switch-mode amplifier giving a very high power conversion efficiency. The waveforms V_1, V_T, and V_0 are shown in Fig. 8. The diodes D_1 introduce a nonlinearity at large input voltages, which prevents the stage from being driven into saturation.

The stage can deliver up to 30 W but under normal conditions (in a laboratory with a maximum acceleration of around 10 cm/sec^2 at 20 Hz) the power required is under 1 W. Full power is normally only required for isolating against forces supplied directly to the supported mass M (e.g., hand contact). Because of the large difference between mean power and maximum power it is convenient to use rechargeable batteries as the power source with a trickle charger providing sufficient power to cover the mean consumption.
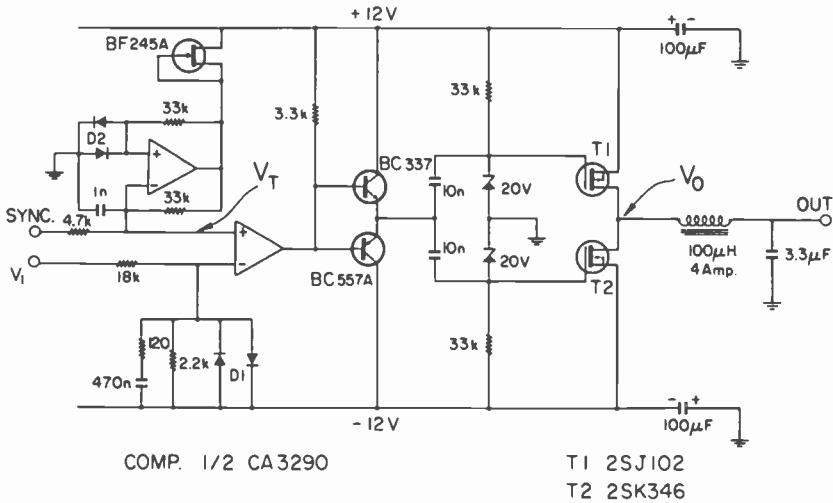
Fig. 7—Class D output stage.

Isolation Properties

The transmissibility of the table defined by the ratio a_1/a_2 of Eq. [4] has a minimum value of about 0.01 at 30-Hz excitation frequency (i.e., a 30-Hz disturbance will be suppressed by a factor of about 100). At lower frequencies, the transmissibility increases roughly as $1/\omega$, being about 0.03 at 10 Hz and 0.1 at 3 Hz. Below 1 Hz, the transmissibility tends rapidly to unity. At higher frequencies, in the range 30 to 200 Hz, the transmissibility stays in the range 0.01 to 0.03, but the dynamic isolation becomes gradually less effective until above about 200 Hz the isolation is purely passive, being supplied by the rubber support blocks.

Applications

The table described here, using dynamic vibration isolation, is essentially rigid at frequencies greater than about 1 Hz. Thus, when
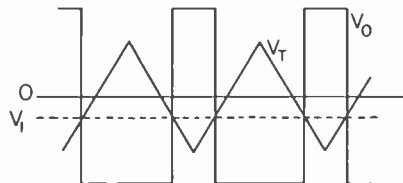
Fig. 8—Waveforms associated with the output stage of Fig. 7.

used as a support for a high-resolution optical or electron micro-scope, forces introduced by the operator's hands or pumping lines are absorbed without producing movement in the table top. Similar arguments apply when it is used as a support for a spectrometer; a Fabry-Perot interferometer has been operated on a predecessor of the present table for several years with quite unprecedented reso-lution. We have high expectations that the table could be effectively used as a support for step-and-repeat cameras, which are presently running into problems as resolution is pushed to the limits. The dynamic rigidity offered by this table should closely approximate the ideal rigid base on which instruments are designed to operate.

Megasonic Particle Removal from Solid-State Wafers

Stanley Shwartzman and Alfred Mayer*
RCA Solid State Technology Center, Aerospace and Defense,
Somerville, NJ 08876

Werner Kern
RCA Laboratories, Princeton, NJ 08540

Abstract—A noncontact electronic cleaning system is described for the
removal of micron-size and smaller particles from silicon
wafers used in the fabrication of solid-state devices. The ap-
paratus consists of a tank with a suitable cleaning liquid and
one or several transducers operating in the high-frequency ul-
trasonic range of 850 to 900 kHz (hence the term "mega-
sonic"). Unlike ultrasonic scrubbing, the cleaning action re-
sults from high-pressure waves set up in the solution, rather
than from the implosion of bubbles that are generated by ul-
trasonic cavitation. For silicon substrate and device wafers,
solutions based on hydrogen peroxide mixtures are used that
effect the simultaneous desorption of organic and inorganic
contaminants from the surfaces, even though the temperature
does not normally exceed 40°C. This low processing temper-
ature greatly reduces the rate of hydrogen peroxide decom-
position, resulting in substantially reduced consumption of
chemicals.

Commercially available megasonic cleaning units are de-
signed for either static or dynamic operation. In the static type,
the wafers remain stationary in the tank solution and the trans-
ducers alternate from on to off. In the dynamic type, which is
especially well-suited for production processing, the wafers
move through the solution while the transducers are continu-
ously powered. The complete system integrates the various
parts, which include the megasonic cleaning tank, the rinse

---

* Now with Gilbert Scientific, 18 Davenport St., Somerville, NJ 08876.

station, the high-velocity forced-hot-air dryer, and the storage enclosure. The megasonic system has been used industry-wide to clean a wide variety of materials besides silicon substrates and device wafers, for which it was originally designed.

1. Introduction

This paper describes the development of a cleaning system designed specifically to remove small particles from silicon wafers to be used in the fabrication of solid-state devices. It is called the "megasonic cleaning system," where the term megasonic is used to differentiate this high-frequency method of cleaning from the more commonly known low-frequency ultrasonic method.

The removal of soluble impurities from the surfaces of a semiconductor wafer is, in general, important in the manufacture of integrated circuits. However, reduction of the number of detectable insoluble particles adherent to a surface nearly to zero is absolutely essential to assure functionality of high-density memories that employ line widths of 1 μm or less. The major fraction of the integrated circuit industry's device yield loss may in fact be traceable to particulate contamination.

The paper describes the principles of operation of the total megasonic cleaning system, whose individual components (cleaning, rinsing, drying, and storage) form a compatible whole. While megasonic energy provides the cleaning force, it is also necessary to relate the solution chemistry, the carrier geometry, and the rinsing, drying and transfer procedures to each other, so that the cleaned surfaces will not be recontaminated after cleaning.

The megasonic cleaning system[1-3] employs a noncontact, brushless electronic scrubbing apparatus that was developed primarily for removing particulate matter (1 μm and smaller) simultaneously from both sides of a silicon wafer. This integrated system allows the wafers to be cleaned, rinsed, dried, and inserted directly into a furnace in the same quartz carrier. Sonic energy from the transducer array panels is directed parallel to the surface of the wafers which are immersed in the media liquid. The scrubbing action is provided by piezoelectric transducers that produce short sonic waves at a frequency of approximately 850 to 900 kHz. The particulates are physically forced from the surface of the wafer by the very high frequency sonic pressure waves generated in the bath liquid. Particles on the order of 0.3 μm in diameter can be effectively removed with input power densities of between 5 and 10 W/cm^2. By compar-

ison, ultrasonic cleaners[4-6] normally operate at 20 to 80 kHz and at power densities up to 50 times higher than those of megasonic systems. Fig. 1 shows a first design of the megasonic cleaning tank, the associated equipment, and the operation of the complete system for factory applications.

Megasonic cleaning has also been applied successfully and industry-wide to the cleansing of photomasks, glass plates, sapphire substrates, metals, ferrite heads, plastic carriers, wafer boats, and storage boxes. However, detailed data are available only for silicon wafer applications.

2. Background

The efficient removal of particles from silicon wafer surfaces is essential to the manufacture of large-scale integrated circuits.[7-9] With thousands of active elements per chip and line-width dimensions under 2 μm, the removal of micron-size and submicrometer particles (less than 0.3 μm) is a necessity, since such particles can cause device defects. A rule of thumb dictates that defects larger than 25% of linewidth should be considered statistically significant.

It should be realized that removal of particles becomes more difficult as the particle size decreases, since adhesion forces increase exponentially with decreasing particle size. Ever finer geometries
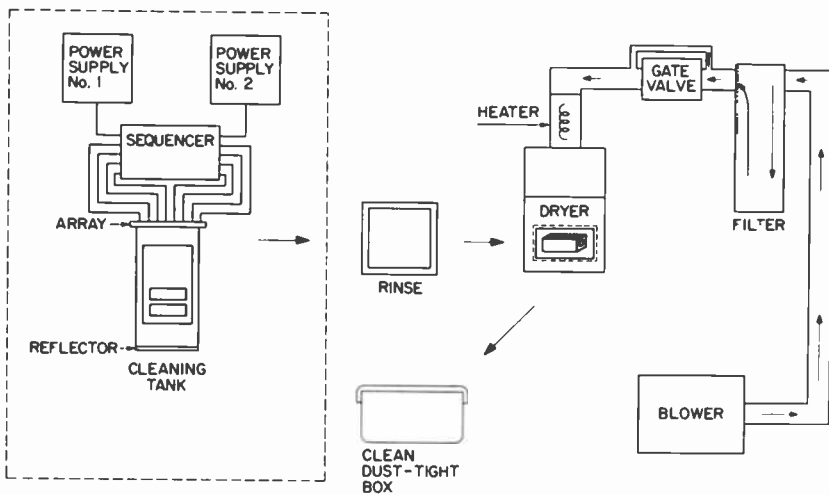
Fig. 1—Schematic diagram of first megasonic factory system and its operation.

of the device features requires removal of smaller and smaller particles, which may demand the application of even higher frequencies than used in the present system.

Starting substrate wafers (that is unpatterned wafers after lapping, polishing, storing, and prior to oxidation or photoresist coating) used in the manufacture of solid-state devices, must also be made chemically clean. Since most dirt particles are typically made up of silicon, minerals, metals, or organic matter and are insoluble in aqueous cleaning agents, they are usually removed by mechanical scrubbing.[10,11] However, these scrubbers are intended to be used with aqueous, neutral detergent solutions. If used with chemically active cleaning solutions, they corrode rapidly. Therefore, mechanical scrubbing must be complemented by chemical cleaning[12,17] in a separate process step. An additional problem of this type of brush-cleaning technique is the maintenance of scrubbers. The brushes load up with dirt particles, and wafers are periodically chipped or broken, showering debris over the brushes. If the brushes are not replaced frequently, they themselves become a source of scratches and particle contamination. Also, scrubbers are sequential in operation, and wafers have to be loaded and unloaded one at a time. Many machines scrub and spin-dry only the front side of the wafer and may leave the back surface wet.

An alternative technique is high-pressure water jet scrubbing.[10,11] This technique allows a jet of fluid to penetrate into the dense device topography, but it too has been found to frequently cause extensive work damage to silicon crystal surfaces.[18]

Finally, conventional chemical cleaning based on the use of hydrogen peroxide solutions is relatively slow and requires a large amount of the chemicals because the peroxide decomposes rapidly in the hot solution. Since the solution can only be used for one wafer batch at a time, the conventional immersion cleaning method is wasteful of energy and chemicals. Obviously, then, a need exists for a highly reliable cleaning system that is compatible with current wafer-handling technology, that can remove particles down to at least 0.3 μm, and that can chemically clean both surfaces of a wafer and leave them dry. These goals have been achieved in the megasonic cleaning system.

3. Discussion of Technique

The success of the megasonic system is probably as much due to the attention paid to the total-system concept, i.e., choice of liquid medium, wafer-holding fixtures, rinsing, drying, storage, and wafer

transferring, as to the high-frequency insonation treatment. Why then, is it not possible to obtain anything like this cleaning action with a 20- to 80-kHz ultrasonic system used in the same way, even at 10 times the power density?

The answer is that the mechanisms of cleaning in the two systems are different. When low-frequency insonation is used, cleaning takes place mainly by cavitation. Cavitation depends on the formation of shock waves and works by the impact of these waves on particles adhering to a surface. Cavitation bubbles are formed by the successive high-pressure and low-pressure components of the acoustic wave. These components cause a hole or cavity to form in the liquid, which implodes when the walls can no longer sustain the tensile forces. Gas bubbles or particles are nucleation centers that cause the cavities to collapse before they can fully develop. That is why it is customary to de-gas solutions in low-frequency ultrasonic cleaning.[4-6]

We believe that the cleaning mechanism for high-frequency insonation is different. Our observations of the effectiveness of megasonic cleaning indicate that gas bubbles are not detrimental. The best cleaning action takes place when the liquid in the megasonic tank can wet the substrate and particle surfaces; therefore, we have used ammoniacal hydrogen peroxide solution as the medium. The hydrogen peroxide evolves oxygen freely, even in the cold solution. The cleaning action is excellent, as measured with silicon substrates deliberately contaminated with 0.3 μm alumina particles or with fingerprints made with a saturated hydrocarbon grease. Calculations based on a transfer of 7.5 W/cm^2 to the wafer surface suggest that the water molecules move only about 0.1 μm in each cycle, but that their acceleration is on the order of 10^5 g. The maximum instantaneous velocity is about 30 cm/s. It appears that the time between pulses, 1.25 μs, is too short for the formation of cavitation bubbles. Rather, we believe, a high-pressure wave pushes and tugs at particles 850,000 to 900,000 times per second. The peak pressure is about nine atmospheres.

These considerations led us to model megasonic cleaning as follows (Fig. 2). Imagine that the particles move sufficiently to permit solvent to diffuse rapidly into the interface between the wetted substrate and the particle. The liquid film acts as a wedge and progressively reduces the contact area until the particle becomes dislodged, is free to move, and becomes suspended in the solution. Its re-adsorption is prevented by the liquid film and by the electrical charges of the particles, which have the same polarity as the sub-
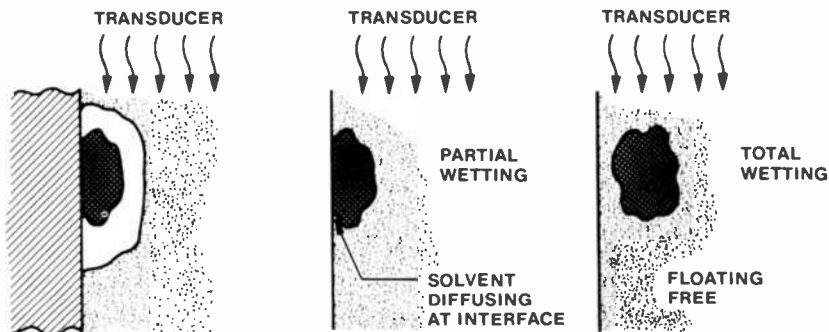
Fig. 2—Model of megasonic action on a particle held on a silicon wafer surface: Frequency 900 kHz; pressure 9.1 × 10⁵ N/m²; maximum instantaneous velocity 30 cm/s; wavelength 1.3 mm; acceleration ~10⁵ g; motion of H_2O molecule ~0.1 μm.

strate. The main features of high-frequency insonation are the local action, the large pressure, the dimensional match between wave and particle, and the wetting action of the liquid medium.

4. Transducer Assembly and Cleaning Tank

The heart of the megasonic system is the piezoelectric ceramic transducer assembly that generates the high-frequency pressure wave in the liquid medium. The best transducer crystals available to us[1] had a maximum diameter of 63 mm and a thickness of 2 mm. The thickness of the oscillating crystal determines the frequency of operation; in this case, approximately 850 to 900 kHz. At the time of system development, transducer manufacturers would not produce crystals thinner than 2 mm at 63-mm diameter. The piezoelectric material chosen for the megasonic cleaning system was lead zirconate titanate. These particular piezoelectric transducers are readily available and have a high Curie temperature, which helps to prevent depolarization and thus extends their operating life.

The divergence of the sonic pressure beam generated by a single 63-mm diameter transducer is very small, so that coverage of wafers larger than 63 mm in diameter required movement of either the wafers or the transducer. We initially chose to forego the problems associated with mechanical motion and decided to clean large areas by electronic switching of an array of several transducers. The 63-mm transducers were cut into hexagons (to increase packing density) and mounted on a common protective foil that also acts as an

electric front-surface contact. The array was then encapsulated for rigidity and used to form one wall of the cleaning tank (Fig. 3).

The cleaning tank material must be compatible with the cleaning solution. Polypropylene is a good choice for the tanks provided a reflecting plate, set at 45°, is placed in the tank opposite the transducers. The reflector is constructed ideally from two plates of fused quartz separated by a layer of air. The reflector serves three purposes: (1) it sends the reflected pressure wave to the liquid surface to prevent interference with the primary wave, (2) it protects the polypropylene from being damaged by the absorbed energy, and (3) it causes small spouts to be generated at the liquid surface as an indication that the system is operating. A detailed schematic of a static megasonic cleaning tank is shown in Fig. 4. Fig. 5 is a photograph of a small commercial static megasonic unit of recent design.

5. Experimental

5.1. Test Vehicles and Conditions

After the preliminary experiments had confirmed the effectiveness of megasonic cleaning, a detailed evaluation of the process parameters was made by measuring the time required to clean wafers that
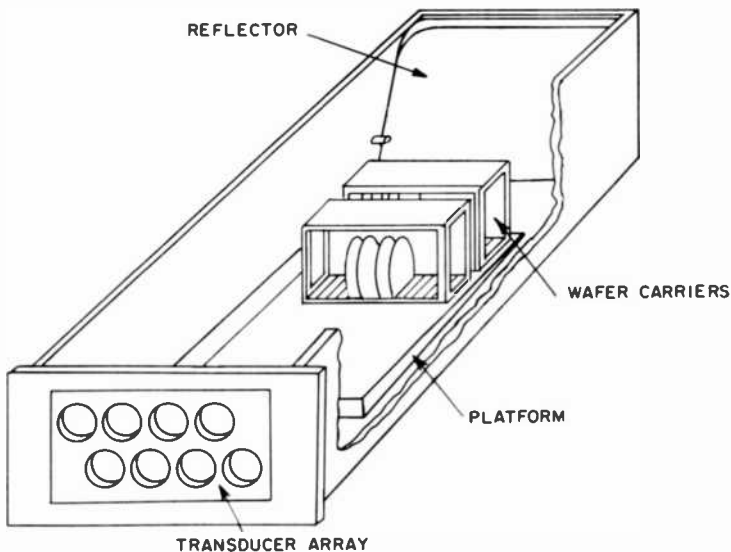
Fig. 3—Megasonic cleaning tank showing array of 8 transducers, reflector, and wafers in stacked carriers for cleaning.

QUARTZ
DEFLECTOR PLATE

VITREOUS CARBON
LIQUID-LEVEL SENSOR

ENERGY-CARRYING
SOLUTION

POLYPROPYLENE
TANK

TANTALUM FACEPLATE

TRANSDUCER PANEL

PRODUCT

PARTICLE   SONIC ENERGY

SUBSTRATE

OUTPUT
POWER: 300 W MAX.
          800 kHz

OPERATING
POWER: 120 V, 60 Hz
          10 A
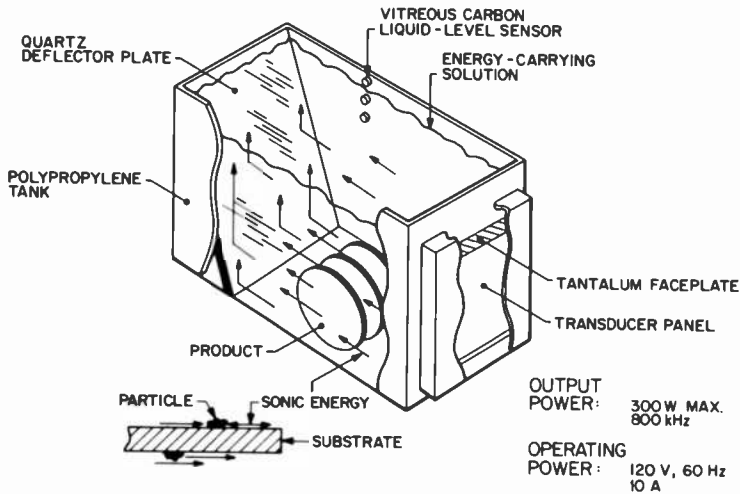
Fig. 4—Detailed schematic of static megasonic cleaning tank. The trans-
ducer plate incorporates a set of 8 transducers. The wafer holder
is not shown for clarity. The megasonic action for particle removal
is indicated schematically. In an alternative system design the
transducers are mounted in the shape of strips on the bottom of
the tank, rather than in the side panels, eliminating the need for
the reflector. A commercial unit of this type is shown in Fig. 5.
There is no difference in the effectiveness of the two designs.

had been contaminated with fingerprints or particles. The particles
were deposited by dipping wafers into a slurry of 2.5 g of 0.3-μm-
diameter aluminum oxide suspended in 1 L of deionized water; the
slurry was stirred constantly to keep the alumina particles from
agglomerating. The wafers were then drained, dipped in clean
water, and spin-dried. The wafers had particle counts in the range
of 5×10^3 per cm^2, as determined by examination under a micro-
scope in dark-field mode at $100\times$ magnification. After cleaning and
drying, the wafers were scanned across the top, middle, and bottom
third, starting and finishing about 4 mm from the edge.

With the megasonic cleaning system described, a natural finger-
print is removed in less than 1 minute. About 4 minutes are re-
quired to remove the particulate contaminants to a level of no more
than 1 cluster (3 or 4 particles) per scan. This performance should
be compared with the usual cleaning method of immersing the
wafers in hot SC-1 (RCA "Standard Clean" consisting of ammonium
hydroxide, hydrogen peroxide, and deionized water[12,16,17]) for 15
minutes, cascade rinsing, and then spin-drying. It takes 3 to 5 min-

Fig. 5—Photograph of a Fluorocarbon Model 2600-3 static megasonic unit with two bottom-mounted strip transducers and electronic computerized programming panel. (Courtesy of Fluorocarbon Company).

utes to remove fingerprints by this method, and particles are not removed to a significant level except by scrubbing prior to the hot SC-1 bath.

All of the experimental work was carried out with silicon wafers that had been polished by conventional mechanical-chemical techniques. Occasionally, experimental wafers that had become contaminated with oil, wax, or other organics were precleaned in 1,1,1-trichloroethane. Artificial fingerprints made with vacuum grease could not be removed unless the surface was first degreased. A "ghost" of the print remained, but disappeared completely after megasonic/SC-1 treatment.

5.2 Basic Considerations

The conventional cleaning approach based on immersion in hot (75–80°C) hydrogen peroxide solutions is intended for and limited to

the removal of soluble organic and inorganic surface contaminants.[12,15-17] Most particles are insoluble under normal conditions. They are held on the surface by electrostatic and Van der Waals forces or chemically by the formation of hydrated interpenetrating oxides. The entire surface is usually covered by a thin organic film that deposits from room air and renders the surface hydrophobic. In addition, organic films may derive from residues of solvents, atmospheric contaminants, and condensed vapors from plastic containers.

To remove a particle, enough energy must be imparted to it so that it moves far enough away from the surface not to be recaptured. The steep pressure gradient of the megasonic energy beam appears to be most effective for this purpose. Disengagement of the particle is facilitated by allowing a liquid of suitable polarity to penetrate into the space between the particle and the surface. However, the liquid penetrates easily only when it wets both surfaces. Previous work[19] had shown that megasonic/SC-1 promotes wetting and readily removes organic contaminant films. With the megasonic system, a fingerprint could be removed in approximately 40 to 80 s in SC-1 at 30°C. Heating the solution to 60 and 80°C shortened that time somewhat, but also increased the solution decomposition rate.

The speed of sound in water changes only about 2.5 m/s per degree Celsius; hence, hot and cold solutions tune at virtually the same frequency. Initially contaminated, hydrophobic wafers cleaned megasonically in SC-1 were found to be hydrophilic after only 1 minute in SC-1 between 20 and 45°C.

Repetition of these tests with water alone did not produce the same cleanliness either in removing fingerprints or particles. Similarly, an aqueous Triton-X* surfactant solution was effective but less so than SC-1 solution. Use of chlorinated solvents and alcohol usually left "ghosts" of fingerprints on the surface. A special problem in evaluating these reagents is that they all contain many particles. RCA "Standard Clean" SC-2 (hydrochloric acid, hydrogen peroxide, and deionized water[12,16,17]) is known to remove ionic and metallic surface impurities effectively, but is less effective than SC-1 solution in particle removal, possibly because its higher zeta potential and its somewhat lower redox potential slow down the oxidative dissolution of surface organic films. Alternative agents used in industry are sulfuric acid–nitric acid mixtures and sulfuric acid–hydrogen peroxide mixtures.[14] Because these agents are highly cor-

* Registered trademark, Rohm & Haas Co.

rosive, their use was not explored in detail. Initial corrosion tests indicated, however, that the megasonic tank parts could be constructed of zirconium, tantalum, and PTFE (polytetrafluoroethylene) and then would probably stand up to these acids and to SC-2 solution.

5.3 SC-1 Solution as Solvent

Subsequent experience has shown that the choice of SC-1 was sound. The usual composition is 5:1:1 by volume of deionized water, ammonium hydroxide (29 w/w% based on NH_3), and hydrogen peroxide (unstabilized, 30 w/w% H_2O_2).[12,16,17] Hydrogen peroxide decomposes slowly at low temperatures. Moreover, the cleaning action is effective even for a hydrogen peroxide concentration as low as 0.1% of the original concentration. Therefore, the main reason for changing the solution is that the particle concentration has become too high. Continuous filtration has proved useful in reducing the rate of particle accumulation. Typically, we measured between 20 and 200 particles of 0.5-μm diameter per liter of solution and between 400 and 2500 particles/L of 0.2-μm diameter in the center work area of the megasonic work station.

Measurements showed that the megasonic SC-1 solution during a 24-hour period of intermittent use and storage decreased in H_2O_2 content by 38% and in NH_3 content by 47%. In immersion treatments at 85°C, this level of decomposition occurs in less than 40 min.[17]

Care must be taken in the cleaning with hot SC-1 in the immersion mode to prevent depletion of the H_2O_2; otherwise silicon wafers may pit due to etching. By contrast, no pitting is observed after a 30-min treatment in the megasonic cleaning system with cold 1:5 ammonia-water solution in the complete absence of peroxide; however, cleaning is much faster and more effective if the hydrogen peroxide is present.

Figures from the production line indicate that the cost of chemicals used for cleaning has actually been reduced by 90%. A hidden benefit is the much-reduced cost of neutralizing the effluent for ecologically acceptable disposal.

Meek et al.[21] showed that SC-1 effectively removed impurities with atomic mass above that of chlorine, and that diodes made in silicon after this type of cleaning showed improved breakdown characteristics. We deliberately contaminated silicon wafers with copper, and then cleaned the surfaces with megasonic/SC-1. The data obtained by solid-state mass spectroscopy (SSMS), by neutron

activation (NA), and by atomic absorption (AA) of extracts of the surface with complexing reagents indicated that the process had removed copper from the silicon surface below the analytical detection limits. The copper detection limits were 1.0 ppma for SSMS and AA, and less than 0.4 ppma for NA.

It is likely that heavy metal ions (many of which tend to form stable amine ions) and the alkali and alkaline-earth metal ions will be removed by megasonic/SC-1 cleaning at 35–40°C to a large extent because they exchange ions readily with ammonia and, therefore, can be rinsed off. The remarkable effectiveness of 75–80°C hot SC-1 and SC-2 immersion treatments for removing both organic and inorganic contaminants from silicon surfaces has been amply demonstrated and published in numerous papers.[12–17, 19–38] In contrast, the effectiveness of these solutions at low temperatures (35–40°C) in combination with megasonic treatments, while apparently effective, has not yet been measured quantitatively.

A freshly prepared SC-1 solution at an initial temperature of 20°C will gradually heat up to about 35 to 40°C during continuous use. Although the rate of gas evolution appears to increase with usage, no decrease in cleaning action was observed, as judged by the removal of particles and fingerprints. Particulates were usually reduced to a low-enough concentration to pass the dark-field microscopic examination, used at that time for inspection, at the end of 6 min. With a 10-min total cleaning time, virtually no rejects were found by routine inspection.

5.4 Rinsing and Water Supply

Rinsing is used to dilute the residual cleaning solution that adheres to the wafer surface, to establish the lowest practical equilibrium between the rinse and the target surface, and at the same time to float off residual particles without re-introducing them or allowing new particles to recontaminate the clean surface.

Our regular supply of deionized water was monitored for one week and found to contain less than the detectable limit of between 2 and 5 ppb of sodium. The water is used regularly in device production and is known to be adequate for ensuring low capacitance-voltage bias-temperature (CVBT) shift in MOS test capacitors. The rinse water from the single-stage overflow tank was checked regularly after the 2-min rinse cycle at 3 to 4 L/min flow and found to yield the same low sodium concentration. Only on one occasion did the concentration rise to 5 ppb. The amount of solution dragged out

from the SC-1 tank averages about 7 mL/load of 100 wafers of 76-mm diameter.

The contribution of the drag-out to the sodium content of the rinse water after 1 min was determined to be less than 1 ppb. It follows also that the resistivity of the rinse water is low because of the ammonia drag-out, rather than being caused by sodium ions.

Good maintenance of the water system is essential to avoid bacterial infestation. Absolute cartridge filters with a pore size of less than 0.25 μm are needed to keep pseudomonas out; these bacteria are larger than 0.3 μm. The most serious problem we encountered was from intrusion of oil particles from the raw water supply. This led to clogging and rapid multiplication of bacteria on filters and ion-exchange resin beds, and caused some final filters to burst. The appearance of streaked air-dried wafers gave immediate warning of this condition.

5.5 Positioning, Geometric Factors, and Surface Damage

The distribution and relative intensity of the megasonic beam was monitored with the aid of a 5 × 10-mm piece of a transducer; the output from this piezoelectric pickup was displayed on an oscilloscope. It was found that the peak intensity was emitted from an area approximately 25 mm in diameter on a 50-mm diameter hexagonal transducer, and that intensity fell to about half peak value at the transducer's edge. The lead zirconate titanate transducers were very similar in active area, output, and frequency distribution from one to another as well as from batch to batch. No marked interference was found from two adjacent transducers. Beam divergence was very small.

Beam attenuation was very small when directed to a boatload of wafers that stood edge-on. Even when the spacing between the wafers was reduced to 1.5 mm or increased to 12 mm, the cleaning action was as effective as when the beam was directed normal to the surface. The cleaning tank evaluated permitted four carriers, each with 25 wafers, to be arranged in series, i.e., one hundred 76-mm diameter wafers at a time. The first carrier was placed between 76 and 100 mm from the transducer array. Care was taken to avoid interposing reflecting surfaces between the array and the wafers, but a 1.5-mm-thick quartz rod did not appear to change the cleaning action, and can be used to help in the fixturing for irregular samples.

As an extreme test of possible damage to silicon crystals, wafers were exposed to the beam head-on as well as edge-on at distances

between 50 and 300 mm from the transducers for up to one hour at peak output with no motion. No damage was visible under high magnification at this stage or after oxidation and differential etching for detecting surface damage, defects, slip, or dislocations.[19,39–42]

5.6 Drying

The most interesting experimental work on drying has been the comparison of hot-air drying with the more customary spin-drying. The work was part of an evaluation involving the comparison of several commercial spin dryers for cleanliness. Wafers were megasonically cleaned, air dried, and scanned for particle size and density. Some were then dipped in filtered rinse water in the same boat that had also been cleaned megasonically. Repeated hot-air drying introduced no further particles. However, when these wafers were spun dry, all showed an increased particle count of between 10 and $10^3/cm^2$. All the spin dryers were located inside laminar-flow stations and supplied with filtered nitrogen during the drying cycle. The absence of rotary parts, the ease of insertion and withdrawal, and the supply of ultrafiltered high-purity rinse water and air are the main factors that make hot-air drying so successful.

To test the performance of the entire process, quantitative measurements were carried out with a Hamamatsu particle counter. Wafer lots were processed on 16 days by megasonic/SC-1 cleaning, rinsing, hot forced-air drying, and transfer to the counter. One blank silicon wafer per daily lot was measured. The density of particles of 0.3-μm size and larger averaged only 9 particles per 7.5-cm-diam wafer, with a range of 4–14 particles. Particles of 0.8 μm and larger averaged 4 per wafer, with a range of 1–7 particles.

Another major advance is the ability to spot water contamination at a very early stage, again, by the appearance of streaks on the wafers during drying. This situation should be compared with the norm in a typical processing plant, where the first indication of water problems comes from failure of devices to pass end-of-line tests with consequent loss of product.

Even though a high-velocity air stream is used, it exerts little pressure on the wafers, and virtually no breakage occurs. Even wafers thinned to 20 μm for use in vidicon targets have been successfully cleaned in the megasonic hot-air drying system. We recommend the installation of ultrahigh-efficiency particulate membrane gas filters[43] as close as possible to the point of use in the high-velocity forced air stream to insure effective removal of particulates.[44]

5.7 Storage of Clean Wafers

In most silicon device processing operations, it is customary to clean wafers immediately before furnace insertion to minimize re-contamination. We found that polypropylene boxes with tightly fitting lids* made extended storage periods possible, provided the boxes were clean and free from particles and did not give off organic vapors, such as from plasticizer. The most extended tests were made over a period of two months with production wafers cleaned before epitaxial deposition. Some of these wafers were processed immediately and others stored for varying periods up to six weeks. Close to 500 wafers were involved in the test and were evaluated by inspection for haze, stacking faults, mounds, and crystal spikes. No statistically significant difference was detectable between the wafers processed immediately and those stored for six weeks.

A similar test was made with 300 wafers prior to the growth of a gate oxide for MOS transistors, except that the maximum storage time was only six hours. That limit was imposed by the experimental arrangements, and can undoubtedly be greatly extended. Again, no significant difference was discernible between stored and immediately processed wafers.

We must emphasize the importance of keeping the box containing the wafers tightly sealed. Opening of the box to remove just one wafer for inspection can lead to particle pickup unless the opening is done in a class-100 laminar-flow hood with all precautions taken to assure that the operator does not add contaminants from clothing, paper, handling tools, etc. It is strongly suggested that all handling in and out of storage boxes be closely monitored by frequent particle counts made while simulating the operation. It should also be noted that high-voltage static charges may be generated when plastic parts are handled. Charge neutralization of the air in the vicinity of such parts should be instituted to avoid transfer of particles to wafer surfaces by static attraction.[45]

5.8 New Developments for Improving the Apparatus

It is likely that the power density can be reduced and that even smaller particles can be removed at frequencies higher than 1 MHz. Some work was done with pulsed operation at 5 MHz. However, the major problem with 5-MHz operation was the fabrication of transducers that could operate at fairly high power densities and have a

---

* Fluoroware Corp., Chaska, Minn.; Type EO-6 or equivalent.

reasonably large area. It seemed feasible at that time to array smaller transducers that could be electronically switched. The project was not pursued further because of lack of availability of high-power supplies in the 5-MHz range.

Another avenue being pursued actively is the use of a larger power supply to drive all transducers in the array simultaneously. Apart from the reliability assessment, it will be necessary to determine whether dead spots in such an array can occur due to interference between adjacent transducers very closely matched in frequency. It may be possible to overcome such an effect by superimposing phase modulation. A stationary beam may contain high-density power spots that could locally melt stationary plastic boats.

Finally, as pointed out in Ref. [1], it is possible to use both sides of the transducer for cleaning. At present, with one side used, the back-side wave is attenuated in air, so that much of the available energy is unused. However, by making the transducer assembly in the form of a dividing wall between two tanks, both sides are free to radiate waves into a liquid. The problems to be solved relate to the need for close spacing of the transducers and a design for seals which must also withstand the rf voltage laterally and between both sides.

5.9 Other Applications of Megasonic Cleaning

Although the megasonic system was developed as an improved cleaning method for silicon wafers, it has been used with success throughout the industry to clean a variety of materials, such as finished metalized devices, sapphire wafers, glass plates, photomasks, metals, device chips mounted and bonded to headers, reticles, plastic parts (carriers, storage boxes), and ferrites. These and other materials may be cleaned wth megasonics, provided the cleaning liquid is compatible with the material to be cleaned.

6. Dynamic Megasonic Systems

An alternative to the static system described so far that uses an electronically switched transducer array to attain on/off wave action, is a dynamic system[3] designed and built by the Fluorocarbon Process Systems Division of the Fluorocarbon Company of Anaheim, California. This system uses a belt drive to carry the wafers past pairs of closely matched and continuously powered transducers. No electronic switching is required, since the wafers are moving across the energy field. As the largest commercially available piezoelectric ceramic transducer capable of being driven at about 1

MHz has only a 63-mm diameter, two such transducers are offset to cover 76-mm diameter or 100-mm diameter wafers. Construction as well as repair is then quite simple if modules of such pairs are fabricated; one can be seen with the cover removed in Fig. 6. When two such pairs are incorporated, they must be staggered (i.e., not opposite each other) to avoid interference of the sonic beam. To achieve this purpose, a quartz reflector is set into the wall opposite each transducer pair.

The equipment shown in Figs. 7 and 8 scales-up, automates, and improves the original megasonic cleaning system to increase its throughput from about 600 wafers per hour to about 2500 wafers per hour in preparation for the large-scale production of flat-plate silicon solar-cell arrays. A schematic of the megasonic cleaning system designed for very-large-scale application is shown in Fig. 9. With such a high wafer throughput, there was some concern for high particulate buildup in the cleaning solution. For this reason, a recirculation system was added (Fig. 10).

The piping chosen was polypropylene, and all valves, pumps (positive displacement), and connectors were so chosen that no stainless-steel parts or metals other than tantalum are exposed to SC-1 solution. This precaution was taken because hydrogen peroxide decomposes catalytically on such metals as nickel, iron, and platinum, and because SC-1 attacks copper and titanium and pits aluminum, whereas tantalum can withstand exposure to even hot solutions of SC-1.
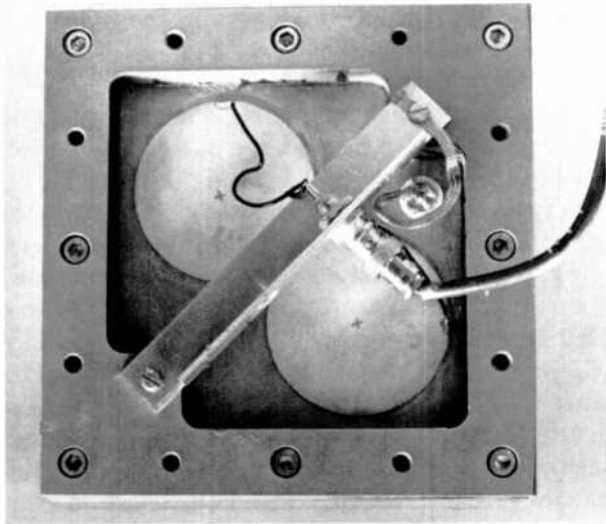

Fig. 6—View of a circular two-transducer module. The transducers are impedance matched and mounted in parallel.
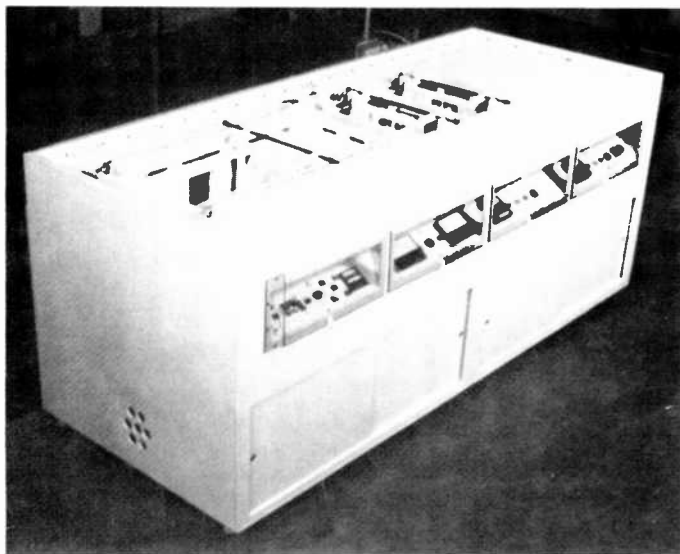
Fig. 7—"Noncontact Electronic Scrubber" cleaning system with side-wall mounted transducers. There are 10 continuously powered transducers in the array. This dynamic system allows continuous and automated flow of wafer lots through the system. (Courtesy of Fluorocarbon Company).

The megasonic units shown in Figs. 7 and 8 have side-wall-mounted transducers. Dynamic systems with bottom-mounted strip transducers are also available (Fig. 11). The effectiveness in cleaning is similar for these two types of systems, but the bottom-mounted version is simpler in construction as it requires no reflector and allows use of multiple frequencies if several transducers are employed.

The wafers to be megasonically cleaned are held in carriers on a platen (Fig. 12). The platen hangs from a rod that engages on and is carried by a continuous polypropylene chain-drive, as shown in the bottom-mounted strip transducer tank, Fig. 11. The speed can be controlled linearly between zero and 65 mm/min. When the platen reaches a magnetic switch, the drive is stopped. The operator manually transfers the three carriers to the overflow rinse tank. A transfer arm, which is standard equipment with chemical processing stations, can be incorporated. The bottom-mounted strip transducers can be powered only when the drive is moving, thus avoiding excessive exposure of a plastic carrier if the drier is stopped
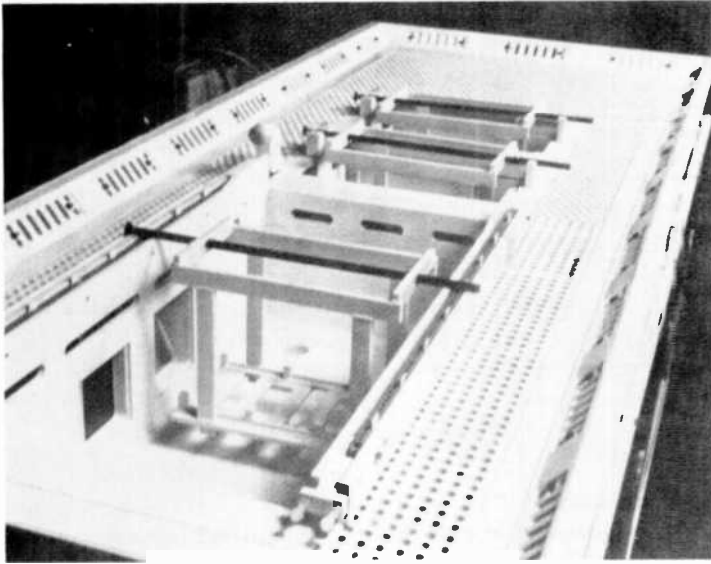
Fig. 8—Detailed view of continuous feed of wafers through the sonic energy field of the system created by the megasonic action. This is a close-up view of the model shown in Fig. 7. (Courtesy of Fluorocarbon Company.)

while a carrier is exposed to the sonic beam. The solid-state power supplies are located underneath the plenum, and each is driven by a signal generator. They are interlocked through a level detector that shuts the power off if the liquid level falls below the level of the detector. If the transducers were exposed to air, i.e., not cooled, they would rapidly overheat and fail.

The Fluorocarbon Company is manufacturing both types of megasonic systems under a nonexclusive license from RCA and offers designs using rectangular strip transducers, some of which are mounted at the bottom of the tank to improve wafer handling (Figs. 5 and 11). Development is in progress to improve the front protective material to make the system compatible with many solvents and strong acids and bases.

7. Summary and Conclusions

The design, construction, operation, and application of a new non-contact, brushless, electronic cleaning system has been described. The apparatus is called a megasonic cleaner because it functions in the high-frequency ultrasonic energy range of 850 to 900 kHz, as

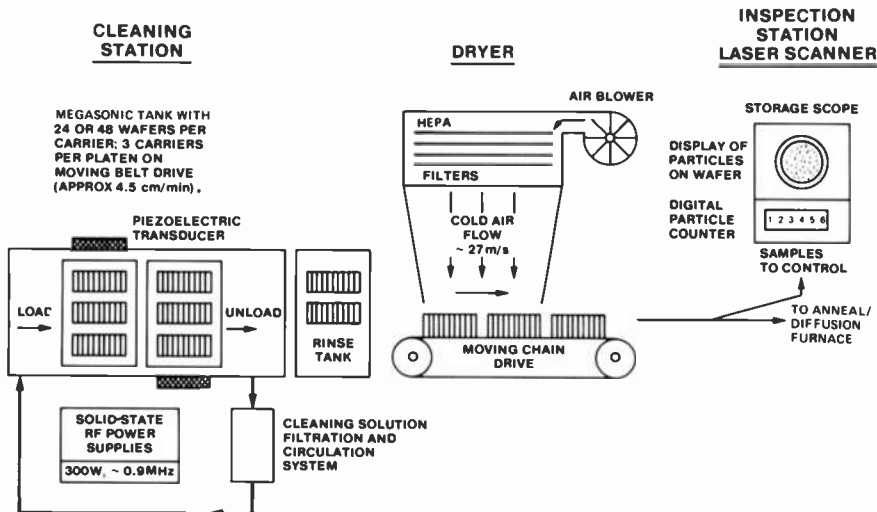Fig. 9—Schematic of integrated megasonic factory system for high-volume processing of silicon wafers for solar cell fabrication. For this application, the high-velocity air in the dryer is not heated to conserve energy. A laser scanner permits nearly continuous monitoring of the cleaning operation.

opposed to conventional ultrasonic cleaners which operate in the 20-80 kHz range. The primary purpose of the system is the removal of particles of about 1 μm and less in size from the surface of silicon substrates and device wafers, including advanced silicon bulk and SOS VLSI circuits and high-density memories. In addition to particulate removal, the megasonic system permits simultaneous desorption of chemical contaminants that are absorbed at the surface of substrates. The utilization of megasonic tank solutions based on hydrogen peroxide-ammonium hydroxide-deionized water (SC-1) and hydrogen peroxide-hydrochloric acid-deionized water (SC-2) as oxidizing, desorbing, and complexing agents appears to be as effective for elimination of organic and inorganic contaminants from silicon and oxide surfaces as the solutions used in the immersion mode at 75–80°C, even though heating of the cleaning solution during the megasonic treatment does not exceed about 40°C by self-heating from the transducers. The considerably lower temperature reduces the decomposition rate of the solutions, rendering the process much more economical than treatments in the immersion mode at 75–80°C.

The megasonic cleaning units are designed for either static or dynamic operation. In the static type, the wafers remain stationary
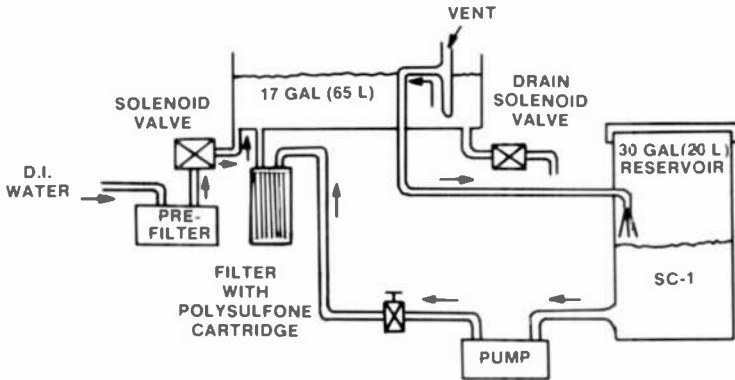
Fig. 10—Schematic diagram of recirculation and filtration system for SC-1 cleaning solution.

in the tank solution, and the transducers in a modular array are electronically switched on/off to achieve maximum efficiency of the megasonic cleaning action. In the dynamic type, the load is mechanically moved through the tank solution, while the transducers
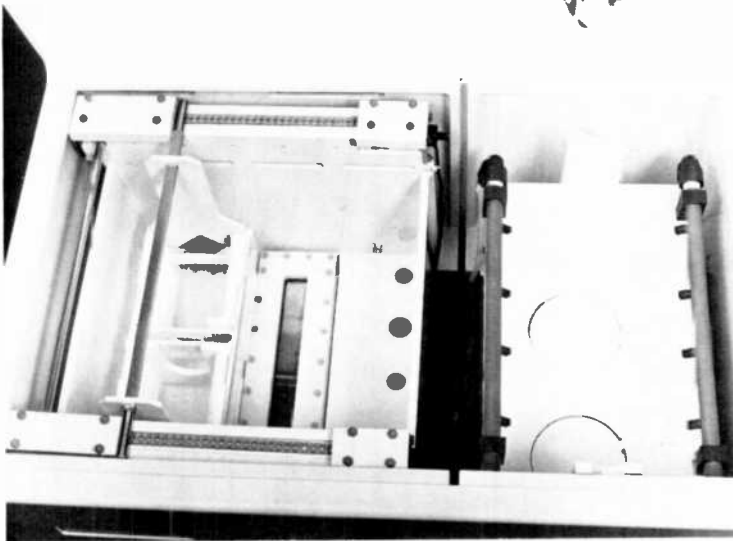
Fig. 11—View into megasonic tank of a dynamic system with single bottom-mounted strip transducer. The right side compartment is a spray-rinse tank with bottom dump exhaust. (Courtesy of Fluorocarbon Company.)
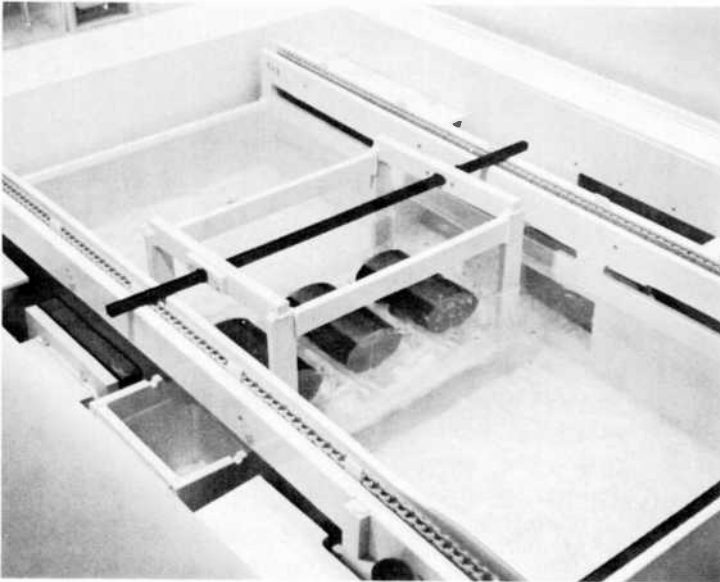
(a)
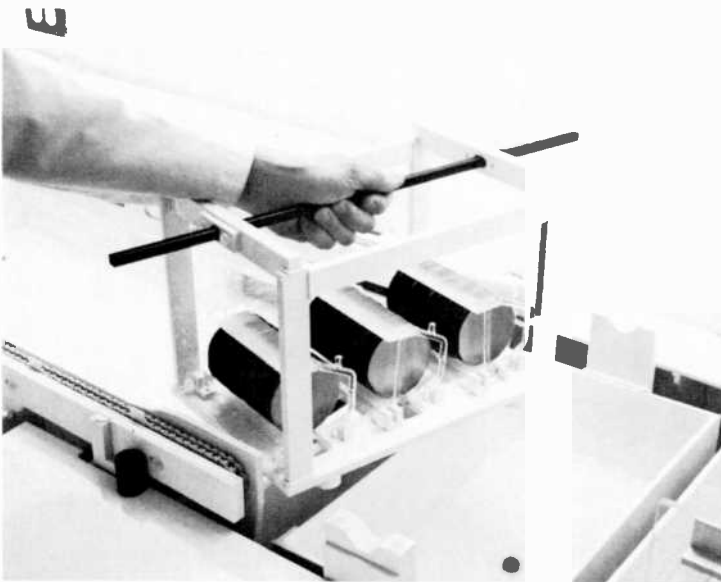
(b)

Fig. 12—Batch of silicon wafers in quartz boats (a) in operating mega-
sonic tank and (b) being transferred in boat carrier from mega-
sonic cleaning tank to overflow rinse tank.

are continuously powered. The dynamic type is ideally suited for automated production applications.

The transducer(s) can be mounted in the side walls of the megasonic tank, in which case a reflector is needed to redirect the path of the pressure wave so as to avoid interference with the primary beam. Alternatively, the transducer(s) can be built into the bottom of the megasonic tank, which eliminates the need for a reflector.

The positioning of the wafer is parallel to the energy beam so as not to obstruct the wave. Wafer holders of fused quartz or Teflon are designed to minimize any shielding or masking effects that would prevent effective cleaning. An explanation has been given on the probable mechanism of particle removal in the megasonic energy field. Unlike ultrasonic scrubbing, the cleaning action results from high-pressure waves set up in the solution, rather than from the implosion of bubbles that are generated by ultrasonic cavitation.

An important aspect of the megasonic cleaning system is the integration of the processing, starting with a batch of wafers in the megasonic cleaning tank for a period of 10 to 15 min, followed by high-efficiency rinsing, drying in filtered, high-velocity hot forced-air, and transfer to the oxidation/diffusion furnace or else storage in closed dust-free containers, all without removing the wafer from the quartz carrier at any time. The entire operation is conducted in a class 100 clean room and handling of the cleaned substrates is minimized, so that recontamination with particles or adsorbates is avoided.

The megasonic system has also been used to clean a wide variety of materials besides silicon wafers. Different solutions have to be used for specific applications, depending on the nature of the substrate and the contaminants. The only precaution that must be observed concerns the exclusion of reagents (e.g., strong hydrofluoric acid solutions) that would attack the metal foil protecting the piezoelectric transducers.

Acknowledgments

Some of the material presented in this paper was prepared and submitted for inclusion in *Treatise on Clean Surface Technology,* Vol. III, K. L. Mittal, Editor; to be published by Plenum Publishing Corp., New York.

References:

[1] A. Mayer and S. Shwartzman, "Megasonic Cleaning System," U.S. Patent No. 3,893,769, July 8, 1975.

[2] A. Mayer and S. Shwartzman, "Megasonic Cleaning: A New Cleaning and Drying System for Use in Semiconductor Processing," *J. Electronic Materials*, **8**, p. 855 (1979).

[3] A. Mayer, "Development of Megasonic Cleaning for Silicon Wafers," Final Report, Sept. 1980; DOE/JPL-955342-79/2, NASA NAS7-100.

[4] P. S. Burggraaf, "Wafer Cleaning: Sonic Scrubbing," *Semiconductor Internatl.* **4,** (7), p. 97 (July 1981).

[5] J. Tuck, "Ultrasonic Cleaning," *Circuits Manufacturing*, **22** (1), p. 56 (Jan. 1982).

[6] M. O'Donaghue, "The Ultrasonic Cleaning Process," *Microcontamination*, **2** (5), p. 63 (Oct./Nov. 1984).

[7] J. M. Duffalo and J. R. Monkowski, "Particulate Contamination and Device Performance," *Solid State Tech.* **27** (3), p. 109, March 1984.

[8] D. L. Tolliver, "Contamination Control: New Dimensions in VLSI Manufacturing," *Solid State Tech.*, **27** (3), p. 129, March 1984.

[9] I. Bansal, "Particle Contamination during Chemical Cleaning and Photoresist Stripping of Silicon Wafers," *Microcontamination*, **2**, p. 35 (Aug./Sept. 1984).

[10] P. S. Burggraaf, "Wafer Cleaning: Brush and High-Pressure Scrubbers," *Semiconductor Internatl.*, **4** (7), p. 71 (July 1981).

[11] A. D. Weiss, "Wafer Cleaning Update," *Semiconductor International*, **7** (4), p. 82–85, April 1984.

[12] W. Kern and D. A. Puotinen, "Cleaning Solutions Based on Hydrogen Peroxide for Use in Silicon Semiconductor Technology," *RCA Rev.*, **31**, p. 187 (1970).

[13] P. S. Burggraaf, "Wafer Cleaning: State-of-the-Art Chemical Technology," *Semiconductor Internatl.*, **4**, (7), p. 91 (July 1981).

[14] D. Burkman, "Optimizing the Cleaning Procedure for Silicon Wafers Prior to High Temperature Operations," *Semiconductor Internatl.*, **4** (7), p. 103 (July 1981).

[15] W. Kern, "Cleaning Solutions Based on Hydrogen Peroxide for Use in Silicon Semiconductor Technology," Citation Classic, *Current Contents*, Engineering, Technology and Applied Sciences, **14**, (11), p. 18.

[16] W. Kern, "Hydrogen Peroxide Solutions for Silicon Wafer Cleaning," *RCA Engineer*, **28**–4, p. 99 (July/August 1983).

[17] W. Kern, "Purifying Si and SiO_2 Surfaces With Hydrogen Peroxide," *Semiconductor Internatl.*, **7** (4), p. 94 (April 1984).

[18] M. Slater, private communication.

[19] A. Mayer, "Detection of Damage on Silicon Surfaces: Origin and Propagation of Defects," *RCA Rev.* **31**, p. 414 (1970).

[20] A. Mayer and D. A. Puotinen, "Silicon Device Processing," in *Silicon Device Processing*, NBS Spec. Public. 337; C. D. Marsden, Ed., U.S. Govt. Printing Office, Wash., D.C., pp. 431–435 (1970).

[21] R. L. Meek, T. M. Buck, and C. F. Gibbon, "Silicon Surface Contamination: Polishing and Cleaning," *J. Electrochem. Soc.*, **120**, p. 1241 (1973).

[22] W. Kern, "Semiconductor Surface Contamination Investigated by Radioactive Tracer Techniques—Part I," *Solid State Tech.*, **15** (1), p. 34 "Part II," **15** (2), p. 39 (Jan. & Feb. 1972).

[23] R. C. Henderson, "Silicon Cleaning With Hydrogen Peroxide Solutions: A High-Energy Electron Diffraction and Auger Electron Spectroscopy Study," *J. Electrochem. Soc.*, **119**, p. 772 (1972).

[24] M. G. Yang, G. M. Koliwad, and G. E. McGuire, "Auger Electron Spectroscopy of Cleanup Related Contamination on Silicon Wafers," *J. Electrochem. Soc.*, **112**, p. 675 (1975).

[25] J. A. Amick, "Cleanliness and the Cleaning of Silicon Wafers," *Solid State Tech.* **47** (11), p. 47 (Nov. 1976).

[26] D. R. Oswald, "Automatic Chemical Processing for Silicon Wafers," *J. Electrochem. Soc.*, **123**, p. 531 (1976); K. D. Beyer, "Silicon Surface Cleaning Process", IBM Techn. Disclosure Bull. **20**, No. 5, p. 1746 (Oct. 1977).

[27] R. M. Gluck, "Novel Gettering of Metallic Impurities on Silicon," *Electrochem. Soc. Ext. Abstr.*, **77**–2, p. 888, Abstract No. 337 (1977).

[28] W. Kern and C. A. Deckert, "Chemical Etching," Part V-1 in *Thin Film Processes*, J. L. Vossen and W. Kern, Editors, Academic Press, New York, pp. 411–413 (1978).

[29] R. M. Gluck, "Gold Removal from Silicon with Dilute Peroxide Mixtures Containing NH_4OH and/or HCl," *Electrochem. Soc. Ext. Abstr.*, **78**–2, p. 640, Abstract No. 238 (1978).

[30] D. A. Peters and C. A. Deckert, "Removal of Photoresist Film Residues From Wafer Surfaces," *J. Electrochem. Soc.*, **126**, p. 883 (1979).

[31] S. P. Murarka, H. J. Levinstein, R. B. Marcus, and R. S. Wagner, "Oxidation of Silicon Without the Formation of Stacking Faults," *J. Appl. Phys.*, **48**, p. 4001 (1979).

[32] A. G. Revesz, "The Defect Structure of Vitreous SiO_2 Films on Silicon. II Channel and Network Defects in Vitreous SiO_2," *Phys. Status Solidi*, **A57**, p. 657 (1980).

[33] L. H. Kaplan, B. K. Bergin, "Residues from Wet Processing of Positive Resists," *J. Electrochem. Soc.*, **127**, p. 386 (1980).

[34] T. M. Hall, Jr., "A Study of the Interface Properties of Deposited Silicon Dioxide on Silicon," Stanford University, Contract No. 19-21-179A (June 1981).

[35] P. F. Schmidt and C. W. Pierce, "A Neutron Activation Analysis Study of the Sources of Transition Group Metal Contamination in the Silicon Device Manufacturing Process," *J. Electrochem. Soc.*, **128**, p. 630 (1981).

[36] S. K. Ghandhi, "Etching and Cleaning," in *VLSI Fabrication Principles*, Wiley & Sons, New York, p. 517–520 (1982).

[37] A. M. Goodman, L. A. Goodman, and H. F. Gossenberger, "Silicon-Wafer-Process Evaluaton Using Minority-Carrier Diffusion-Length Measurements by the SPV Method," *RCA Rev.* **44** (2), p. 326 (June 1983).

[38] B. F. Phillips, D. C. Burkman, W. R. Schmidt, and C. A. Peterson, "The Impact of Surface Analysis Technology on the Development of Semi-conductor Wafer Cleaning Processes," *J. Vac. Sci. Technol.*, **A1** (2), p. 646 (1983).

[39] E. Sirtl and A. Adler, "Chromsäure-Fluss Säure als Spezifisches System zur Ätzgrubenentwicklung auf Silizium," Z. Metallkunde, **52**, p. 529 (1961).

[40] "Standard Test Method for Detection of Swirls and Striations in Chemically Polished Silicon Wafers," ASTM F416-77; *Annual Book of ASTM Standards*, Part 43, Electronics, American Society for Testing and Materials, Phila., PA, p. 840–851 (1981).

[41] F. Secco D'Arragona, "Dislocation Etch for (100) Planes in Silicon," *J. Electrochem. Soc.*, **119**, p. 948 (1972).

[42] G. A. Rozgonyi, "Dislocations, Stacking Faults and "Native" Defect Centers in Silicon Wafers—I. Defect Identification and Mutual Interactions," *Electrochem. Soc. Ext. Abstr.*, **76**–1, p. 167, (1976).

[43] M. A. Accomazzo, K. L. Rubow, and B. Y. H. Lin, "Ultrahigh Efficiency Membrane Filters for Semiconductor Gases," *Solid State Tech.*, **27** (3), p. 141 (1984).

[44] R. L. Duffin, "Process Gas Filtration in Integrated Circuit Production," *Microcontamination*, 1(4), pp. 35–38 (Dec. 1983/Jan. 1984).

[45] G. O. Head, "Air Ionization for Control of Particulates and Electrostatic Discharge," *Microcontamination*, **2** (4), p. 24 (Aug./Sept. 1984).

Patents Issued to RCA Inventors—Fourth Quarter 1984

October

W. G. Anderson Switching Circuit Including PIN Diodes for Impedance Matching (4,477,817)
L. S. Baar Electrical Connector (4,478,472)
D. F. Bowman Three Horn E-Plane Monopulse Feed (4,476,470)
T. Y Chen and W. G. Gibson Video Player with Caption Generator Having Character Background Provisions (4,477,841)
S. P. Clurman Protective Cartridge for Disc Record (4,477,894)
J. W. Daniel, Jr. Phaselock Receiver with Input Signal Measuring Capability (4,479,253)
R. A. Duschl Charge Coupled Device Based System and Method for Measuring Projected Figures (4,480,264)
B W. Faughnan and R. S. Crandall Electrochromic Films Having Improved Etch Resistance and Method for Making Same (4,475,795)
I. Gorog Multi-Bandwidth Optical Playback Apparatus Having Minimum Baseband Distortion (4,477,891)
P. D. Griffis Switching Arrangement for a Stereophonic Sound Synthesizer (4,479,235)
M. D. Hertzler Changeable Liquid Reservoir and Stirrer Apparatus (4,478,172)
G. P. Hope and R. D. Rhodes Lid Latching Apparatus (4,476,994)
W. C. Landis and P. Nyul Light Emitting Assembly and a Method of Making Same (4,479,698)
A. Mattei and W. L. Hahn, Jr. Symbol Synchronizer for MPSK Signals (4,475,220)
M. W. Muterspaugh Electronic Tracking for Tuners (4,476,583)
S. J. Nossen, K. E. McGuire, and S. S. Brokl Multiple Synchronous Counters with Ripple Read (4,477,918)
A. N. Prabhu and S. M. Boardman Thick Film Resistor Inks (4,479,890)
J. J. Prusak and B. P. Patel Apparatus for Injection Molding an Article (4,478,566)
J. J. Prusak Method for the Manufacture of Record Stampers (4,479,853)
D. A. Sheean Deviation Detector for FM Video Recording System (4,476,498)
T. E. Smith and C. C. Wang Purification of VideoDisc Lubricant Additives (4,479,851)
S. Tosima and M. Nishikawa Surface Acoustic Wave Device Having a Pyramid Shaped Tip for Recording Video Information on a Substrate (4,477,892)
R. L. Turner and J. J. Prusak Method and Apparatus for Manufacturing VideoDisc Caddy (4,475,966)
P. G. Welch and E. E. Mitchell Target Support Adjusting Fixture (4,478,701)

November

A. Acampora Automatic Color Control for a Digital Television Receiver (4,482,916)
L. R. Avery Protection Circuit for Integrated Circuit Devices (4,484,244)
D. F. Battson and E. D. Savoye Overcoming Flicker in Field-Interlaced CCD Imagers with Three-Phase Clocking of the Image Resistor (4,481,538)
T. J. Christopher Bias Supply for AC Line Powered Apparatus (4,481,429)
R. M. Colton Core Reset for Single-Ended DC-to-DC Converter (4,481,565)
T. L. Credelle Color Selection Electron Beam Guide Assembly for Flat Panel Display Devices (4,484,103)
T. Fang, E. J. Wittmann, L. A. Harwood, and J. Craft PLL Oscillator Synchronizing System with Matrix for Phase Correction (4,485,353)
P. D. Filliman Level Shifter for an Automatic Kinescope Bias Sampling System (4,482,921)
E. M. Fisher and R. B. Elder Voltage Clamp Circuit Utilizing an Active Device (4,481,433)
P. E. Haferl Regulated Deflection Circuit (4,484,113)
J. R. Hale Strengthening Means for a Deep-Drawn In-Line Electron Gun Electrode (4,484,102)

D. Hampel and J. L. Bradshaw Pattern Recognition System Using Switched Capacitors (4,483,017)

J. J. Hanak Method of Depositing a Semiconductor Layer from a Glow Discharge (4,481,230)

S. A. Harper Method for Preparing a Mosaic Luminescent Screen Using a Mosaic Precoating (4,485,158)

L. L. Jastrzebski and P. A. Levine CCD Imagers with Substrates Having Drift Field (4,481,522)

T. F. Kirschner VideoDisc Player Having Turntable Brake Mechanism (4,485,465)

K. H. Knop and R. H. Morf Diffractive Subtractive Color Filter Responsive to Angle of Incidence of Polychromatic Illuminating Light (4,484,797)

J. R. Matey Scanning Capitance Microscope (4,481,616)

R. B. Maynard, J. J. Moscony, and M. H. Saunders Method for Etching Apertures into a Strip of Nickel-Iron Alloy (4,482,426)

J. T. McGinn, J. F. Corboy, Jr., and L. L. Jastrzebski Method for Growing a Low Defect Monocrystalline Layer on a Mask (4,482,422)

W. H. Meise and R. A. Dischert Error Correction Arrangement for Imagers (4,481,539)

R. D. Miller Regulator for Bias Current of Semiconductor Laser Diode (4,484,331)

M. W. Muterspaugh RF PROM Tracking for Tuners (4,481,673)

E. J. Nossen Fast Frequency/Code Search (4,485,477)

M. Nowogrodzki Channelized Frequency Memory System Employing Feedback (4,484,155)

R. P. Parker Automatic Kinescope Bias Control System Compensated for Kinescope Electron Gun Conduction Dissimilarities (4,484,226)

R. P. Parker Signal Processing Network for an Automatic Kinescope Bias Control System (4,484,228)

R. P. Parker Automatic Kinescope Bias Control System with Selectively Disabled Signal Processor (4,484,229)

M. A. Ralston Broadband Diamond-Shaped Antenna (4,485,385)

A. Sasaki and W. J. Davis Raster-Scanned Display System for Digitally-Encoded Graphics (4,481,509)

R. L. Shanley, 2nd and L. A. Harwood PLL Oscillator Synchronizing System with DC Control of Free-Running Frequency (4,485,354)

J. C. Tallant, 2nd and J. Hettiger Automatic Kinescope Bias Control System Compensated for Sense Point Impedance Variations (4,484,227)

B. K. Taylor and M. C. Stewart Velocity Correction Apparatus for Disc Record Player (4,481,614)

J. Tults Shared Counter Arrangement for a Digital Frequency Locked Loop Tuning System for Selectively Measuring the Frequencies of the LO and IF Signals (4,484,221)

J. Tults Digital AFT System Which Is Activated During Vertical Retrace Intervals (4,485,404)

B. Vanbreeman Rear Projection Television Screen Having a Multi-Surface Fresnel Lens (4,482,206)

H. R. Warren Misregistration Prevention in Two Channel VTRS (4,485,395)

J. A. Wilbur and C. M. Wine VideoDisc Player Having Improved Squelch System (4,484,174)

December

A. Abramovich Fail-Safe Circuit for a Microcomputer Based System (4,488,303)

A. J. Barresi, L. Nelson and J. Pogson Fixture for Solder Thinning Chip Carriers (4,489,923)

W. L. Behrend I.F. Delay Equalizer for a UHF TV Transmitter (4,490,693)

E. A. Brauer Stylus Lifter Locking Mechanism for VideoDisc Player (4,488,285)

L. A. Christopher and D. L. Sprague Incrementing/Decrementing Circuit as for a FIR Filter (4,486,851)

K. T. Chung Damping Material (4,488,282)

K. T. Chung Epoxy Resin (4,488,283)

C. F. Coleman Carriage-Actuated Disc Handling Apparatus for VideoDisc Player (4,486,874)

C. B. Dieterich Coding System for Digital Audio Disc Record (4,488,278)

G. M. Ehemann, Jr. Photodepositing a CRT Screen Structure Using Discrete-Element Optical Filter (4,488,793)

A. M. Goodman and H. F. Goosenberger SIPOS Deposition Method (4,489,103)

C. F. Hackett, E. A. Brauer, K. C. Kelleher, and R. R. Wright In-Arms Stylus Cleaner for Disc Record Player (4,486,872)

P. E. Haferl Electron Beam Suppression Circuit for a Television Receiver (4,488,181)

J. R. Hale and R. J. Alexander Electron Gun Assembly with Bead Strap Having an Angulated Grasping Member (4,486,685)

G. P. Hope Housing for Receiving and Storing Printed Circuit Boards (4,486,816)

R. W. Jebens VideoDisc Player Having Improved Caddy Extraction Mechanism (4,488,280)

K. C. Kelleher VideoDisc Player Having Lifter Driving Circuit (4,486,875)

J. L. Koslov and T. M Wagner CCD Defect Correction without Defect Location Memory (4,488,178)

P. A. Levine Smear Reduction Technique for CCD Field-Transfer Imager System (4,490,744)

M. Lysobey Diode Switching System for a Selectable Impedance Matching Network (4,486,723)

S. V. Naimpally Inductive Electrical Signal Filter with Reduced Impedance (4,489,286)

J. P. Paradise and D. J. Derkach Freeze Clock Circuit (4,489,422)

E. S. Poliniak High-Density Information Disc Lubricants (4,486,325)

G. E. Schmidt, Jr. Closed-Loop Magnetic ROLL/YAW Control System for High Inclination Orbit Satellites (4,489,383)

R. S. Silver Storage Device Having a Semiconductor Target (4,490,643)

C.C. Steinmetz Method of Making a Line Cathode Having Localized Emissive Coating (4,487,673)

F. Sterzer Microwave Radiator Utilizing Solar Energy (4,490,668)

H. J. Wolkstein Method and Apparatus for Compensating Non-Linear Phase Shift Through an RF Power Amplifier (4,488,122)

B. Zuk Timing Circuit (4,487,125)

AUTHORS

Heinrich Auderset graduated in mechanics in 1964. From 1964 to 1967 he worked at the Physical Meteorological Observatory in Davos, Switzerland on problems of global solar radiation standards. In 1967 he joined Laboratories RCA Ltd., Zurich. He was involved in work on Raman scattering of magnetic semiconductors, ferroelectrics and low dimensional materials like inorganic and organic conductors, and in the development of an optical scanner for dust and defect detection on semiconductor materials. At present he works on materials characterization of Polysilicon and Silicon Oxide and of bulk Silicon masking wafers by means of elastic, Raman scattering and the optical scanner. In 1979 Mr. Auderset received an RCA Outstanding Achievement Award for his contribution to the development of the laser scanner.

Glenn W. Cullen received the BS degree in Chemistry from the University of Cincinnati in 1953 and the PhD degree in Inorganic Chemistry from the University of Illinois in 1956. During the following two years he served on the teaching staff and as a Group Supervisor in the Electronics Department of the U.S. Army Air Defense School (Surface to Air Missiles) at Ft. Bliss, TX. In 1958, Dr. Cullen joined RCA Laboratories, Princeton, NJ, as a Member, Technical Staff. Initially, he worked on the chemical stabilization of semiconductor surfaces. Later he was involved in the chemical-vapor deposition of Nb_3Sn, Nb, Ta, and Nb-Ta superconducting thin films. This included the characterization of the electrical properties of the deposits at low temperatures in high magnetic fields. Dr. Cullen has been involved in the preparation and characterization of silicon thin films epitaxially deposited on insulating substrate materials, and in the growth and fabrication of the bulk single-crystal substrate materials. He has coauthored or authored a number of publications and several review articles in this field. Dr. Cullen is Head of the Materials Synthesis Research Group in the Materials and Processing Research Laboratory.
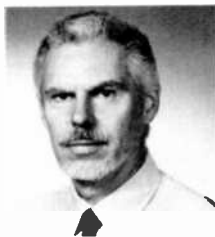
Dr. Cullen received an RCA Laboratories Outstanding Achievement Award in 1963 and 1969. He was also a member of research teams that received David Sarnoff Corporate Research Team Awards, RCA's highest technical honor, in 1965 and 1973. He is a member of the American Chemical Society, the Electrochemical Society, and Society of Sigma Xi, and Alpha Chi Sigma. He has served as the Chairman of the Electronics Division of the Electrochemical Society, and as Chariman of a Gordon Research Conference on Crystal Growth. He has also served as a Trustee of the Federation of Materials Societies, as a member of a National Material Advisory Board Committee on high-purity silicon, and as a member of an Air Force Science and Technology Advisory group. He is a member of the Executive Committee of the American Association for Crystal Growth, and an Associate Editor of the *Journal of Crystal Growth*.

Michael T. Duffy received the BSc degree in Chemistry from University College, Dublin, in 1958 and completed his PhD studies in Solid State Chemistry in 1963. He was a teaching assistant at this University from 1961 to 1963. In 1964 he joined the University of Toronto as a Research Associate and worked in molecular-beam research until 1966, when he joined the staff of RCA Laboratories, Princeton, NJ. Since then he has been engaged in materials research in the field of integrated electronics. Dr. Duffy has worked on the synthesis and characterization of various dielectrics in MIS structures and on the vapor-phase growth of heteroepitaxial materials on insulating substrates, particularly sapphire. His work also included an evaluation of CVD materials for contact with molten silicon. More recent work involved analysis of the surface perfection of polished sapphire substrates and heteroepitaxial silicon films by IR and UV reflectance methods. Since then he has been involved in developing processes for the reactive-ion etching of dielectric films for VLSI processing, and the characterization of amorphous and polycrystalline silicon films for VLSI application.

A Senior Member of the Technical Staff, Dr. Duffy has authored several papers in his field and holds eight U.S. patents. He has shared three RCA Laboratories Outstanding Achievement Awards: in 1969, for work on the MNOS memory transistor; in 1973, for work on a high-speed ZnO/sapphire electro-optic modulator; and in 1980, for the development and application of an innovative technique for optically characterizing the near-surface crystal structure of silicon. He is a member of the Electrochemical Society.

Michael T. Gale received the BA in Physics from Cambridge University, England in 1968 and the MSc. in Optoelectronics from Essex University, England in 1969. He subsequently joined the optics research and development group at Laboratories RCA Ltd. in Zurich, Switzerland, where he has worked on a number of holographic and applied optics projects, with particular emphasis on surface-relief microimages, high-resolution image sampling and analysis techniques, focused laser spot evaluation, and the development of a single-chip CCD color camera. A number of technical publications, 12 issued patents, and an RCA Laboratories Outstanding Achievement Award have accompanied this work.

Günther Harbeke received the Physics Diploma in 1955 and the PhD in Physics in 1958 from the Technical University in Brunswick, Germany. In 1961 he joined the staff of Laboratories RCA Ltd., Zurich. Prior to that he was with the Physikalisch-Technische Bundesanstalt in Brunswick. In 1963, he worked 9 months at the RCA Laboratories in Princeton. Dr. Harbeke has been working in research on the basic optical properties of semiconducting and insulating materials and on light scattering and phase transitions in solids. He has received three RCA Laboratories Outstanding Achievement Awards for team performance in 1962, 1969, and 1984. Dr. Harbeke has a lecturing assignment at the University of Cologne and is a member of the Zurich, Swiss, German, and European Physical Societies.

Werner Kern received his education in chemistry in Switzerland and the United States. His 1947 research thesis on the discovery of fluorescing carcinogenic hydrocarbons in soil established an important new branch of environmental science. He was a research chemist with Hoffmann-La Roche in Switzerland and New Jersey. Later he joined the Nuclear Corporation of America and became Chief Chemist directing research in radiation chemistry. In 1959 Mr. Kern joined RCA Electronic Components and Devices to investigate semiconductor processes by radiochemical methods, was head scientist on several research projects, and was put in charge of radiological safety. In 1964 he transferred to RCA Laboratories, Princeton, NJ, as a Member, Technical Staff; he was promoted to Senior Member in 1983 and Fellow of the Technical Staff in 1985. Mr. Kern has been working in semiconductor process research, specializing in the characterization and device applications of dielectric films, chemical vapor deposition, and etching processes. From 1974 to 1979 he was project scientist for government-sponsored research contracts on glass passivation, dielectric defects, and silicon solar cells. He has been a technical consultant on silicon device processing and chemical safety to RCA Laboratories and the RCA product divisions for the past 20 years.

In 1983 and 1984 Mr. Kern was Chairman of the Electrochemical Society's Dielectrics and Insulation Division and a member of the Board of Directors of this Society. He is a member of the American Chemical Society, the American Vacuum Society, and the Research Honorary Society of Sigma Xi. He is listed in *American Men and Women of Science, Who's Who in Technology Today,* and *Who's Who in the East,* is the author or coauthor of over 80 scientific publications, holds 10 U.S. patents plus several pending, has presented numerous technical lectures and seminars, and has organized and chaired scientific symposia.

He received the Callinan Award of the Electrochemical Society in 1971 for his pioneering research in chemical vapor deposition. Mr. Kern received three RCA Laboratories Outstanding Achievement Awards: in 1966, for his work in integrated-circuit process research; in 1973, for his contributions to the glass passivation of silicon device structures; and in 1983, for developing a ternary glass (CVD BPSG) for low-temperature fusion. He was also awarded a 1981 NASA certificate of recognition. He coedited and coauthored *Thin Film Processes,* published by Academic Press in 1978, and has been Course Lecturer on Chemical Vapor Deposition for the American Vacuum Society since 1981.

Hans P. Kleinknecht received his PhD degree in Physics in 1953 from the Stuttgart Technical University in Germany. He was with ITT in Nürnberg, Germany, and in Clifton, N.J., for five years; with RCA in Somerville and Princeton, N.J., for five years; and with Intermetall in Freiburg, Germany for two years. Since 1963, he has been working for RCA in Zurich, Switzerland. His experience, publications, and patents concern Si crystal growth, characterization of Si material and p-n junctions, rectifiers and transistors, InAs tunnel diodes, electroluminescence in ZnTe and GaP and optical waveguide modulators of GaAlP. Since 1975, Dr. Kleinknecht has been doing applied research on optical techniques in semiconductor manufacturing,

such as in-process etch control, linewidth measurement, and automatic alignment.

Dr. Kleinknecht is a Fellow of Laboratories RCA Ltd., Zurich, Switzerland.

Alfred Mayer was educated in England and joined RCA Somerville's Advanced Materials Group in 1959 where he worked on their gallium arsenide program. By 1961 he headed the surface chemistry group and was involved in most aspects of silicon materials technology: epitaxy, chemical vapor deposition, surface measurements, defect detection and characterization, and especially clean handling techniques. In much of this work, which resulted in numerous publications and patents, he collaborated with S. Shwartzman. Together, they developed the megasonic cleaning concept and helped in the commercialization of units employing this concept. In 1980, Mr. Mayer became vice president of Gilbert Scientific Inc., Somerville, NJ, where he represents several well-known manufacturers of front-end semiconductor production and measurement equipment. He is a member of the Electrochemical Society and the American Society for Testing Materials.

Ernst Meier graduated in 1964 in precision mechanics after a four year apprenticeship with Macafil, Zurich. Following four years in the research workshop of the same company, he joined Laboratories RCA Ltd., Zurich, as a technician. He worked briefly in the chemistry department, and then transferred to the research workshop. He has made significant contributions to the development of the tandem interferometer and many other sensitive instruments.

Heinrich Meier started his professional education and work as a mechanic at Brown-Boveri in Baden, Switzerland, in 1953. From 1959 to 1962 he was a laboratory technician at Laboratories RCA Ltd., Zurich. In 1962 he joined the Imperial College, London, as a research assistant and in 1963 went to Canada to work for Westinghouse at Hamilton, Ontario. In 1968 he rejoined RCA in Zurich, where he was promoted to Technical Staff Associate in 1970. His experience ranges from semiconductor devices, photoconductors, and electroluminescent devices to optical measurement of semiconductor material and design of optical test equipment for semiconductor manufacturing.

John R. Sandercock graduated in physics from Oxford University with a B.A. in 1964 and D.Phil. in 1968 on hot electron effects in semiconductors. Since then he has been working at Laboratories RCA Ltd., Zurich, in the field of light scattering in solids and has brought about significant improvements in the instrumentation for high resolution interference spectroscopy. For this work he received the Duddell medal of the British Physical Society in 1979. Since then his work has been mainly in the field of optical instrumentation for semiconductor technology and high resolution capacitative spectroscopy.

Stanley Shwartzman graduated from the Philadelphia Wireless Technical Institute and attended Temple University. He joined RCA in 1960 and worked extensively on failure analysis of micromodules. In 1964, he joined the Material and Process Department where he worked on designing and developing equipment and instrumentation for use in the study of surface-related phenomena, silicon materials characterization, glass passivation, cleaning, and capacitance-voltage and resistivity measurements. He contributed to the development of the megasonic cleaning system, which RCA now licenses for commercial manufacturing. Mr. Shwartzman joined the Solid State Technology Center in Somerville, N.J., in 1980 where he set up the automatic wafer cleaning systems and worked in improving the while room water supply. He has also worked on low-pressure chemical vapor deposition of SiO_2 and PSG. He is presently a Senior Technical Specialist in the Plasma Etching group.

Mr. Shwartzman holds 7 patents and has coauthored 3 papers.

Richard A. Soltis is a Technical Associate at RCA's David Sarnoff Research Center, Princeton, NJ, and is a member of the Materials Synthesis Research Group within the Materials and Processing Research Laboratory. He joined RCA in 1960 working on the electrical characterization of III-V compounds, the characterization of photochromics, the chemical vapor deposition of thin film dielectrics, and the hetero-epitaxial growth of III-V and II-VI compounds. He is presently involved in the characterization of polysilicon films and the plasma etching of dielectrics.

Edgar F. Steigmeier received the Physics Diploma in 1955 and the PhD in Physics in 1960 from the Swiss Federal Institute of Technology (ETH) in Zurich. From 1960 to 1962, he worked for Brown-Boveri Corporation, Baden, Switzerland, on heat conductivity and thermoelectricity. In 1962 he joined the Materials Research Laboratory of RCA Laboratories, Princeton, where he worked on basic properties and applications of thermoelectric materials such as Ge-Si alloys and III-V alloys; this work has led to high efficiency materials for power generation. In 1964 he transferred to Laboratories RCA Ltd., Zurich. There he worked on problems of heat transport, on optical properties of magnetic semiconductors, and materials involving soft lattice vibrations and phase transitions. Later work was concerned with light scattering of layer structures and of inorganic and organic conductors. At present he is involved in materials characterization (by means of elastic, Raman scattering and optical scanner) of Polysilicon and Silicon Oxide materials, and with Epitaxial and bulk Silicon masking wafers.

In 1969 Dr. Steigmeier received an RCA Laboratories Outstanding Achievement Award for his contributions to the study of materials by means of Raman effect, and in 1979 a second one for the invention of a laser scanner for dust and defect detection. During the Academic year 1973/74, Dr. Steigmeier was a guest lecturer on Solid State Physics at the University of Fribourg, Switzerland. He holds two U.S. patents and is a member of the Zurich, Swiss, and American Physical Societies.

Martin Tgetgel graduated in precision mechanics in 1970. From 1970 to 1971 he attended the Swissair aircraft mechanics school. For the following two years he was employed with Standard ITT, Zurich. In 1973 he joined Laboratories RCA Ltd., Zurich. He was involved in investigations of charge storage on insulating materials and the development of electronic circuits for an optical scanner for dust and defect detection on semiconducting materials. From 1972 to 1976 he attended the Zurich City Evening College in Electronics and in 1978 was promoted to TSA. At present he is working on circuit aspects of optical instrumentation for IC technology and of a capacitative spectrometer.